RESEARCH AND MODELLING IN CIVIL ENGINEERING 2017

EDITED BY JACEK KATZER
AND KRZYSZTOF CICHOCKI

POLITECHNIKA KOSZALIŃSKA

KOSZALIN UNIVERSITY OF TECHNOLOGY
POLITECHNIKA KOSZALIŃSKA

Monograph

RESEARCH AND MODELLING IN CIVIL ENGINEERING 2017

Edited by
Jacek Katzer and Krzysztof Cichocki

KOSZALIN 2017

MONOGRAPH NO 338
FACULTY OF CIVIL ENGINEERING,
ENVIRONMENTAL AND GEODETIC SCIENCES

ISSN 0239-7129
ISBN 978-83-7365-474-7

Chairman of the University Editorial Board
Zbigniew Danielewicz

Editors
Jacek Katzer, Krzysztof Cichocki
Koszalin University of Technology, Poland

Reviewers
Jacek Gołaszewski – Silesian University of Technology, Poland
Izabela Major – Częstochowa University of Technology, Poland

Technical editor
Czesław Suchocki

Website editor
Mariusz Ruchwa

Linguistic consultations
Ewa Sokołowska-Katzer

Typesetting
Czesław Suchocki

Cover design
Tadeusz Walczak
(Photo by *Jacek Katzer*)

KOSZALIN UNIVERSITY OF TECHNOLOGY PUBLISHING HOUSE
75-620 Koszalin, Racławicka 15-17, Poland

Koszalin 2017, 1st edition, publisher's sheet 7,8, circulation 100 copies
Printing: INTRO-DRUK, Koszalin, Poland

Table of contents

Preface

This monograph was created as the scientific outcome of the 2nd Central European Civil Engineering Meeting 2017 (CECEM 2017) which took place at Koszalin University of Technology (Faculty of Civil Engineering, Environmental and Geodetic Sciences) in Poland, 5 - 9 June 2017. Researchers representing four countries (Czech Republic, Slovakia, Romania and Poland) were attending the meeting. The meeting was organized as an ERASMUS+ event. CECEM 2017 had both staff training (STT) and teaching (STA) character and was a great opportunity to share knowledge and experience in the field of civil and structural engineering. The week-long programme included round table discussions, presentations, problem solving cases, lab visits, workshops and social events. The main objectives of CECEM 2017 included peer-learning, networking, transfer of knowledge and sharing research experiences and best practices. Participants brought into the discussion examples from their own institutions and present best practices and innovative approaches to the issues addressed.

The meeting was following the 1st Central European Civil Engineering Meeting 2017 (CECEM 2016) which took place at Koszalin University of Technology (Faculty of Civil Engineering, Environmental and Geodetic Sciences) in Poland, 21 - 23 June 2016. CECEM 2016 attracted researchers from Czech Republic and Ukraine. The success of CECEM 2016 encouraged organizers to transform this event into an annual meeting.

During CECEM 2017 multiple scientific presentations were delivered and discussed. Organizers decided to prepare the monograph as the outcome of the meeting to prevent these high quality presentations from perishing. Willing authors prepared extended versions of their papers for publication. After very careful analyses and peer-review process 10 chapters were accepted for the final version of the monograph. The inclusion of a chapter in the monograph was free of charge for the authors. The peer-reviewing, editing and printing costs were covered by Faculty of Civil Engineering, Environmental and Geodetic Sciences at Koszalin University of Technology.

The 3rd CECEM will take place in Koszalin (Poland), 4 - 8 June 2018. Colleagues from partner and non-partner institutions are encouraged to take part in the event (contact person: prof. Jacek Katzer, cecem@tu.koszalin.pl).

Editors
Krzysztof Cichocki & Jacek Katzer

1. Energy transfer improvement in a water pumping installation

Anca Constantin
Ovidius University from Constanta, Faculty of Civil Engineering, Constanta, Romania

1.1. Introduction

Water and energy are two main topics among the nowadays challenges for engineers and scientists, in the context of the increasing population, growing wealth and consumption, and intensive climate change all over the world. The 2016 International Water Association Forum organized in Brisbane identified six focus areas, stating that ”rebuilding all existing infrastructures is unrealistic, we must focus on optimization and efficiency gains in current practices” (Brisbane Report, 2016).

Pumping installations, providing drinking or irrigation water are among the most important energy consumers, therefore it is determinative for the hydraulic system not only to meet the required technical parameters but also to provide a high level of energy efficiency.

Engineers focus on both the reduction of energy consumption and the efficiency improvement of the end consumers, such as electrically driven hydraulic pumps. An energetic perspective on the pumping stations has to take into consideration the pumps and the pipelines as well (Constantin et al. 2012).

The study is oriented on both branched and looped water supply systems in rural area, aiming to assess the hydraulic parameters in different operation alternatives and to determine by numerical simulation the most appropriate and energy efficient operation method of the pumping installation.

1.2. Theoretical considerations on hydraulic energy

Hydraulic energy is defined as the capacity of a liquid to do work as it flows from one state to another. Usually, in technique, energy is not available in the needed form, therefore it must be transformed by the use of specific machinery. Hydraulic pumps are designed to convert mechanical energy into hydraulic one. The electrically driven dynamic pumps, which are mostly used in water supply, cause a continuous fluid movement due to a rotating part: an impeller or a propeller. In a pumping unit, meaning the pump and its electrical motor, energy conversion takes place in two steps: firstly the electric energy is transformed by the electric motor into mechanical one, and secondly the mechanical energy is transformed by the impeller into hydraulic energy given to the fluid. As the fluid passes through the impeller, its velocity increases. The flow continues through the pump's casing, and the velocity is reduced, because part of the kinetic energy is converted to potential energy. For both motor and pump, energy conversion has a certain efficiency, thus an overall efficiency may be defined:

$$\eta = \eta_e \cdot \eta_p \tag{1.1}$$

Where:

η_e – efficiency of the electric motor, [-];
η_p – pump's efficiency, [-].

The pumping head, the difference between the specific energy in and out the pump, is the most important technical parameter and corresponds to a given discharge. Subtracting the pump's internal losses from the total theoretical head stated by Euler, at different flowrates, will yield the pump's curve, which for the centrifugal type is a parabola. Furthermore, this parabola can be expressed as a function of discharge and rotation speed (Constantin et al., 2011):

$$H_{(Q,n)} = aQ^2 + bnQ + cn^2 \tag{1.2}$$

Where:

H – total head, [m];
Q – discharge, [m³⁄s];
n – rotation speed, [rot⁄min];
a,b,c – constant coefficients.

Pumps and pipelines should operate together in a hydraulic system such a way that the energy given by the pumps to the fluid to be enough for it to overcome the static head and the resistance to movement opposed by the pipelines.

The system curve represents the energy requested by the pipelines and their equipment (valves, elbows etc.) in order to transport different values of flowrate.

$$H_c = H_g + h_r \tag{1.3}$$

Where:

H_g – geodetic head, [m];
h_r – head loss over the pipelines, [m].

In a pumping installation, water flow is turbulent, therefore the head loss is proportional to the squared flowrate:

$$h_r = MQ^2 \tag{1.4}$$

Where:

M – hydraulic resistance modulus for all the pipelines in the pumping installation, $[m^{-5}s^{2}]$.

The equivalent hydraulic resistance modulus for the entire pumping installation, can be calculated according to the way the pipes are connected: series or parallel. A given pump operates on a specific system of pipes at the flowrate for which the energy generated by the pump equals the energy requested by the system.

Thus, for each discharge value given by a pump, we have the relationship (Constantin 2016):

$$H_g + MQ^2 = aQ^2 + bnQ + cn^2 \tag{1.5}$$

Or, stated differently, the duty point, ***F***, is the intersection between the curves (1.2) and (1.3)., as it is shown in Fig.1.1.

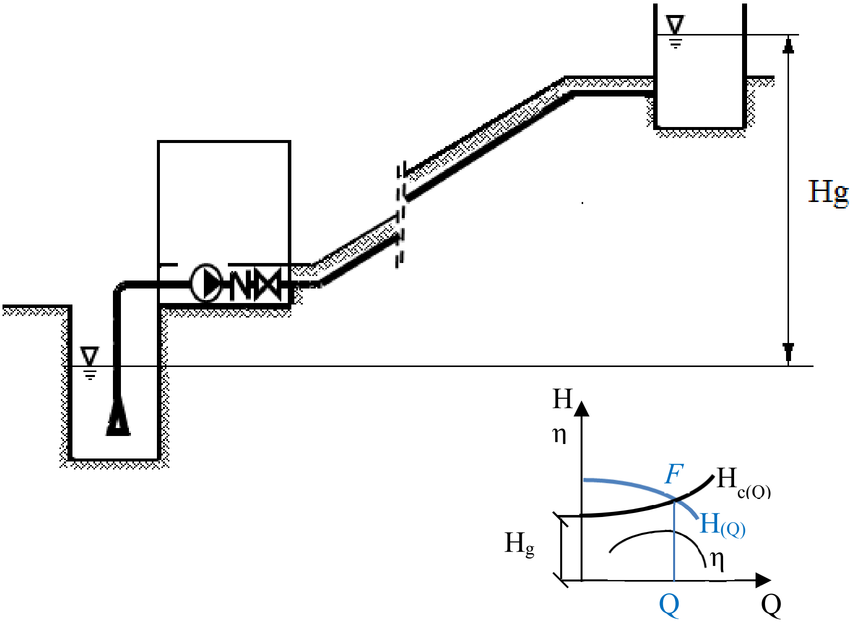

Fig. 1.1. Pumping installation. Duty point F

A pump selection is a matter of accuracy, depending on either the available pumps offered by the pump building companies or the skills of the engineer who designs the hydraulic system. A pump is chosen according to the water demand of the consumer and the maximal total head requested by the system, assessed by the designer. It is recommended the consumed power to be as low as possible.

When an installation is equipped with a single pump, this has to be chosen at its best operation point that means, at maximal efficiency. But one single pump on a system is not a good choice (unless the pump has variable speed) because the variable demand of the consumer has to be followed by the pump discharge during operation. The flow rate delivered by a constant speed pump can be varied only by controlling the opening of the valve on the discharge duct, which is an increased energy consuming method. Therefore a group of pumps working in parallel is the usual option.

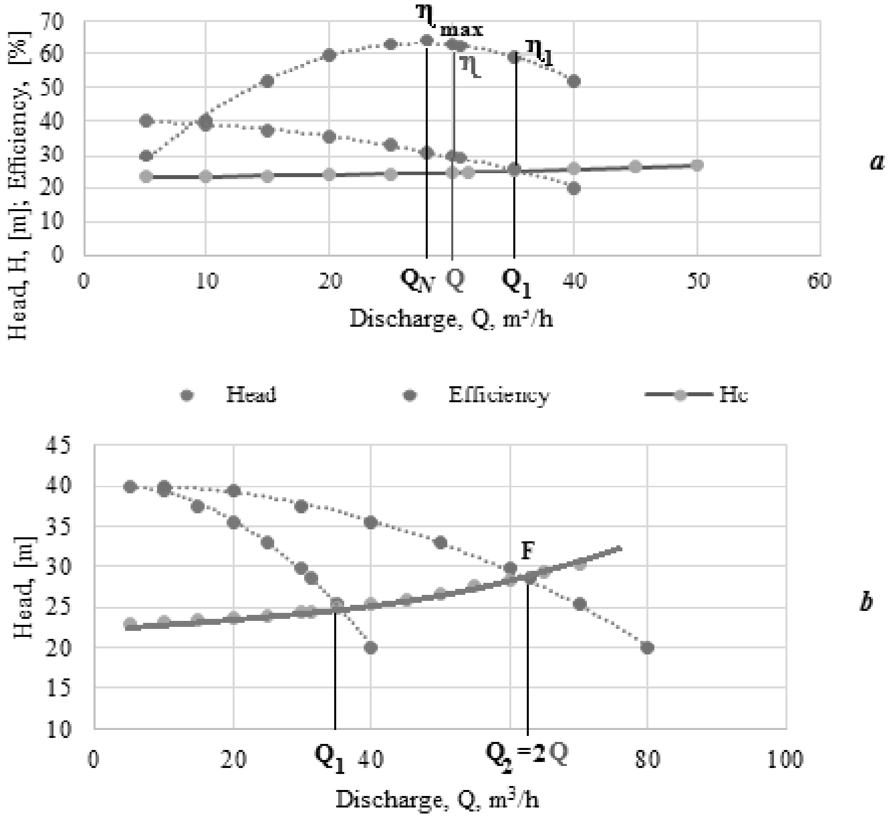

Fig. 1.2. Efficiency variation according to the discharge of the pump a.one pump operation; b. two identical pumps operating in parallel

For instance, when two identical pumps, with constant speed, operate in parallel the discharge provided by the installation can be set on two different values. When the two pumps are different, one additional value can be obtained for the discharge. Other values for the discharge can also be obtained solely by throttling.

In the case of two pumps mounted in parallel, the efficiency and the consumed power depend on whether one or two pumps are operating.

Let's consider two identical centrifugal pumps with constant speed, mounted in parallel. The valves on the discharge ducts stay completely open. The pump has been selected for a duty point with the discharge Q at the total head H and the efficiency η, as represented in Fig.1.2a. Its best operation point (BOP) is placed at a smaller discharge $Q_N < Q_1$. Its maximal efficiency is η_{max}.

When operating in parallel, the two pumps will deliver the discharge $Q_2 = 2Q$ at the head *H* that means we refer to the duty point F, in Fig.1.2b. Their efficiency will be also η, assuming the pipelines are symmetrical from hydraulic point of view. But when a single pump operates, its duty point moves to a bigger discharge,$Q_1 > Q$, thus the efficiency decreases to $\eta_1 < \eta < \eta_{max}$, Fig.1.2$a$.

The average efficiency such a group of centrifugal pumps will operate with, depends on how long they will work together. The case depicted by Fig.2 is recommended as the pumps will work in parallel a longer period than separately. Conversely, when the two pumps work in parallel a shorter period than separately, the best operation point is recommended to be placed at a bigger value of the discharge than the duty point that type of pump was selected for.

The best discharge adjustment method, from energy efficiency view point, is possible by varying the rotation speed, if the pump allows it. Variable speed pumps are expensive, but they allow a rational use of the energy during pumping installation operation.

A variable speed pump performances can be determined with the affinity laws (Burchiu 1982):

$$\frac{Q_x}{Q} = \frac{n_x}{n} \tag{1.6}$$

$$\frac{H_x}{H} = \left(\frac{n_x}{n}\right)^2 \tag{1.7}$$

$$\frac{P_x}{P} = \left(\frac{n_x}{n}\right)^3 \tag{1.8}$$

$$\eta_x = 1 - (1 - \eta)\left(\frac{n}{n_x}\right)^{0,2} \tag{1.9}$$

These laws allow us to calculate the speed n_x, the head H_x and the power P_x for a desired discharge Q_x, when all these parameters are known for a speed *n*. Usually the manufacturers build the same pump model with constant and with variable speed.

A variable speed pump can deliver the same discharge Q_3 either in the duty point F_2 at maximal speed, n_1, or in F_3, at a smaller speed, n_3, but the power is different due to the difference between the heads H_2 and H_3, Fig.1.3. The difference in power is shown by the difference between the areas of red and green rectangles in Fig.1.3. If the considered pump was a constant speed one, operating at $n_1 = ct$, at the duty point F1, its discharge could be decreased to Q_3 only by partly closing its valve on the discharge duct.

In the pumping installations equipped with variable speed pumps, two pumping methods are possible:

- by keeping the pressure proportional to the delivered flow rate (duty points F1 and F3 on a parabola shaped system curve with no static head, Fig.1.3);
- by keeping the pressure constant as the delivered flow rate varies.

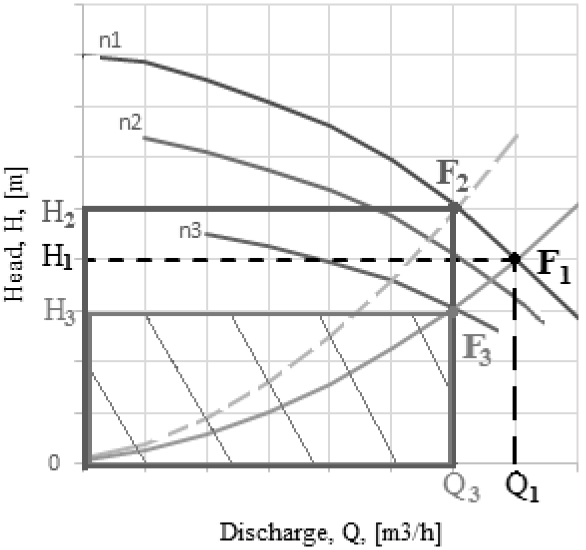

Fig. 1.3. Duty point, F_1 is homologous with F_3. If F_1 is BOP, the duty point F_3 will have a better efficiency than F_2. Example for BOP placed to the right of the duty point the pump was chosen for

1.3. Numerical simulation

Numerical simulation in EPANET is a free means for assessing the hydraulic parameters in different operation alternatives of a new designed network or an existing one that has to be modernized. It allows us to correct random sizing flaws, if any, and to determine the most appropriate and energy efficient pumping method. Simulation assisted design and operation are more and more affordable and consequently more used, therefore efforts on simulation uncertainty evaluation methods are being done (Nopens, 2016). Nevertheless simulation has to be conducted by people who have a solid background in the field.

EPANET considers all the components of a water supply system as junctions or pipes. Water demand is concentrated in junctions, therefore there is no distributed demand along the pipe. Hydraulic system's operation can be simulated as steady or unsteady and also the water quality can be investigated in different scenarios (Rossman, 2000).

The EPANET software imposes the demand flow rate in the junctions of the network and calculates the required head values. The results with respect to pressure, velocity, flow can be collected as fields of data or as time series.

Smârdan village drinking water distribution network has been chosen as study case, in order to be modernized. This village is located, at a relatively low and uniform elevation, close to the Danube, Fig. 4.

The water distribution network in Smârdan is a looped type, directly supplied by a pumping station (NP 133-2013). The underground pipes follow the streets direction in the village, as they are shown in Fig.4.

The sizing flow rate is 17.03 l/s, in accordance with the number of inhabitants, fire water volume and the developing perspective of the village (NP 133-2013).

Fig. 1.4. Village Smârdan, on the Danube river side

It represents 12% of the maximal water demand during a day. A high variation of the water demand during a day is specific for a rural settlement. According to the recommendations (SR 1343-1/2006), the standard hourly water demand variation indicates thirteen different discharge values which should be provided by the pumping station during a day time.

The simulation was carried out for the existing configuration of the network-looped network. A second configuration was taken into account: branched network, aiming to compare them. All the metallic pipes were replaced by PEHD pipes.

For each of the two configurations, simulation was done considering the network supplied by:

- two identical constant speed pumps,
- two identical variable speed pumps.

Hydraulic analysis was made during 24 hours.

The constant speed pump selected for the looped network gives the discharge of 30.65 m^3/h at a total head of 29m, with a efficiency of 62.4% . Its BOP is at 30 m^3/h with an efficiency of 63%. The constant speed pump selected for the branched network gives the same discharge of 30.65 m^3/h at a total head of 23m, with a smaller efficiency of 59.5%. Its BOP is at a bigger discharge, of 38.6 m^3/h, with the same efficiency of 63%. The variable speed pumps were considered the same model, and with respectively the same performances at maximal rotation speed as those with constant speed.

1.4. Simulation results. Discussion

The simulation for either looped or branched network supplied by constant or variable speed pumps led to a complete image of the hydraulic parameters. Smârdan proved to be a low pressure network.

In the case of looped network supplied by constant speed pumps, pressure field showed that during night time, when the demand is very low, pressure in nodes is high, reaching 41,4 mwc , which is below the upper limit of 60mwc (SR 1343-1/2006).

The existing looped configuration is represented in Fig.15. The corresponding hydraulic resistance modulus for the looped network is $M_l = 80900\ [m^{-5}s^2]$.

The velocity field revealed a variation between 0.43 to 0.81 m/s. During the night when the demand is low, velocity decreases down to 0.04 m/s in a few peripheral pipes.

A special attention was paid to the furthest consumer, i.e. node 25, with a base demand of 1.72 l/s. The demand variation during 24 hours is graphically given in Fig.1.6 a. The constant speed pumps were chosen such way the pressure in this node to be at least 7mwc, as imposed for the hydrants.

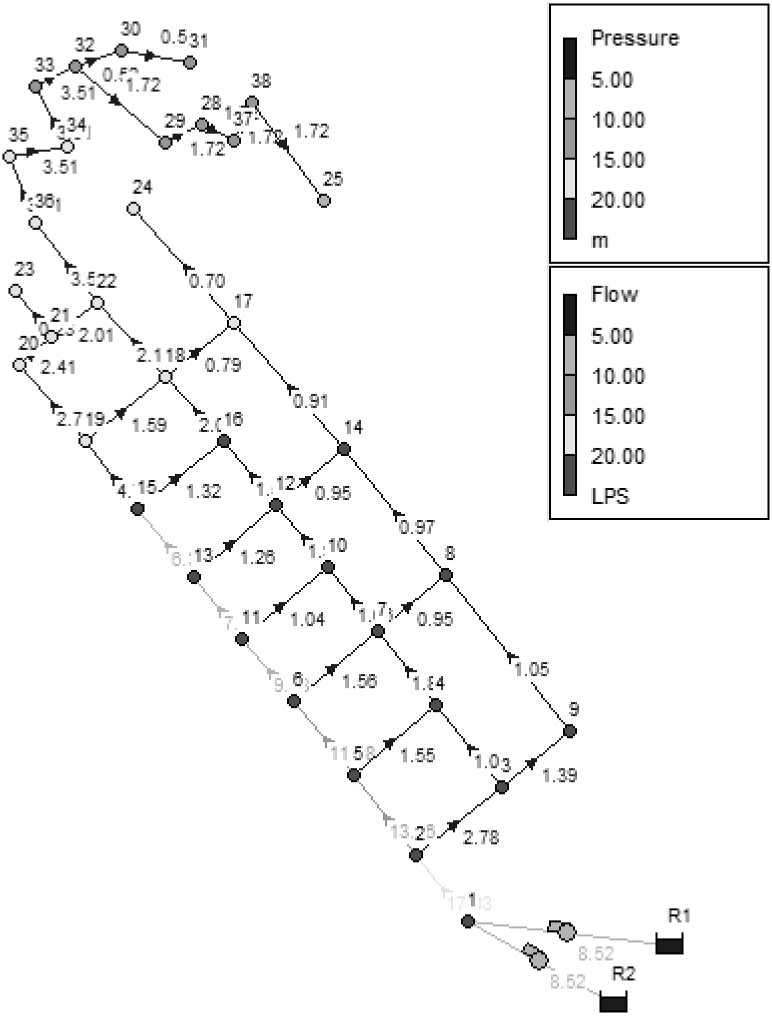

Fig. 1.5. Looped network configuration. Pressure and flow fields at maximal demand hour (7:00 am); constant speed pumps

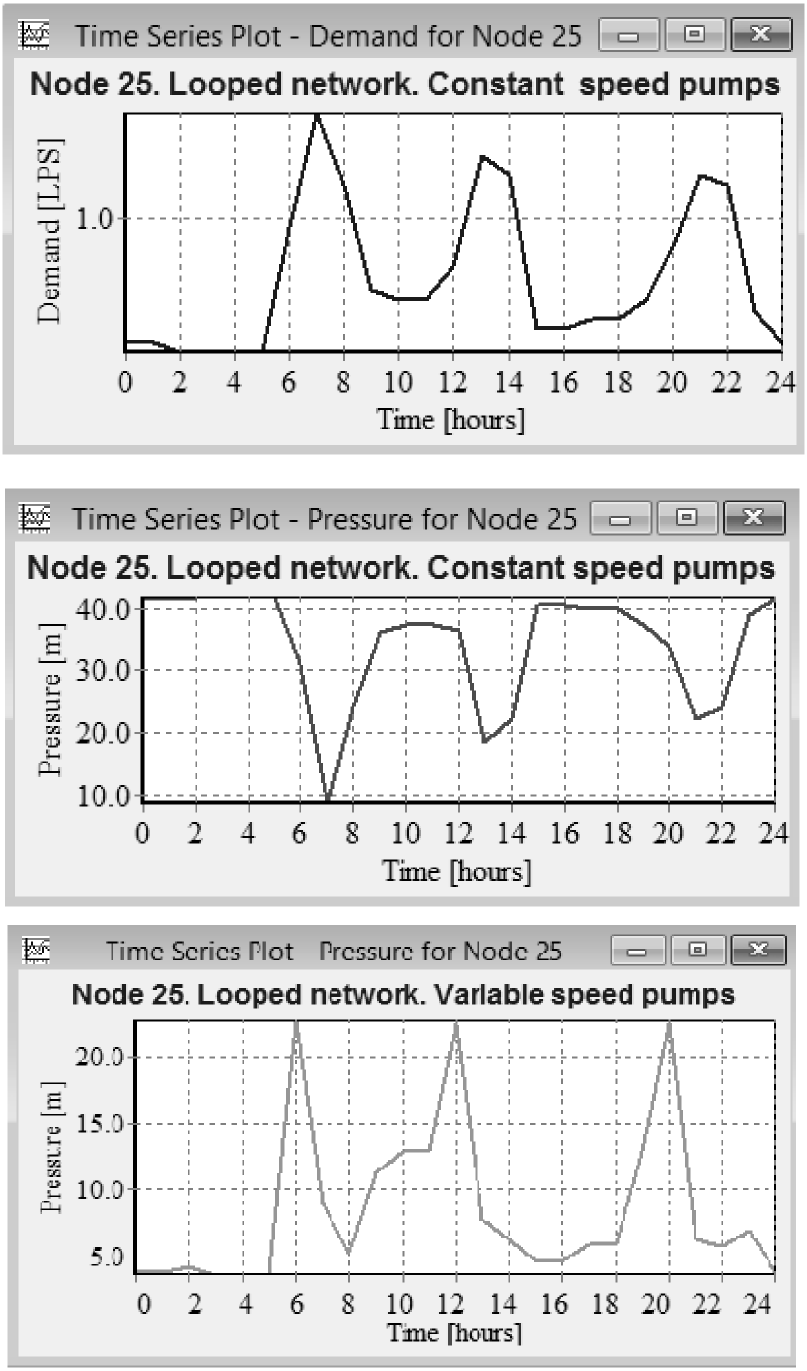

Fig. 1.6. Discharge and pressure variation in node 25 (the furthest consumer)

Pressure variation in node 25 is inversely proportional to the demand, characteristic for constant speed pumps, as it may be seen in Fig.1.6. When variable speed pumps are used, pressure is proportional to the discharge.

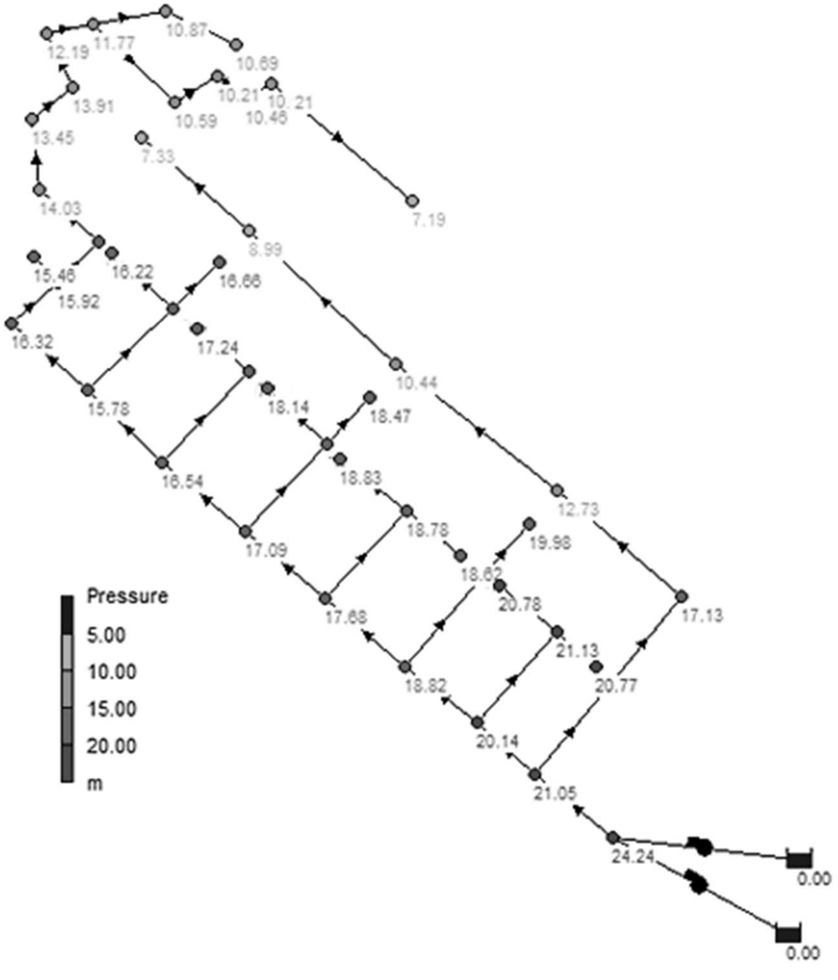

Fig. 1.7. Branched network configuration. Pressure field at maximal demand hour (7:00 am); constant speed pumps

The branched variant, represented in Fig.1.7, has 10 additional junctions compared to the looped one. The hydraulic resistance modulus for the branched network is much smaller $M_b = 60100\ [m^{-5}s^2]$, which allowed us to select a pump model with a smaller head, 23m instead of 29m, at the same discharge.

Consequently the consumed energy decreased, even if the efficiency of the new type of pump is less: only 59.5% instead of 62.4%.

In the case variable speed pumps are used, average pressure decreases and, furthermore, its variation is directly proportional to the demand. In Fig.1.7c it is represented the pressure variation in node 25 for variable speed pumps operating at different speeds, in the proportional way (pressure directly proportional to the discharge). The speed values have been determined by the use of affinity laws. The pressure decreased under the minimal admitted value during night time, therefore, during these intervals the speed had to be increased.

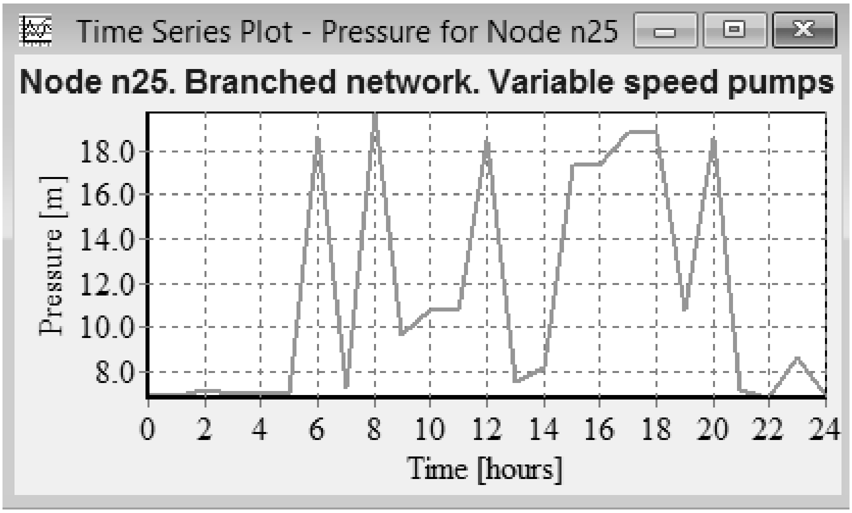

Fig. 1.8. Pressure variation in in node 25. Branched network, variable speed pumps

In Fig.1.8 there is represented the pressure variation in node 25 in the case the lower speed value is limited such way the minimal pressure is kept above 7mwc. The minimal speed is $n_3 = 0.78 \cdot n_{max}$ when both pumps operate. For the low demand values, when only one pump operates, the speed decreases to $n_{min} = 0.40 \cdot n_{max}$.

In EPANET, the controls written to simulate pumps operation takes into account that the number of pumps and their rotation speed vary according to the demand pattern.

Only four of the duty points need both pumps to operate in parallel, as represented in Fig.1.9.

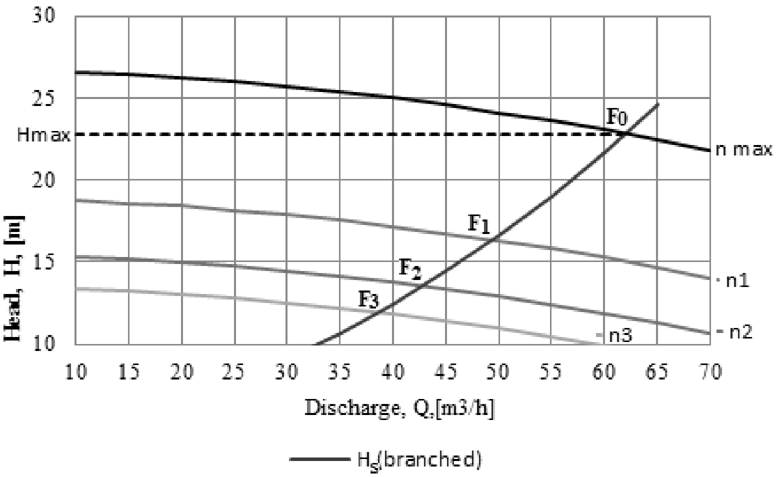

Fig. 1.9. Branched network, variable speed pumps. The duty points where the two pumps operate in parallel

In order to compare the four cases of simulation, the total head values are provided in Table 1.1.

Table. 1.1. Duty points for looped and branched network

Discharge, Q[l/s]												
0.68	1.36	2.21	2.9	4.26	4.94	6.47	7.84	9.2	12.09	12.78	14.14	17.03
Total head, H,[m] Constant speed pumps, looped network												
38.49	38.3	37.9	37.4	36.1	35.3	37.15	36.51	35.7	33.69	33.12	31.9	28.91
Total head, H,[m] Constant speed pumps, branched network												
31.9	31.8	31.4	31.06	30.0	29.35	30.83	30.32	29.7	28.06	27.61	26.63	24.24
Total head, H,[m] Variable speed pumps, looped network												
27.14	26.9	26.6	26.08	24.8	24.61	31.23	30.53	26.4	26.36	28.38	25.98	28.91
Total head, H,[m] Variable speed pumps, branched network												
22.87	22.7	22.4	22.03	21.0	20.84	26.12	25.57	22.2	22.23	23.84	21.92	24.24

The total head in the case of the branched network decreases with about 16%, in comparison with the looped network, considering the variable speed pumps, and the proportional pumping way, where the head is not oversized.

The electric variable frequency drives (VFDs) that supply variable frequency to the electric motor of a hydraulic pump are slightly less efficient than a basic direct on line motor due to additional eddy currents. Other types of VSDs also have additional losses, but these losses are small compared to the overall power saving (Astall 2013).

All the data regarding the energy consumption and average efficiency given by numerical simulation in EPANET are gathered in Table 1.2. According to these figures, the best variant is the branched network supplied by variable speed pumps.

In spite the efficiency decreased in the case of branched network, the specific consumed energy is smaller due to the consistent decrease of the total head.

Best operation point of the pump model used at the looped network is at a higher discharge than the discharge the pump was selected for, so the average efficiency is 62.77%, slightly higher than the pump's efficiency of 62.4%.

Table. 1.2. Energy efficiency for standard water demand during 24 hours and a sizing discharge of 61.3 m3/h

Network type	Pumps in parallel	Pump's parameters		Consumed power [kw]	Specific consumed energy [kwh/m3]	Average efficiency [%]
		Head [m]	Efficiency [%]			
Looped network	Two identical, constant speed pumps	29	62.4	4.56	0.3	62.77
	Two identical, variable speed pumps	29	62.4	2.04	0.15	62.77
Branched network	Two identical, constant speed pumps	23	59.5	3.83	0.26	59.5
	Two identical, variable speed pumps	23	59.5	1.39	0.13	59.5

1.5 Conclusions

EPANET software can process large amounts of data in a short period of time meeting the need of the engineer in charge with the technical design of a water distribution network. By a correct simulation of the network operation in different alternatives of geometry and pumping unit models, this software may be a useful means to obtaining the whole picture of the hydraulic parameters and their evolution in time.

The possibility to investigate different hydraulic system configurations and operation variants offers to the decision makers the basis to select the optimal technical alternative.

The branched configuration of the network proved to be a better solution than the looped one, speaking from the energetic view point. It provides an energy saving of about 0.02-0.03 kwh/m^3 · Its disadvantage is the fact that when a pipeline is interrupted by accident all the downstream consumers will have no drinking water.

The network supplied by variable speed pumps is more effective than the variant of constant speed pumps, in terms of energy consumption. They are expensive, therefore a high investment cost is expected, but they can follow a wide variable water demand, characteristic for small water distribution networks, with a consistent power saving. In Smârdan village considering the proportionally pumping method, the energy saving is significant because the static head of the system is small and all the duty points are approximately homologous. In the studied water distribution system, the use of variable speed pumps, operating at proportional pressure, instead of constant speed pumps, led to an energy saving of $0.15\,{}^{kWh}/_{m^3}$ that means a saving of over $50000\ {}^{kWh}/_{year}$. Besides, a decrease of the indirect environmental pollution is also to be expected.

References

Astall R., Understanding pump curves 4: variable speed, *The Australian pump magazine*, 2013, Issue 3, https://www.pumpindustry.com.au/understanding-pump-curves-4-variable-speed-the-answer-to-all-your-prayers/.

Burchiu V., *Pumping installations*, E.D.P., Bucharest 1982.

Brisbane Report, *Conclusions, Key Messages and Outcomes*, World Water Congress & Exhibition, 2016.

Constantin, A., Hydraulic simulation of water distribution network in rural area - first stage in water infrastructure improvement, *16th International Multidisciplinary Scientific GeoConference SGEM 2016, www.sgem.org, SGEM2016 Conference Proceedings,* Book 3 Vol. 1, pp. 415-422.

Constantin A, Niţescu C. S., Stănescu M., *Hydraulic machinery and pumping stations*, Ovidius University Press, Constanţa 2011.

Constantin A., Niţescu C. S., Stănescu M., *Energetic Efficiency Analysis of Water Pumping Installations, Recent Researches in Energy Environment and Sustainable Development*, Proceedings of the 6th WSEAS International Conference on Energy Planning, Energy Saving, Environmental Education (EPESE'12), Vol 3, Porto 2012, pp. 82-87.

Nopens Ingmar et al., *Modelling and Integrated Assessment (MIA)*, Global Trends and Challenges in Water science, Research and Management, International Water Association Alliance House, London 2016, pp. 86-89.

NP 133-2013 *Regulation regarding the design, execution and exploitation of water distribution systems*, Bucharest 2013.

Rossman L., EPANET 2 *User Manual*, Water Supply and Water Resources Division National Risk Management Research Laboratory, US, 2000.

SR 1343-1/2006 *Water supplies. Calculation of drinking water supply quantities in urban and rural sites*.

2. Dynamic numerical analysis of the integrated shear connection

Maciej Major[1], Paweł Helbrych[2]

[1,2] Politechnika Częstochowska, Wydział Budownictwa, Częstochowa, Polska

2.1. Introduction

Development of integrated structures is closely correlated with the development of technologies to obtain framing structures, where integrated components are often preferred. The most frequently used and the most effective solution is integrated floor structures, with reinforced concrete slab on the fluted sheet metal is integrated with the girder made of a steel section (in typical solutions, the function of the girder is overtaken by the I beam) (Biliński, Kmita, 2009). It is necessary for the design of the integrated floors to take into consideration two stages: construction and use (Moy, Jolly, El Shihya, 1987). In the first phase, during calculation of the ultimate limit states and serviceability limit states, the functional load, weight of components and weight of concrete mixture should be also analysed. In this phase, the fluted sheet metal performs the role of the permanent formwork. In the second phase, the interrelations between the girder and the concrete slab should be evaluated, with loads compared in this phase being functional load and technological load, individual weights of structural components and finish layers. In the phase of use, the fluted sheet metal performs the role of the external reinforcement of the span reinforcement of the floor slab. In the case of typical integrated floors, the best integration of the slab with the steel section is ensured by the use of the non-welded connectors assembled mechanically, which ensures a substantial reduction of the assembly time for the whole construction component (Major, Major, 2015). The most frequently used non-welded connector is continuous connector in the form of a stripe of the fluted sheet metal with specific width or a shear connector Hilti X-HVB, both assembled by means of the nails shot with the nail gun (Thomas, O`Leary 1998).

In a study by (Nawrot, Kucharczuk, 2004), the authors presented an alternative solution in the form of the hat connectors, which their utility confirmed by the experimental examinations.

The aim of this chapter was to determine the compatibility of the numerical and experimental model by comparing the vertical displacement (slip) as a function of the applied load and the dynamic analysis of the discussed connection in which the hat-shaped connector was adopted.

2.2. Experimental tests

The PN-EN 1994-1-1 standard presents a model for examinations of connectors for integrated steel and concrete beams. According to the guidelines, the model is composed of two concrete slabs connected with the examined connectors using the steel section (I-beam). Fig. 2.1. The adequately prepared model is situated on the test stand and loaded with the axial force applied to the transverse upper surfaces of the I-beam, thus forcing the shear force in the integration plane. For individual increments of the axial force, the measurements of vertical displacements occurring in the plane of contact of the concrete slabs with the steel section are made. The measured slips are used to evaluate the capacity and ductility of the connector. According to the PN-EN 1994-1-1 standard, the ductile connectors are those with sufficient deformation capacity to justify the assumption of ideal plastic behaviour of the shear connection in the structure considered, whereas those that do not meet this assumption are considered as non-ductile.

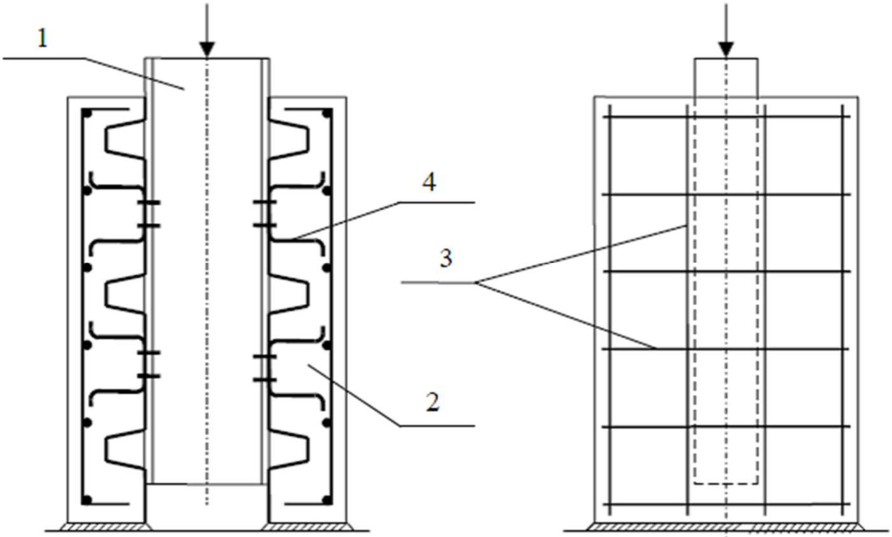

Fig. 2.1. Model of shear connector: 1- steel section, 2 - concrete slab on fluted sheet, 3 – slab reinforcement, 4 - connector tested (photo Nawrot, Kucharczuk, 2004)

The experimental tests were performed for three models with 100 mm connectors and three similar models with 60 mm connector. Figure 2.2 presents a geometry of the connector.

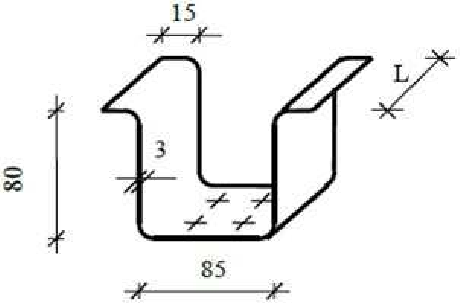

Fig. 2.2. Hat-shaped connector (photo Nawrot, Kucharczuk, 2004)

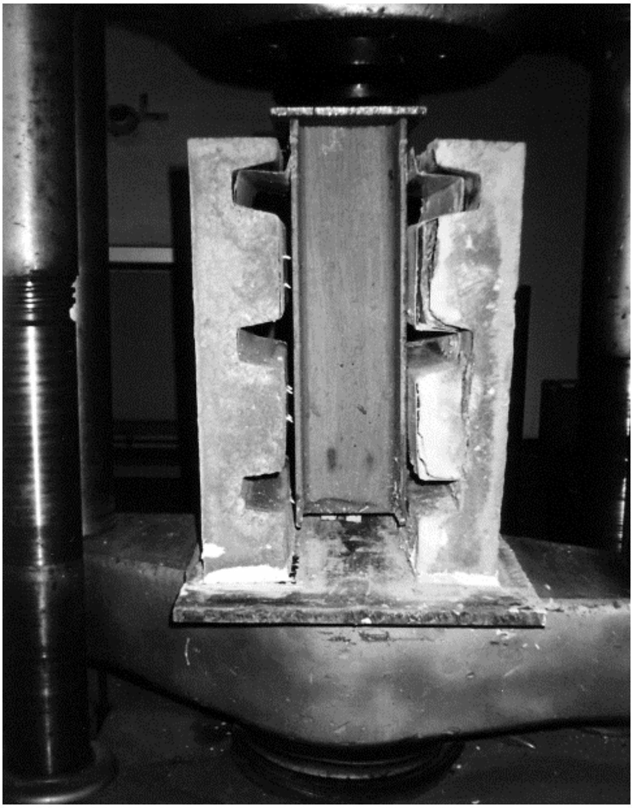

Fig. 2.3. Form of the destruction of the examined shear connection (photo Nawrot, Kucharczuk, 2004)

The models were prepared for the following geometrical and material data:

a) steel section:

- type: HEA 160,
- steel S235.

b) concreted slab:

- dimensions: 105x400x550 mm,
- concrete C25/30,
- reinforcement Ø 10, steel AII,
- trapezoidal metal sheet T55x188, thickness 0.75 mm.

c) hat-shaped connector:

- geometry according (Fig. 2.2),
- steel S235,
- 4 x nail Ø 4.5 ENP Hilti.

During the experiment, the capacity of the connectors and slips in the model were evaluated and the forms of destruction of the connection were analysed (see Fig. 2.3).

2.3. Numerical model of the connection

Numerical calculations were performed using the ANSYS software based on the finite element method. All the elements of the shear model were made as 10-node Solid elements. The model was loaded with its own weight and the force distributed on the upper surface of the I-beam HEA160. The support was modelled as a movable support (Fig. 2.4).

An elastic-plastic model was adopted for the HEA160 section, with the following parameters:

- density: 7.850 kg/m^3,
- Poison's ratio: 0.3,
- Young's modulus: 210 GPa,
- yield point: 292.25 MPa (determined empirically),
- ultimate tensile strength: 405.15 MPa (determined empirically).

An elastic-plastic model of material was adopted for the 60 mm hat-shaped connector, with the following parameters:

- density: 7850 kg/m^3,
- Poison's ratio: 0.3,
- Young's modulus: 210 GPa,
- yield point 332.20 MPa (determined empirically),
- ultimate tensile strength: 415.25 MPa (determined empirically).

A elastic-plastic model of material was adopted for the trapezoidal sheet metal, with the following parameters:

- density: 7850 kg/m^3,
- Poison's ratio: 0.3,
- Young's modulus: 210 GPa,
- yield point 277.25 MPa (determined empirically),
- ultimate tensile strength: 350.10 MPa (determined empirically).

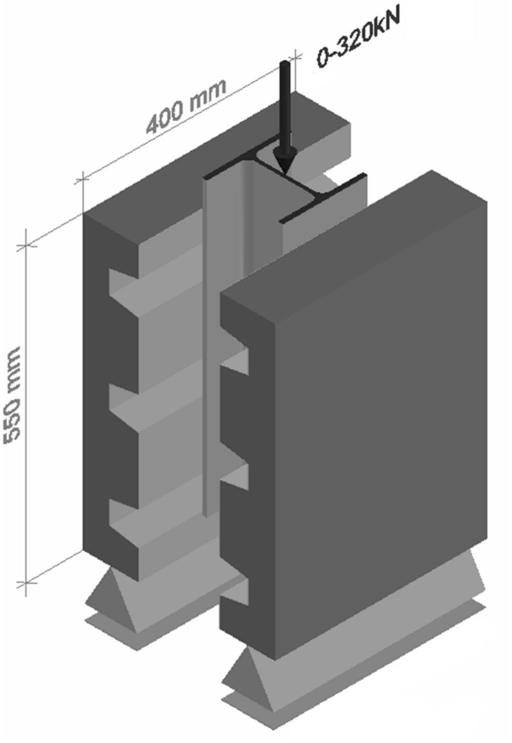

Fig. 2.4. The numerical model of the shear connection

A model of material was adopted for the concrete, with the following parameters:

- density: 2500 kg/m^3,
- Poison's ratio: 0.2,
- Young's modulus: 30 GPa,
- compression strength: 16.08 MPa.

An elastic-plastic model of material was adopted for the nails, with the following parameters:

- density: 7850 kg/m^3,
- Poison's ratio: 0.3,

- Young's modulus: 200 GPa,
- yield point 350.0 MPa,
- ultimate tensile strength: 650.0 MPa.

An elastic-plastic model of material was adopted for the reinforcement bars, with the following parameters:

- density: 7850 kg/m^3,
- Poison's ratio: 0.3,
- Young's modulus: 205 GPa,
- yield point 305.0 MPa,
- ultimate tensile strength 490 MPa.

The Tetrahedrons method was used to generate a model grid, using quadrilateral 10-node elements (see Fig. 2.5).

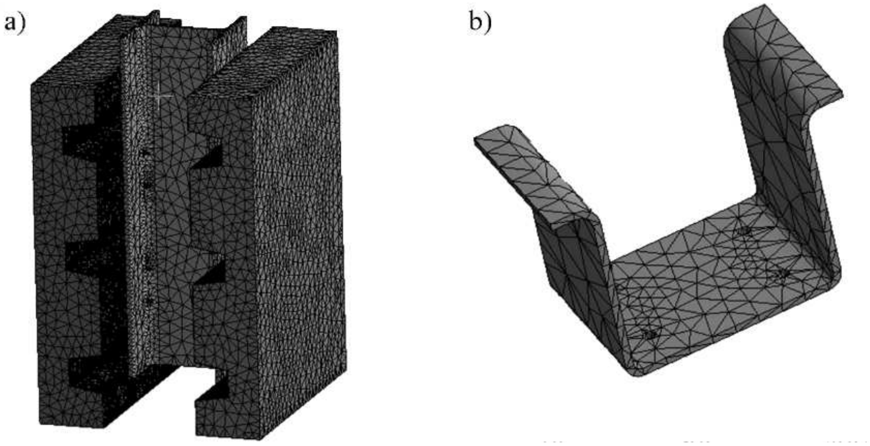

Fig. 2.5. Element grid: a) examined model, b) hat-shaped connector

2.4. Static examination of the numerical model

The model No. 6 with 60 mm hat-shaped connector, examined empirically in a study by [Nawrot, Kucharczuk, 2004] was adopted as a reference model for the numerical static examination. In order to verify the consistency of the experimental and numerical models, the comparison was made for the displacement as a function of the applied load for both models.

The experimental model and numerical models were loaded with the axial load in the range of from 0 kN to 330 kN, with the steps of 15, 10 and 5 kN. The load for the numerical model was completed for the value of the destructive force of the empirical model. The vertical displacement at the moment of the experimental model destruction was 3.50 mm and the slab was disconnected at the locations of the connectors.

Figure 2.6 presents the values of loading forces and slips for the experimental and numerical models.

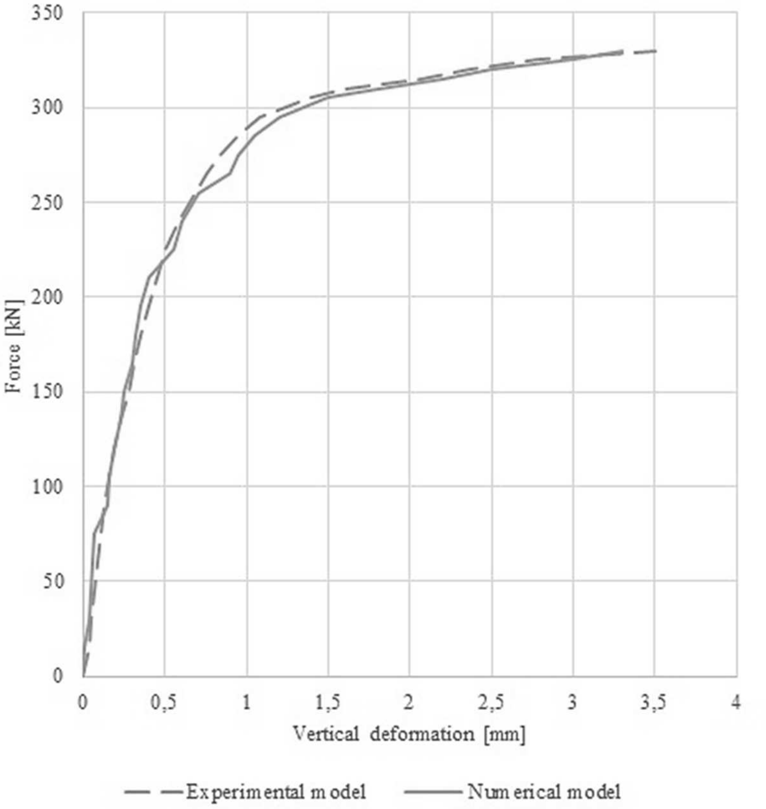

Fig. 2.6. The slip between the concrete slab and the HEA160 steel section:
a) experimental model b) numerical model

For the numerical model, the highest vertical deformation (slip in the plane of contact of the HEA160 I-beam with the concrete slab) was established for the maximal shear force of 330 kN and was 3.38 mm. The slips obtained for individual values of loading forces in the numerical model can be regarded as consistent with the results of the experiments, which suggest the adequate modelling of the shear connector in the numerical analysis.

The greatest overall deformation in the numerical model was observed for the sheet metal at the contact with the concrete slab for the maximal shear force of 330 kN. Furthermore, the trapezoidal sheet metal was disconnected from the concrete slab as shown in Fig. 2.7, whereas Fig. 2.8 illustrates overall deformations in the experimental model.

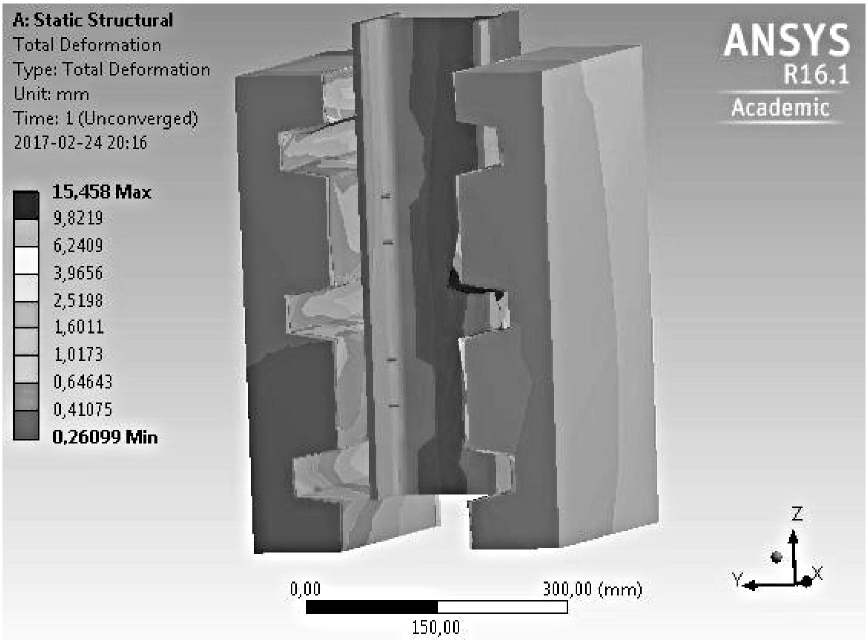

Fig. 2.7. General deformations of the analysed numerical model of the shear connection

In the numerical model, the locations of concentration of shear stresses are near the lower wall of the hat-shaped connectors in the area of integration of the I-beam with the concrete slab, see Fig. 2.9a

Furthermore, the maximal shear stresses (381.54 MPa, see Fig. 2.9b) in the hat-shaped integration connector were observed in the location of the contact between the horizontal and vertical walls of the connector. Tensile strength of the connector was not exceeded, whereas this was the case for the yield point, which is consistent with the experimental tests, where the connector was plastically deformed, but the material was not broken.

Fig. 2.8. General deformations of the analysed experimental model of the shear connection (photo Nawrot, Kucharczuk, 2004)

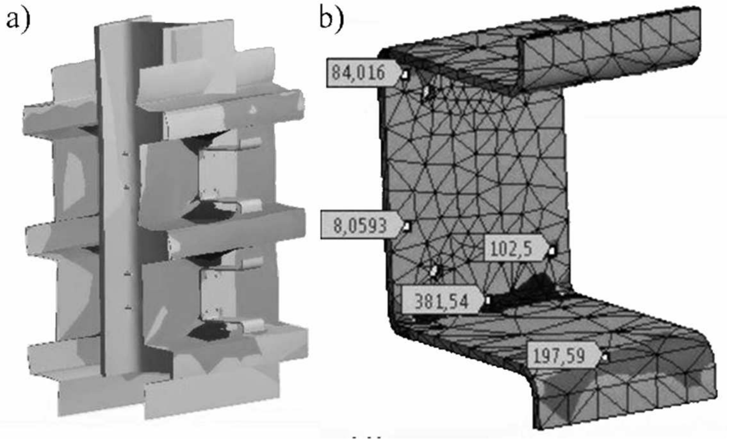

Fig. 2.9. Shear stresses in the numerical model: a) locations of stresses concentration, b) shear stresses in the connector

2.5. Dynamic examination of the numerical model

After the initial numerical analysis of the shear model of the integrated connection and obtaining the consistency of the results of the slips of the steel I-beam (HEA160) with the experimental and numerical analyses, the dynamic analysis of the model of the shear connection was conducted. The numerical model was loaded for 9 times with the axial force, with initial value of the axial force of 50 kN, incremented with five steps of 300 kN and the sixth step of 20 kN to the level of 320 kN. Next two steps were reducing the loading force to the values of 300kN and 200kN, respectively. Total time of the application of the axial force was 9.1×10^{-5} s, whereas total time of load analysis was 4×10^{-4} s. The range of values of load with the axial forces is identical in its value to the static load in the experimental examinations for the model No. 5, whereas time of its effect was selected for the speed of sound wave propagation in the solid body under normal conditions of 5.100 m/s. The design of the load to the numerical model is presented in Fig. 2.10.

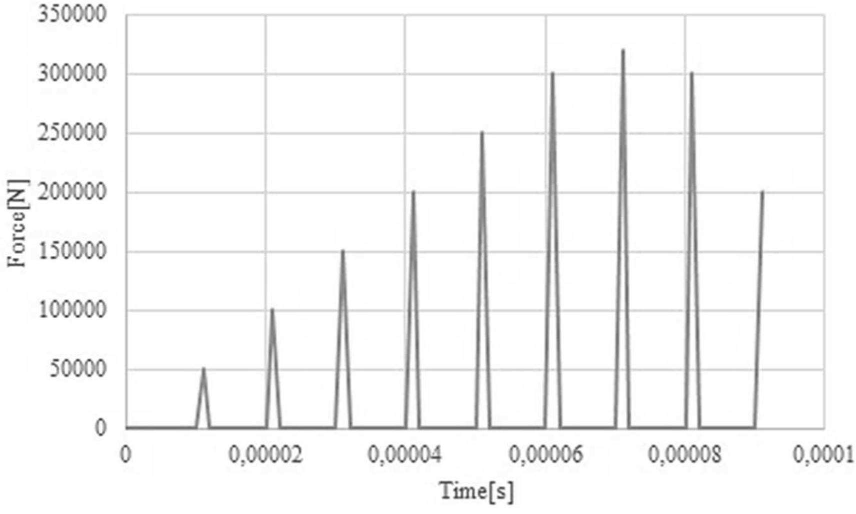

Fig. 2.10. Design of the load to the numerical model

In the loading phase, i.e. in the period from 0 to 9.1×10^{-5} the layered distribution of stresses was observed, with no maximal stresses obtained for the time of analysis. Maximal stresses in this period were 109.3 MPa. It is also noticeable that stresses are transferred through the connectors to the concrete slabs (Fig. 2.11).

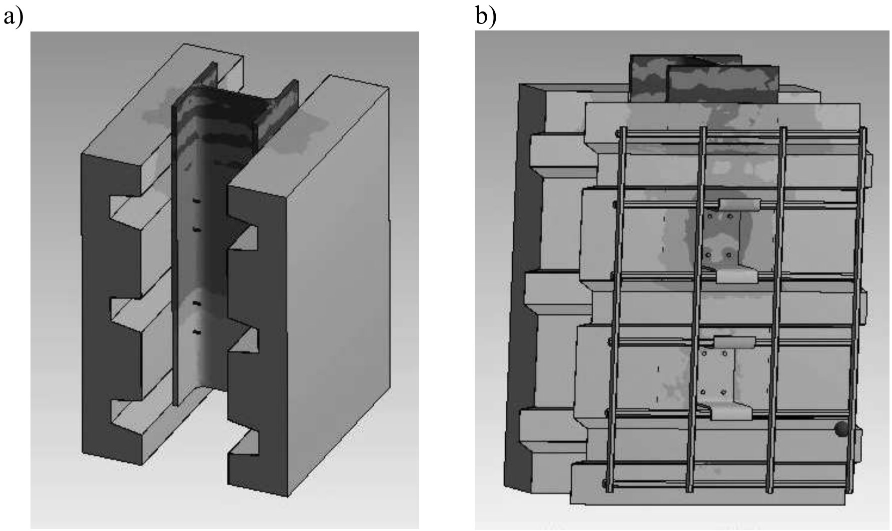

Fig. 2.11. Distribution of stresses in the model studied in the loading phase: a) view of the whole model, b) view without concrete slab

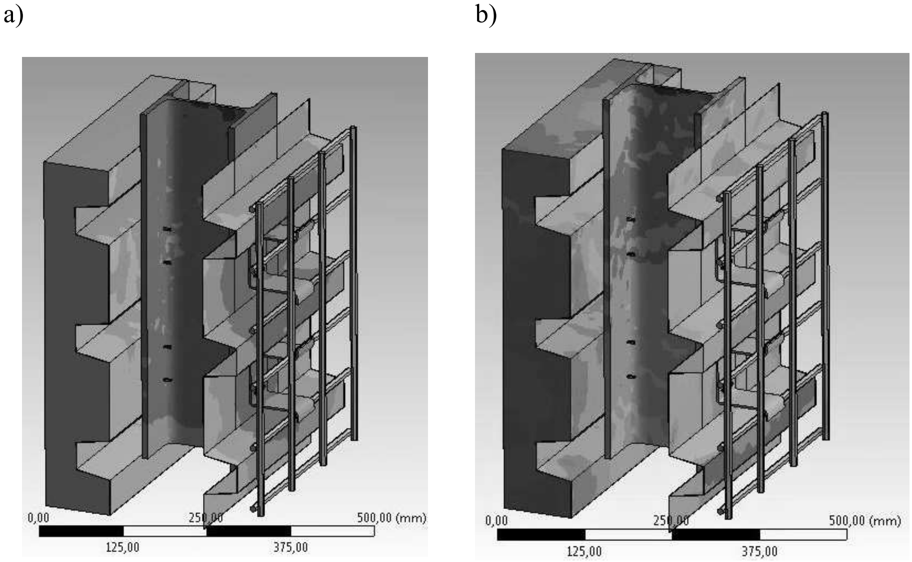

Fig. 2.12. Distribution of stresses in the model in the phase of analysis: a) distribution of stresses for 1.6×10^{-4} s, b) distribution of stresses for 3.2×10^{-4} s

In the initial phase of the analysis, i.e. from 9.1×10^{-5} s to 2×10^{-4} s, a uniform distribution of stresses was observed in the whole model and the spectrum of load effect was extended in the concrete slab (see Fig. 2.12a); for the analysis time of 1.6×10^{-4} s, the maximal shear stresses were 201.77 MPa.

In the final phase of the analysis, i.e. from 2×10^{-4} s to 4×10^{-4} s, scattering of the wave of shear stress and gradual reduction of the stress value in the function of time were observed in the model (see Fig. 2.12b).

Analysis of the distribution of shear stresses in the connector revealed their concentration near the holes for nails, with maximal values of stresses observed at the same time for the whole model i.e. 1.6×10^{-4} s, reaching 63.8 MPa (Fig. 2.13).

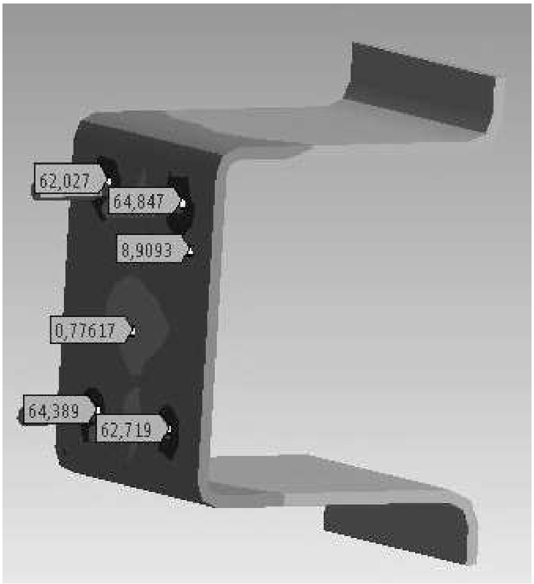

Fig. 2.13. Distribution of shear stresses in the hat-shaped connector

Values of maximal shear stresses vs time are presented in Fig. 2.14.

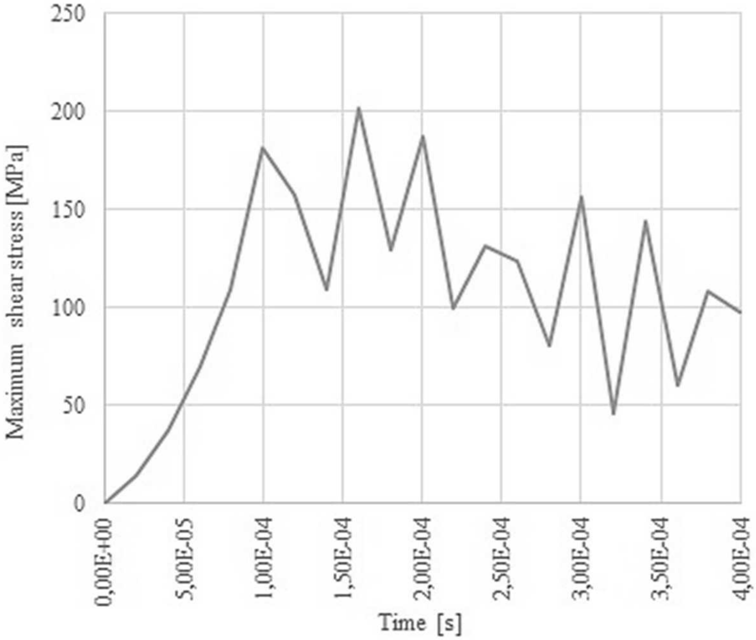

Fig. 2.14. Design of the load to the numerical model

2.6. Conclusions

The numerical model correctly maps the behavior of a shear connection made using a hat-shaped connector. The shear stresses for the numerical model were consistent with the results obtained in the experimental studies. A high convergence of slip curves for both methods was obtained, with a maximum difference of 4.4%. Shear stresses in all model elements did not exceed the limit values either for the experimental or numerical analyses. Yield of the hat-shaped connector was not observed in the dynamic analysis. The proposed numerical model can be used to pre-verify different variants of the connector geometry to optimize its shape.

References

Biliński T., Kmita J., *Dorobek nauki polskiej w zakresie konstrukcji zespolonych.* Zielona Góra: Oficyna Wydawnicza Uniwersytetu Zielonogórskiego, 2009.

Bródka J., Kozłowski A., *Stalowe budynki szkieletowe*. Rzeszów: Oficyna Wydawnicza Politechniki Rzeszowskiej. 2003.

Major M., Major I. *Konstrukcje zespolone w budownictwie zrównoważonym*, Budownictwo o zoptymalizowanym potencjale energetycznym, nr (16), Częstochowa 2015, pp. 51-56.

Moy S., Jolly C., El Shihya A., *Unwelded Shear Connectors for Composite Beams*, Composite Steel Structures, London-New York, 1987, pp. 65-74.

Nawrot J., Kucharczuk W., *Badanie nośności nowych łączników do zespolonych stropów stalowo-betonowych*, Inżynieria i Budownictwo, 2004, R.60 nr 12, pp. 654-657.

PN-EN 1994-1-1 Eurokod 4 2008, *.Projektowanie zespolonych konstrukcji stalowo-betonowych*, Część 1-1: Reguły ogólne i reguły dla budynków, Bruksela.

Thomas D., O`Leary D.C., *Composite beams with profiled-steel sheeting and non welded shear connectors*, Steel Construction To-day, 1998, Vol. 2 No. 4, pp. 117-121.

3. Effect of carbon nanotubes on the mechanical fracture properties of alkali-activated materials

Pavel Rovnaník, Hana Šimonová, Libor Topolář, Pavel Schmid, Zbyněk Keršner
Brno University of Technology, Faculty of Civil Engineering, Brno, Czech Republic

3.1. Introduction

The development of infrastructure leads to an increase in the demand for natural resources, which are limited, and the building industry in particular consumes a huge amount of raw materials for the production of building materials. Ordinary Portland Cement (OPC) will remain a key player in the future, although its production is energy demanding and contributes to the ongoing increase in global CO_2 emissions. There are two possible ways of reducing the negative impact of the building industry. One way is to utilize secondary raw materials as supplementary cementing materials, among which blast furnace slag is the most effective at reducing CO_2 footprint (Keun-Hyeok 2015). The other way is to utilize alkali-activated concrete. This type of material is even more effective in reducing CO_2 emissions and energy consumption. Different sources show that the global warming potential of alkali-activated concrete is approximately 40–70% lower than that of OPC concrete (McLellan 2011, Keun-Hyeok 2013).

Alkali activation was introduced and brought into practice by Gluchovsky (Gluchovsky 1959). It is a reaction of siliceous material which contains a highly reactive vitreous phase (blast furnace slag, fly ash, metakaolin, silica fume etc.) with alkali activator, usually alkaline hydroxide, silicate or carbonate, which is added either in the form of a solution or a soluble solid. Davidovits who working on numerous aluminosilicate-based formulations from early 1980s named these materials 'Geopolymers' (Davidovits 1982). The mechanical properties and application possibilities of alkali-activated materials, especially with slag as aluminisilicate precursor, are very similar to those of OPC concrete. However, in contrast to OPC-based binders, these materials offer superior properties such as higher corrosion resistance against acid or sulphate attack (Bakharev 2005, Rovnaníková 2002) and also higher resistance to elevated temperatures and fire (Rovnaník 2013, Lyon 1997). The major disadvantage is increased shrinkage. This effect is caused by both autogenous and drying shrinkage and finally results in volume contraction, micro-cracking and the deterioration of tensile and bending properties (Shi 2006).

Multi-walled carbon nanotubes (MWCNTs) exhibit extraordinary mechanical properties, with the Young's modulus of an individual nanotube being around 1 TPa and tensile stresses being in the range of 65–93 GPa (Belytschko 2002). MWCNTs are thus the most promising nanomaterials for enhancing the mechanical fracture properties of building materials, and their resistance to crack propagation. Some problems have appeared connected with the aggregation of MWCNTs, which reduces the efficiency of single nanotubes. Nevertheless, effective dispersion can be achieved by applying ultrasonic or high shear rate mechanical dispersion with the use of a surfactant (Konsta-Gdoutos 2010-1).

The main aim of this work is to apply MWCNTs as a shrinkage reducing admixture for alkali-activated materials. Regarding the properties of MWCNTs, they have a great potential to reduce the cracking tendency of silicate-based materials caused by autogenous and drying shrinkage, which is one of the essential problems arising during the practical application of materials in the building industry (Sanchez 2010, Konsta-Gdoutos 2010-2).

Since microcracks have a strong negative effect on mechanical performance, the efficiency of MWCNTs as a potential nanoscale reinforcement and shrinkage reducing agent can be monitored by the fracture behaviour of the composite material and by acoustic emission methods. In this study, fracture testing and acoustic methods were applied to determine the performance of MWCNTs in mortars with three different types of basic binder: alkali-activated slag, fly ash geopolymer and metakaolin geopolymer.

3.2. Materials and methods

The alkali-activated materials were composed of basic aluminosilicate precursor and water glass as alkaline activator. Among plenty of reactive aluminosilicate materials three basic and the most common commercially available were chosen. Two of them are considered secondary raw materials (granulated blast furnace slag, coal fly ash) and one is primary product (metakaolin). The chemical composition of aluminosilicate precursors together with the fineness is introduced in Table 3.1. A commercial sodium silicate solution with SiO_2/Na_2O = 1.6 and 43 wt% of dry mass was used as an activator. Quartz sand with a maximum grain size of 2.5 mm was used as aggregate. Multi-walled carbon nanotubes (Graphistrength® CW 2-45, Arkema, France) were used as received. Since MWCNTs are commonly not water-soluble, the received MWCNTs already contained 55% of carboxymethyl cellulose as a dispersing agent. Carbon nanotubes were used in the form of 1 and 5% dispersions. In order to prepare the aqueous dispersions, the procedure prescribed by the producer was followed. MWCNT pellets were dissolved in hot water and dispersed bundles of MWCNTs were further disintegrated by mechanical homogenizer (3 h at 14000 rpm).

Table. 3.1. Chemical composition and characteristics of aluminosilicate precursors

Material	Slag	Fly ash	Metakaolin
SiO2 (%)	39.66	49.82	55.01
Al2O3 (%)	6.45	24.67	40.94
Fe2O3 (%)	0.47	7.05	0.55
CaO (%)	40.12	3.91	0.14
MgO (%)	9.50	2.68	0.34
Na2O (%)	0.33	0.70	0.09
K2O (%)	0.55	2.78	0.60
d10 (μm)	5.2	9.1	3.4
d50 (μm)	15.5	60.7	6.3
d90 (μm)	38.3	200.4	11.6

The mixture composition is given in Table 3.2. The MWCNT content was 0.05, 0.10, 0.15, and 0.20% of the weight of the solid aluminosilicate, and the results of the tests were compared with a reference mixture, which was prepared without MWCNTs but following the same procedure. The mixtures were cast into 40 × 40 × 160 mm prismatic moulds and left to set. The curing process differed for different types of basic material. Metakaolin and fly ash geopolymer specimens were covered with plastic sealant directly after casting to keep moisture in the fresh material. Meanwhile metakaolin geopolymer was treated only at ambient temperature, the moulds with fly ash geopolymer were kept at first at ambient temperature for 3 days and then heated at 60 °C for 24 h. After demoulding the hardened specimens were stored in the laboratory conditions (22 ± 2 °C, $\varphi = 45 \pm 5\%$) till the age of 28 days. Alkali-activated slag set within 24 hrs and the hardened samples were immersed in water for 27 days, then pulled out of the water and allowed to dry spontaneously under ambient conditions for 24 hrs prior to fracture testing. Samples are identified with the following designation: (aluminosilicate matrix) (percentage of MWCNTs). For example, sample of fly ash geopolymer with 0.1% of MWCNTs is identified as FAG 0.10.

Experiments were carried out on a Heckert FP 10 mechanical testing machine with the measuring range 0–2000 N. During the experiment, the three-point bending test was performed on specimens with a central edge notch cut to about 1/3 of specimen depth. The load span was 120 mm. The effective crack extension method was used to evaluate a load–deflection (*F–d*) diagrams. The *F–d* diagram was used for the calculation of elasticity modulus from the first (almost linear) part of the diagram, and for the calculation of effective fracture toughness and specific fracture energy. The effective fracture toughness values were determined using the Effective Crack Model (Karihaloo 1995), which combines linear elastic fracture mechanics and the crack length approach. Estimations of fracture energy values according to the RILEM method were calculated using a 'work of fracture' value (RILEM 1985). Informative compressive strength values were also determined for all specimens on the fragments remaining after the fracture experiments had been performed.

Table. 3.2. Mix composition of alkali-activated materials with MWCNTs

Material	Component	MWCNTs content				
		0%	0.05%	0.10%	0.15%	0.20%
AAS	Slag (g)	450				
	Sodium silicate (g)	180				
	Sand (g)	1350				
	1% MWCNTs (g)	0	22.5	45	67.5	90
	Water (ml)	95	72.5	50	27.5	5
FAG	Fly ash (g)	350				
	Sodium silicate (g)	280				
	Sand (g)	1050				
	1% MWCNTs (g)	0	17.5	35	52.5	70
	Water (ml)	70	52.5	35	17.5	0
MKG	Metakaolin (g)	350				
	Sodium silicate (g)	350				
	Sand (g)	1050				
	1% MWCNTs (g)	0	17.5	35	52.5	70
	Water (ml)	120	103.5	85	67.5	50

The initiation of cracks during the fracture tests was also monitored via the acoustic emission (AE) method. AE is the term for the noise emitted by materials and structures when they are subjected to stress. Stresses can be mechanical, thermal or chemical in nature. The noise emission is caused by the rapid release of energy within a material due to events such as crack formation that occur under applied stress, generating transient elastic waves which can be detected by piezoelectric sensors. In this case the AE method detects and characterizes the development of the fracture cracking process and only evaluates the damaging activity while it is occurring (Grosse 2008). A guard sensor eliminated mechanical and electrical noise. Four acoustic emission sensors were attached to the surface of the specimen with beeswax (Fig. 3.1). Acoustic emission signals were recorded by DAKEL XEDO measuring equipment with four IDK-09 acoustic emission sensors with a 35 dB preamplifier.

When monitoring the cracking tendency of AAS mortar during hardening, fresh slurry was placed into a cylindrical mould. A steel waveguide was then inserted into the slurry and the AE sensor was attached to its free end with beeswax (Fig. 3.1). The intensity threshold of the signals that were detected was set to 0.8 V with 30 dB gain. This allowed us to eliminate background noise and record only the emissions produced due to the cracking of the material.

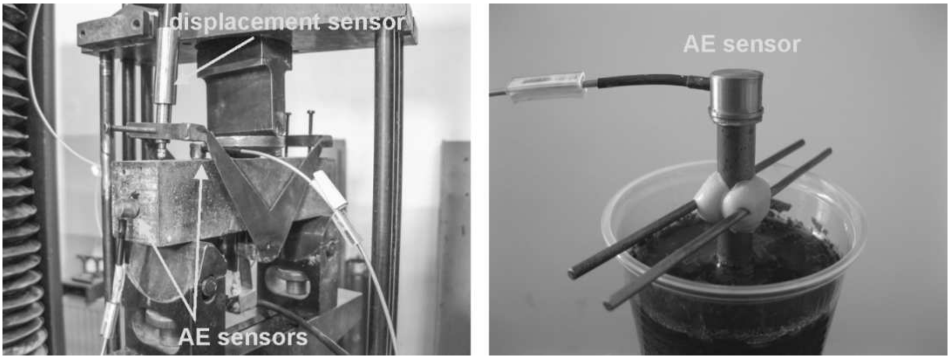

Fig. 3.1. Fracture test configuration in testing machine (left), measurement of AE activity during hardening (right)

3.4. Results and discussion

Basic mechanical and fracture parameters (mean values) of alkali-activated materials are listed in Table 3.3. Alkali-activated slag exhibits the best mechanical properties among all three tested materials, and the values are comparable with those observed for Portland cement mortars (Rovnaník 2008). On the other hand, fly ash geopolymer showed the lowest values of compressive strength, modulus of elasticity and fracture toughness. Only in case of fracture energy, the minimum value was reached with metakaolin geopolymer.

Table. 3.3. Mechanical and fracture parameters of reference alkali-activated materials

Material	Compressive strength	Elasticity modulus	Fracture toughness	Fracture energy
	MPa	GPa	MPa $m^{1/2}$	J m^{-2}
AAS	61	14	0.81	34.9
FAG	11	6	0.25	27.0
MKG	42	15	0.42	7.6

The effect of MWCNTs on the different mechanical fracture properties (mean values and standard deviations) of tested alkali-activated materials is introduced in Figs. 3.2–3.5. All parameters are presented as relative values with respect to average values of the reference materials set as 100%. Addition of MWCNTs has a positive effect on the compressive strength of all composites (Fig. 3.2). The best improvement was observed for the composite based on fly ash geopolymer, because the strength increased with addition of 0.05%, 0.10%, and 0.15% MWCNTs by 30%, 50%, and 70%, respectively. Generally, addition of 0.20% MWCNTs led to a rather decreasing effect on the compressive strength of all materials.

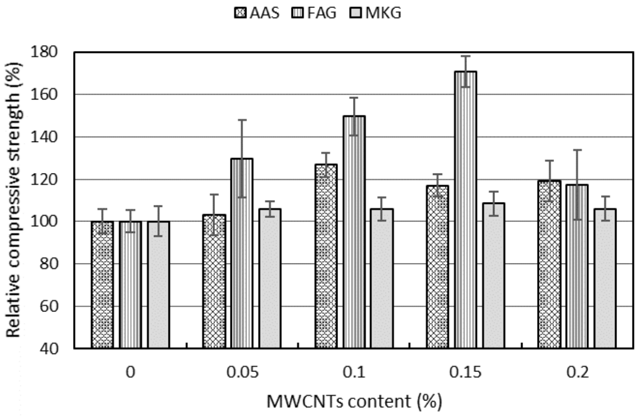

Fig. 3.2. Relative compressive strength values of alkali-activated aluminosilicate composites with various amounts of MWCNTs

When the values of elasticity modulus were compared, it turned out that MWCNTs remarkably contribute to the stiffness of AAS and FAG composites but the stiffness of MKG decreased instead (Fig. 3.3). The highest values were reached for AAS composite where even 0.05% MWCNTs was responsible for an increase in elasticity modulus of alkali-activated slag by 30% but further addition had a negligible effect. The values for the FAG composite follow similar trend as compressive strength with maximum observed for the composite containing 0.15% of MWCNTs. However, the increase was not as significant as in the case of compressive strength. On the other hand, the modulus of elasticity was reduced by up to 10% in case of MKG material, which means that MWCNTs have rather negative effect on the stiffness of metakaolin-based geopolymer materials.

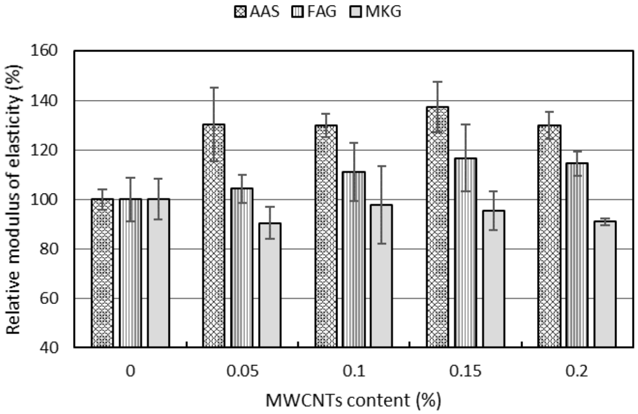

Fig. 3.3. Relative modulus of elasticity values of alkali-activated aluminosilicate composites with various amounts of MWCNTs

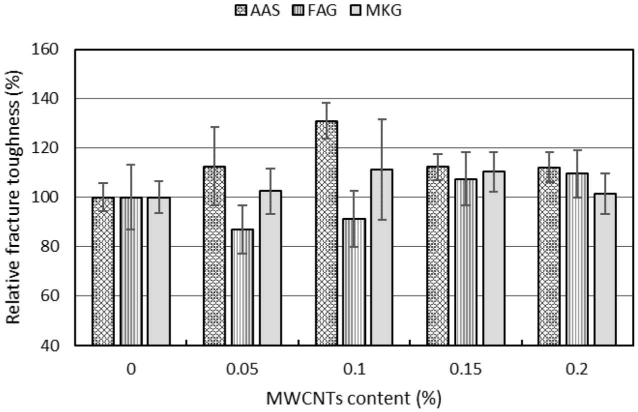

Fig. 3.4. Relative fracture toughness values of alkali-activated aluminosilicate composites with various amounts of MWCNTs

Values of effective fracture toughness of composites with MWCNTs were generally higher than those observed for reference samples with exception of fly ash geopolymer containing 0.05 and 0.10% MWCNTs (Fig. 3.4). In this case the effective fracture toughness decreased by 13 and 9%, respectively. A slight increase by 7 and 10% was detected in case of the mixtures having 0.15 and 0.20% of MWCNTs. Addition of nanotubes to MKG material improved the effective fracture toughness by 11% at its maximum which was reached for the mixture with 0.10% MWCNTs. Unfortunately, this composite showed also the highest coefficient of variation. The best improvement of the effective fracture toughness was achieved for AAS composite mixtures for which the values increased by 12–31%.

The comparison of the relative fracture energy values of alkali-activated aluminosilicate composites with various amounts of MWCNTs is presented in Fig. 3.5. This parameter exhibited the highest variability, especially in case of materials with FAG and MKG matrix. Meanwhile MWCNTs caused an improvement in fracture energy of MKG by up to 35% with 0.15% addition, they had rather adverse effect on other two composites. However, the fracture energy of pure MKG is surprisingly much lower than in case of FAG or even AAS samples. Concerning the variation coefficients, we can assume that the fracture energy of FAG is not influenced much by the addition of MWCNTs. In case of AAS, the fracture energy considerably increased only for 0.10% addition. However, with respect to high coefficients of variation of some results, it can be suggested that it follows similar trend as was observed for the fracture toughness.

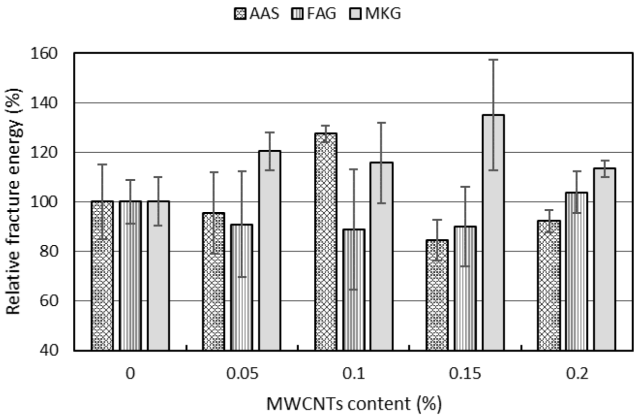

Fig. 3.5. Relative fracture energy values of alkali-activated aluminosilicate composites with various amounts of MWCNTs

Acoustic emission signals which were received during the three-point bending testing of the specimens were analysed. The attention was focused on three basic parameters: the amplitude, duration and energy of the AE signals (Figs. 3.6–3.8 – mean values and standard deviations). Different types of cracks generate different AE signals, and these differences can be related to the properties of the material (Iwanami 1997, Li 1995). Once the AE transducer captures a signal over a certain level, an AE event is recorded. The amplitude of AE signals, which is the greatest voltage measured in a waveform. This is an important parameter in AE inspection because it determines the detectability of the signal. Signals with amplitudes below the operator-defined minimum threshold are not recorded. A higher amplitude indicates the formation of a larger and more significant crack (Iwanami 1997). Amplitude values of all mixtures varied between 2489 and 3775 mV. FAG composites exhibited much higher amplitudes than AAS or MKG. However, while 0.15 and 0.2% MWCNTs caused rather significant decrease in amplitude, the variation in values of AAS and MKG composites was quite small.

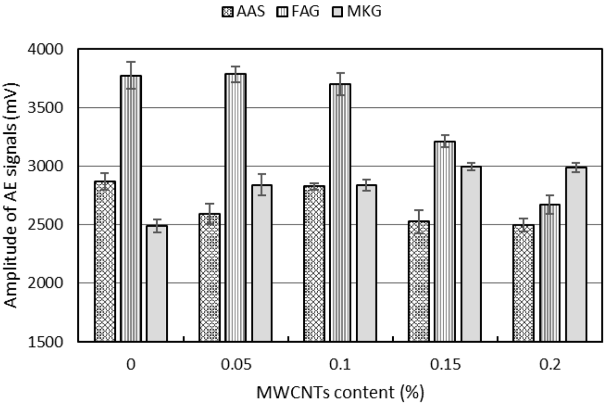

Fig. 3.6. Amplitude of AE signals of alkali-activated aluminosilicate composites with various amounts of MWCNTs detected during fracture test

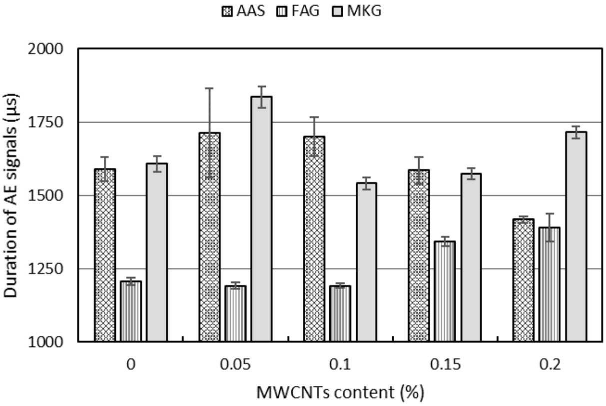

Fig. 3.7. Duration of AE signals of alkali-activated aluminosilicate composites with various amounts of MWCNTs detected during fracture test

The duration of an AE signal is the time difference between the crossing of the first and last threshold. As in case of amplitude, the duration of AE signals measured for FAG samples was completely different from those of AAS and MKG. FAG samples exhibited lower values which slightly increased with 0.15 and 0.20% MWCNTs. In case of AAS and MKG, the addition of carbon nanotubes at lower dosage increased the time of duration but with higher amounts of nanotubes it was reduced.

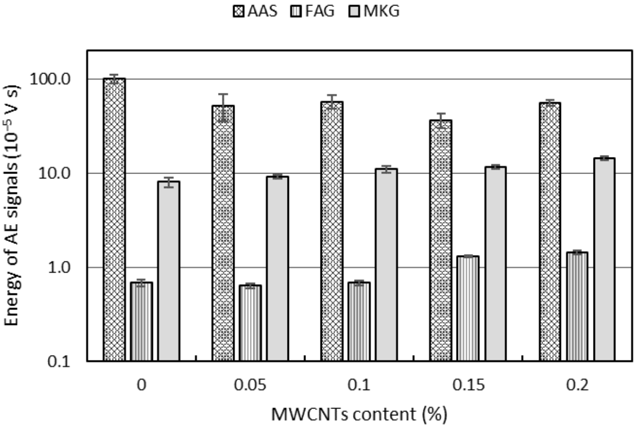

Fig. 3.8. Energy of AE signals of alkali-activated aluminosilicate composites with various amounts of MWCNTs detected during fracture test (in logarithmic scale)

The acoustic emission method was also used to monitor the hardening process of alkali-activated aluminosilicate mortars. In order to evaluate the formation of microcracks during hardening, we focused on the most commonly-used AE parameter, which is the number of signals overshooting a preset limit. ‘Number of overshoots’ refers to the number of pulses emitted by the circuitry measuring the signal voltage that exceed the threshold for a given time interval. The number of microcracks in the specimen can be inferred directly from such AE activity. Since the most important processes which are involved in the formation of hard structure occur at an early age, Figs. 3.9–3.11 show the cumulative number of AE signals over time during the first 6–10 days after mixing. Addition of MWCNTs to AAS material does not bring too much improvement in reduction of cracking during hardening process. In the first four days, the number of AE signals of composites with MWCNTs even exceeded the one achieved with the reference sample. However, in longer period some improvement can be observed because the curve for AAS has still increasing trend even after 7 days whereas with MWCNTs only few new signals were detected irrespective of MWCNTs amount.

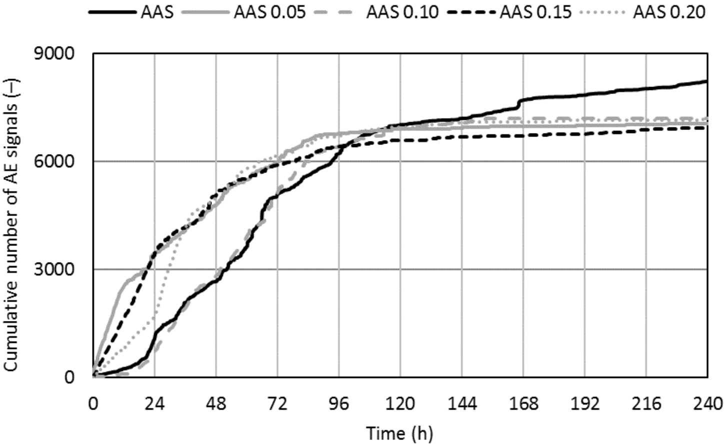

Fig. 3.9. Cumulative number of AE signals recorded during hardening of AAS mortars with MWCNTs

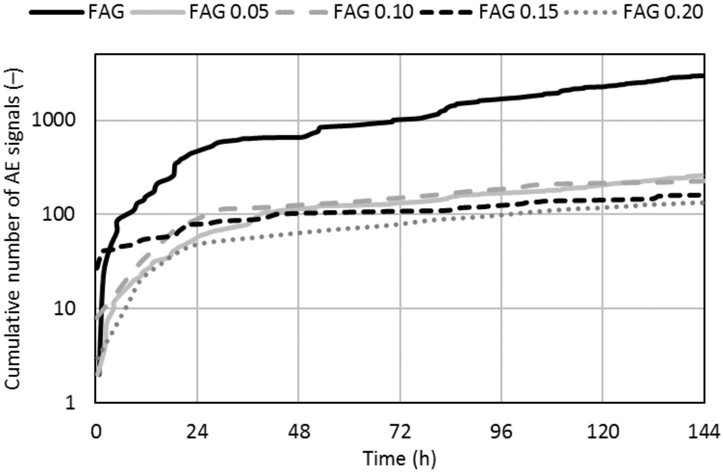

Fig. 3.10. Cumulative number of AE signals recorded during hardening of FAG mortars with MWCNTs (in logarithmic scale)

Remarkable improvement in cracking tendency was observed for FAG and MKG. The cracking tendency of FAG during hardening is much lower than for AAS and the application of MWCNTs helped reducing the number of AE signals by one order within the first three days (Fig. 3.10). However, similarly to AAS the amount of MWCNTs had negligible effect on the number of detected AE signals. Reference MKG material showed the highest number of AE signals within the first 6 days of the measurement but addition of MWCNTs had an essential influence on the reduction of signal (Fig. 3.11). It is also the only material for which the amount of MWCNTs had a significant effect on the number of signals. Application of just 0.15% MWCNTs was able to reduce the number of signals by three orders and in case of MKG 0.20 mixture the first event was detected at the age of 5 days.

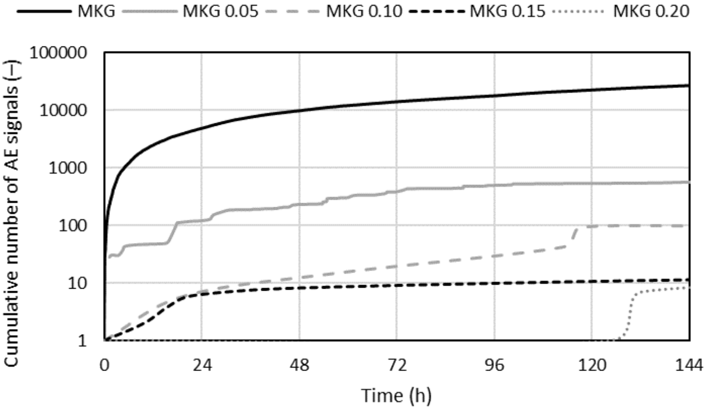

Fig. 3.11. Cumulative number of AE signals recorded during hardening of MKG mortars with MWCNTs (in logarithmic scale)

3.5 Conclusions

MWCNTs have been considered the most promising nanomaterial for enhancing the mechanical properties of building materials. In this research, MWCNTs were used for the improvement of mechanical fracture properties and the reduction in ability microcracks formation of three different types of alkali-activated aluminosilicate materials: alkali-activated slag, fly ash and metakaolin-based geopolymer. The tested materials exhibited totally diverse properties but the addition of MWCNTs had a positive effect on most of the determined parameters. Application of MWCNTs in AAS had the most positive effect on the improvement of elasticity modulus and fracture toughness whereas the best improvement in compressive strength was achieved with FAG. Finally, MWCNTs had the highest increase in fracture energy and showed the highest reduction of the microcracks formation during the process of hardening. We also noticed that the best improvement was achieved with 0.1 or 0.15% of MCNTs and higher dosage showed rather adverse effect. Therefore, the maximum amount of 0.15% of MWCNTs would be recommended to reach optimum properties.

Acknowledgements

This outcome has been achieved with the financial support of the Ministry of Education, Youth and Sports of the Czech Republic under the 'National Sustainability Programme I' (project No. LO1408 AdMaS UP).

References

Bakharev T., Resistance of geopolymer materials to acid attack. *Cem Concr Res*, 2005, vol. 35(4), pp. 658–670.

Belytschko T., Xiao S.P., Schatz G.C., Ruoff R., *Atomistic simulations of nanotube fracture*. *Phys Rev B*, 2002, vol. 65(23), pp. 235430–235437.

Davidovits J., *Mineral polymers and methods of making them*. US Patent 4,349,386, 1982.

Gluchovsky V.D., *Soil Silicates (Gruntosilikaty)*, Budivelnik Publisher, Kiev, 1959.

Grosse C.U., Ohtsu M., *Acoustic Emission Testing*, Springer-Verlag, Berlin 2008.

Iwanami M., Kamada T., Nagataki S., *Application of acoustic emission technique for crack monitoring in RC beams*. JCA Proc Cem Concr, 1997, vol. 51, pp. 192–197.

Karihaloo B.L., *Fracture Mechanics and Structural Concrete*, Longman Scientific & Technical, Harlow, 1995.

Keun-Hyeok Y., Jin-Kyu S., Keum-Il S., *Assessment of CO_2 reduction of alkali-activated concrete.* J Cleaner Prod, 2013, vol. 39, pp. 265–272.

Keun-Hyeok Y., Yeon-Back J., Myung-Sug C., Sung-Ho T., *Effect of supplementary cementitious materials on reduction of CO_2 emissions from concrete.* J Cleaner Prod, 2015,vol. 103, pp. 774–783.

Konsta-Gdoutos M.S., Metaxa Z.S., Shah S.P., *Multi-scale mechanical and racture characteristics and early-age strain capacity of high performance carbon nanotube/cement nanocomposites.* Cem Concr Comp, 2010-1, vol. 32(2), pp. 110–115.

Konsta-Gdoutos M.S., Metaxa Z.S., Shah S.P., *Highly dispersed carbon nanotube reinforced cement based materials.* Cem Concr Res, 2010-2, vol. 40(7), pp. 1052–1059.

Li Z., Xi Y., *Application of acoustic emission technique to detection of concrete cracking and rebar corrosion*. NDT-CE: Int. Symposium Non-Destructive Testing in Civil Engineering, Berlin 1995, pp. 613–620.

Lyon R.E., Balaguru P.N., Foden A., Davodovits J., Davidovits M., *Fire resistant aluminosilicate composites.* Fire Mater, 1997, vol. 21, pp. 67–73.

McLellan B.C., Williams R.P., Lay J., van Riessen A., Corder G.D., *Costs and carbon emissions for geopolymer pastes in comparison to ordinary Portland cement.* J Cleaner Prod, 2011, vol. 19(10), pp. 1080–1090.

RILEM Committee FMT 50, *Determination of the fracture energy of mortar and concrete by means of three-point bend test on notched beams*. Mater Struct, 1985, vol. 18(4), pp. 285–290.

Rovnaník P., Bayer P., Rovnaníková P., *Utilisation of alkali activated aluminosilicates as fire protecting materials.* Concrete for Fire Engineering, Proc. 7th Int. Congress – Concrete: Construct ion's Sustainable Option, IHS BRE Press, Brecknell, UK, 2008, pp. 273–282.

Rovnaník P., Bayer P., Rovnaníková P., *Characterization of alkali activated slag paste after exposure to high temperatures.* Constr Build Mater, 2013, vol. 47, pp. 1479–1487.

Rovnaníková P., Bayer P., *Corrosion resistance of alkali activated aluminosilicate materials.* Innovations and Developments in Concrete Materials and Construction, Thomas Telford, London 2002, pp. 373–381.

Sanchez F., Sobolev K., *Nanotechnology in concrete – A review*. Constr Build Mater, 2010, vol. 24(11), pp. 2060–2071.

Shi C., Krivenko P.V., Roy D., *Alkali-activated cements and concretes*, Taylor & Francis, Oxon 2006.

4. A correction of fatigue characteristics of concrete with respect to age of specimens

Hana Šimonová[1], Stanislav Seitl[1], Petr Frantík[1], Zbyněk Keršner[1]
[1] Brno University of Technology, Faculty of Civil Engineering, Brno, Czech Republic

4.1. Introduction

Many structures are often subjected to repetitive cyclic loads of high stress amplitude. Examples of such cyclic loads include automobile and train traffic, machine vibration and wind action. The phenomenon known as material fatigue, a process in which progressive and permanent internal damage occurs in materials subjected to repeated loading, is a serious problem also for concrete structures such as bridges, tunnels, airport/highway pavements, railway sleepers, etc. Concrete is a highly heterogeneous material and the processes occurring within its structure and leading to its degradation under cyclic loading are more complicated in comparison to those affecting metals (see Lee & Barr 2004). This is one reason why the understanding of fatigue failure in cementitious composites is still lacking in comparison to that of ferrous materials, even though concrete is a widely used construction material.

Fatigue tests of concrete materials and structures are expensive, and for this reason numerical modelling (Pryl et al. 2010) can represent a powerful approach for the prediction of the damage process and fatigue life of such materials under different service conditions. For the effective and correct use of a numerical (material) model it is often necessary to tune its parameters using data obtained during experiments. The correct evaluation of such data is becoming a prerequisite for the correct use of numerical models in practice.

Therefore, the topic of this chapter is the issue of determining fatigue characteristics of selected cement-based composites. In order to achieve relevant fatigue test evaluation which takes into account the age of the specimens, a correction procedure of the measured data based on static compressive strength measurements covering the time interval of the fatigue tests was suggested and verified. The procedure is applied to Wöhler curves obtained from cyclic three-point bending tests of beam specimens with a central edge notch.

4.2. Theoretical background

In practice, the structures are subjected to random fatigue loading. This process of loading is very difficult to model in the laboratory conditions, therefore there is an effort to simplify course of loading. The most frequent case is the replacement of the random loading by sinusoidal load, which were also used in experiments described later.

As in the case of static tests, different loading arrangements have been used in fatigue testing, including compression, tension and bending tests. The most common method of fatigue testing, by far, is via flexural tests (Lee & Barr 2004).

The fatigue loading is usually divided into two categories (RILEM 1984) i.e. low-cycle and high-cycle loading. Low-cycle loading involves the application of a few load cycles at high stress levels. On the other hand, high cyclic loading is characterized by a large number of cycles at lower stress levels. In this chapter, the attention will be paid on high-cycle fatigue.

Various approaches have been used to assess the fatigue life of structural members in recent years. The generally accepted approach in engineering practice is based on empirically derived *S–N* diagrams known as Wöhler curves (stress *S* vs. the number of cycles to failure *N*), see Figure 4.1. Fatigue tests are characterized by relatively large scattering of measured lifetime values at individual stress levels, therefore for an approximate determination of the Wöhler curve, several specimens have to be tested at each stress level. A minimum of 8–12 specimens of tested material is necessary to determine Wöhler curve. For a more accurate determination of its course, or for its statistical evaluation, 15–20 specimens is needed.

S–N test data are usually displayed in logarithmic co-ordinates, where its course is approximated by oblique and horizontal line. The oblique line approximates the set of completed tests. The horizontal line, which represents the fatigue limit, passes through a set of unfinished tests (run outs) in such a way that it corresponds to the highest stress level of only unfinished tests.

Unlike ferrous metals, concrete does not appear to have a fatigue limit. It has been reported that plain concrete subjected to repeated uniaxial tensile stresses exhibits no fatigue limit under 2×10^6 cycles (Satio & Imai 1983). Hence there is no known stress level below which the fatigue life of plain concrete will be infinite (Lee & Barr 2004).

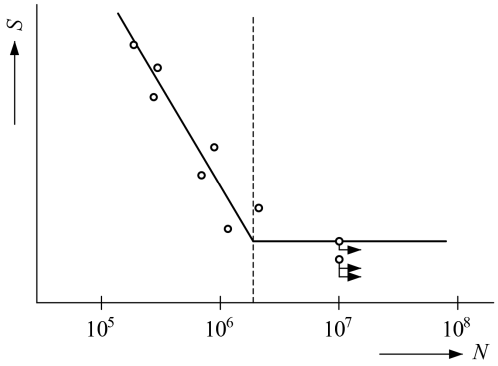

Fig. 4.1. Typical *S–N* (Wöhler) curve (according Věchet & Král 2007).

There are several mathematical descriptions of Wöhler curve:

Basquin function (Weibull 1961):

$$S = a \cdot N^b \tag{4.1}$$

Where:

S – applied stress,
N – number of cycles,
a – material parameter,
b – material parameter.

Kohout–Věchet model (Kohout &Věchet 2001):

$$\log \frac{\Delta\sigma}{\Delta\sigma_\infty} = b \cdot \log\left(\frac{N+B}{N+C}\right) \tag{4.2}$$

Where:

$\Delta\sigma$ – range of fatigue stress (variables),
$\Delta\sigma_\infty$ – permanent fatigue limit (limit value of fatigue stress for infinite number of cycles),
N – number of cycles (variable),
B – material parameter,
C – material parameter,
b – material parameter.

Another possibility is to use the statistical evaluation of dynamic tests, e. g. the Weibull non-linear regression model developed by Castillo (Castillo & Fernández-Canteli 2009):

$$S = exp\left(\frac{\left(log\left(\frac{1}{1-P}\right)\right)^{1/\beta}\cdot\delta+\lambda}{\log N-B}+C\right) \tag{4.3}$$

Where:

S – fatigue stress,

N – number of cycles (variable),

P – probability of failure,

B – model parameter, threshold value for N or the limit number of cycles,

C – model parameter, threshold value for S or the endurance limit,

β, δ – model parameter, shape and scale parameters of the Weibull distribution,

λ – model parameter, parameter fixing the position of the zero probability curve.

4.4. Materials and methods

An extensive laboratory experiment was conducted on a set of specimens of plain C30/37 and C45/55 class concrete. The specimens were used to determine the values of fundamental fracture characteristics and related fatigue parameters using static fracture and dynamic experiments. The partial result of this extensive experiments were published in following publication: Seitl et al. 2012, Šimonová et al. 2013, Šimonová et al. 2014.

As was already mentioned, the fatigue experiments lasted for a long time, which is problematic from the point of view of the ageing of the specimen material. In this case, the fatigue tests were performed between 28 and 160 days of specimen's age. Therefore, the correction procedure of the measured data based on static compressive strength measurements covering the time interval of the fatigue tests was suggested and verified (Šimonová 2013).

The procedure is applied to Wöhler curves (eq. 4.1) obtained from cyclic three-point bending tests of beam specimens with a central edge notch (see Figure 4.2). The nominal dimensions of the beams were 100×100×400 mm; span length 300 mm. The initial notches were made by a diamond bladed saw. Note that the depth of the notches was 10 mm (see Figure 4.3). The fatigue experiments were carried out in a computer-controlled servo hydraulic testing machine (INOVA–U2). The controlled values for temperature and relative humidity were 22±2 °C and 50%.

Fatigue testing was conducted under load control. The stress ratio $R = P_{\min}/P_{\max} = 0.1$, where $P_{\min}$ and $P_{\max}$ refer to the minimum and maximum load of a sinusoidal wave in each cycle. The load frequency used for all repeated-load tests was 10 Hz. The number of cycles before failure was recorded for each specimen. Concrete specimens were loaded in the range of high-cycle fatigue; therefore, the upper limit to the number of cycles to be applied was selected as 2 million cycles. The test finished when the failure of the specimen occurred or the upper limit of loading cycles was reached, whichever occurred first.

Fig. 4.2. Three-point bending fatigue test configuration.

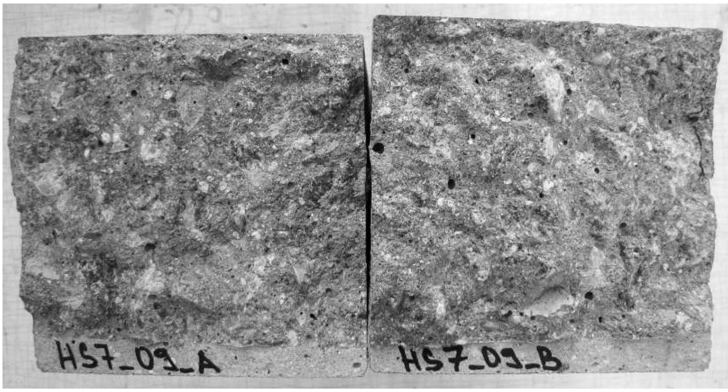

Fig. 4.3. Illustration of selected tested specimen after three-point bending fatigue test.

4.4. Advanced approximation of compressive strength values of concrete specimens

The suggested correction procedure allows more accurate determination of the fatigue parameters corresponding for the age of the specimens when the dynamic test was performed.

At first, analytical expressions were determined for regression curves as approximations of the selected mechanical fracture parameter values over time – compressive strength, modulus of elasticity, effective fracture toughness and specific fracture energy in the following way. In the first instance the relative values of individual parameters for all examined ages of specimens were obtained: the values of parameters obtained from measurement were divided by the appropriate mean average value for specimens at the age of 28 days. In the next step adaptation data for individual parameters were plotted in charts depending on the age of specimens. The analytical expressions for simple approximation (regression) curves were determined. Power, logarithmic and polynomial functions were used (EXCEL software). The coefficient of determination (R^2) was obtained for each type of regression curve.

From the analytical equations determined for the simple approximation curves of all mentioned mechanical fracture parameter values of plain C30/37 and C45/55 class concrete specimens follows that the closest approximations, based on the coefficient of determination value, were achieved for compressive cube strength values (Šimonová et al. 2011, 2013). For this reason, an advanced approximation curve was used for the compressive strength values, which more accurately describes the development of the compressive strength over time and not only in the interval in which dynamic tests were performed, as was in the case for simple approximation curves.

The cube specimens with edge lengths of 150 mm were used for determination of the compressive strength values. Because of the gradually increasing age of the concrete specimens during the dynamic tests, the specimens were tested at the age of 28, 98 (91 for C45/55 class concrete) and 159 days to cover whole interval of performing of dynamic tests. A summary of the compressive cube strength results for C30/37 and C45/55 class concrete is given in Table 4.1 and 4.2.

Table. 4.1. The compressive cube strength values [MPa] of C30/37 class concrete specimens at investigated ages.

Speci-men	f_{c28}				Speci-men	f_{c98}	Speci-men	f_{c159}
	Value	Mean value	Standard deviation	COV [%]		Value		Value
HS2_1	58.23	57.2	1.11	1.9	HS2_4	69.02	HS2_7	74.36
HS2_2	57.31				HS2_5	70.74	HS2_8	72.30
HS2_3	56.02				HS2_6	71.01	HS2_9	69.74

Table. 4.2. The compressive cube strength values [MPa] of C45/55 class concrete specimens at investigated ages.

Speci-men	f_{c28}				Speci-men	f_{c91}	Speci-men	f_{c159}
	Value	Mean value	Standard deviation	COV [%]		Value		Value
HS6_1	77.01	76.1	1.65	2.2	HS6_4	80.35	HS6_7	92.54
HS6_2	74.23				HS6_5	84.57	HS6_8	92.58
HS6_3	77.17				HS6_6	81.82	HS6_9	88.50

As in the case of simple approximation curves, the values of compressive strength obtained from measurement were divided by the appropriate mean value for specimens at the age of 28 days, thereby the relative values of compressive strength were determined. In the next step the relative values were then approximated by the function according to Abdel-Jawad 2006 in the modified form:

$$\frac{f_c(t)}{f_{c28}} = a \cdot \left(1 - e^{-b(t)^c}\right) \tag{4.4}$$

Where:

$f_c(t)$ – compressive strength at age t days,

f_{c28} – compressive strength at the age of 28 days,

a – $a = f_{c\infty}/f_{c28}$, coefficient represents an asymptote to an approximation curve expressed as the ratio between the theoretical compressive strength at the age $t = \infty$ and the determined mean value of compressive strength at the age of 28 days,

b, c – the exponential part of the equation with coefficients b and c expresses the degree of the time-dependent change in compressive strength at the interval $t = (0; \infty)$, which is generally dependent on the parameters of used concrete mixture and also on the environment conditions in which the specimens are stored.

The approximation was performed with the method of least squares using the genetic algorithms implemented in the open source Java package GA – Implementation of simple genetic algorithm (Frantík 2011).

Figure 4.4 shows the course of the approximation curve (4.4) for both classes of concrete with resulting coefficients *a*, *b* and *c*; The *x* symbol in the equation denotes the time in days, *y* the dimensionless relative value of the compressive cube strength, and R^2 is the dimensionless coefficient of determination.

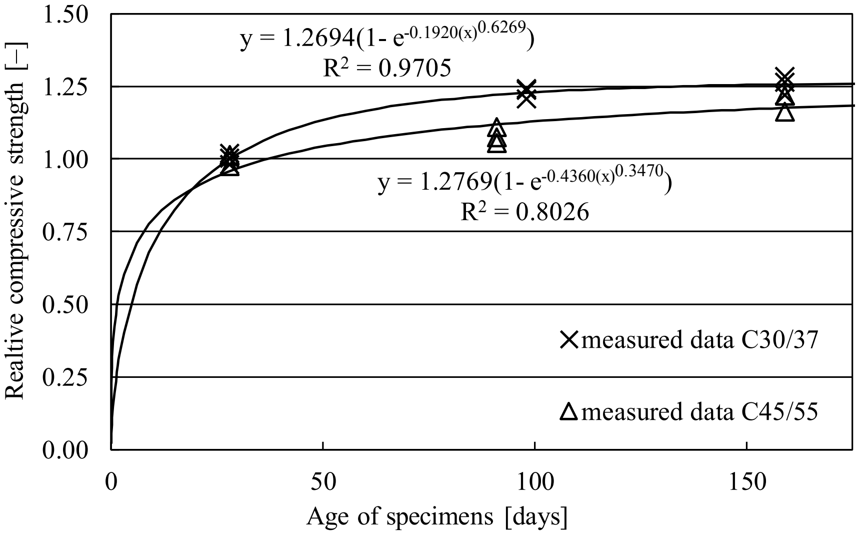

Fig. 4.4. Approximation curves for relative compressive cube strength.

4.5. Results of the fatigue fracture tests

The results of the fatigue tests under a varying maximum bending stress level are summarized in Figs. 4.5 and 4.6 for C30/37 and C45/55 class concrete, respectively, where the maximum bending stress (*S*) applied during the fatigue experiments is plotted against the logarithm of the number of cycles to failure (*N*).

In an ideal, theoretical case, all specimens at a certain stress level would fail after the same number of cycles. However, the fatigue behaviour of a heterogeneous material like concrete is far from being ideal, so the results are usually highly scattered. Accordingly, it is necessary to determine not only the analytical expression of the relevant *S–N* curve but also a measure of the scatter, such as the coefficient of determination R^2.

According to (4.1), the power function and the coefficient of determination for C30/37 class concrete are as follows:

$$S = 4.7256 \cdot N^{-0.0230} \text{ and } R^2 = 0.3806 \tag{4.5}$$

and for C45/55 class concrete:

$$S = 5.9227 \cdot N^{-0.0345} \text{ and } R^2 = 0.7289. \tag{4.6}$$

The coefficient of determination of *S–N* curve determined directly from the measured values is relatively low for both strength classes of concrete. In order to obtain correct values of fatigue characteristics corresponding to specimen age at which the fatigue tests were performed, the measured data were divided by the coefficients determined from the above introduced approximation curves of the compressive strength in time. The measured data was standardized to a specimen age of 28 days using this procedure.

For illustration, in Figs. 4.5 and 4.6, in addition to the measured data, the corrected data using the coefficients obtained from the advanced approximation curve of the relative compressive strength values (see Fig. 4.4) are also plotted, including the analytical expression of *S–N* curve and coefficient of determination. In case of C30/37 class concrete, this procedure led to a significant increase of the value of the dimensionless coefficient of determination from 0.38 to 0.70. In case of C45/55 class concrete an increase of the coefficient of determination was also achieved, although not in such extent, from 0.73 to 0.88. The obtained results can be considered as evidence of the efficacy of the described correction procedure.

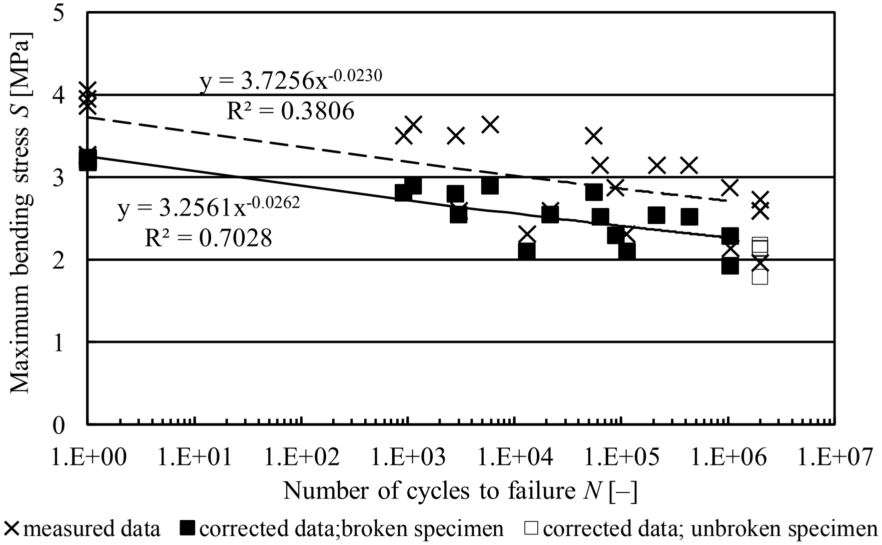

Fig. 4.5. *S–N* curves from the C30/37 class concrete.

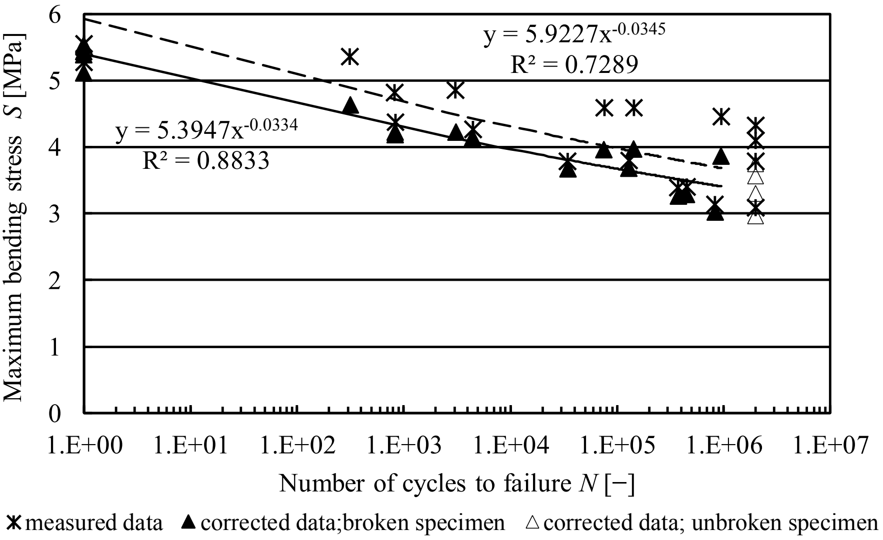

Fig. 4.6. *S–N* curves from the C45/55 class concrete.

4.6. Conclusions

A rather complex procedure of correction of the values of the basic fatigue parameters – Wöhler curves – of C30/37 class concrete specimens with initial central edge notch tested in three-point bending cyclic fracture tests was introduced in this chapter. The correction procedure is based on approximation of static compressive strength measured data covering the time interval of the fatigue tests. The experiment was repeated with the same extent at C45/55 strength class concrete specimens. It can be stated that correction for both sets of concrete specimens led to an increase in the coefficient of determination of Wöhler curve, which can be considered as proof of its effectiveness. The introduced correction procedure was used also for another sets of concrete specimens with an alkali-activated based binder (see Seitl et al. 2014, 2016) and also in this case the increase of coefficient of determination of Wöhler curve was achieved.

Acknowledgment

This paper has been worked out under the “National Sustainability Programme I” project “AdMaS UP – Advanced Materials, Structures and Technologies” (No. LO1408) supported by the Ministry of Education, Youth and Sports of the Czech Republic.

References

Abdel-Jawad Y.A., *Estimating concrete strength using a modified maturity model,* Proceedings of Institution of Civil Engineers – Construction Materials, 2006, vol. 159, iss. CMI.

Castillo E., Fernández-Canteli A., *A Unified Statistical Methodology for Modeling Fatigue Damage*, Springer, 2009.

Frantík P., *Java package GA – Implementation of simple genetic algorithm*, GNU GPL licence, 2011, [online], http://www.kitnarf.cz/java.

Kohout J., Věchet S., *A new function for fatigue curve characterization and its multiple merits*, International Journal of Fatigue, 2001, vol. 23, pp. 175–183.

Lee M.K., Barr Big, *An overview of the fatigue behavior of plain and fibre reinforced concrete*, Cement & Concrete Composites, 2004, vol. 26, pp. 299–305.

Pryl D., Červenka J., Pukl R., *Material model for finite element modeling of fatigue crack growth in concrete*, Procedia engineering, 2010, vol. 2, issue 1, pp. 203–212.

RILEM Committee 36-RD 1984, *Long term random dynamic loading of concrete structures*, Materials and Structures, vol. 17, issue97, pp. 1–28.

Satio M., Imai S., *Direct tensile fatigue of concrete by the use of friction grips, ACI J* , 1983, vol. 80, pp. 431–438.

Seitl S., Šimonová H., Keršner Z., Fernández-Cateli A., *Evaluation of concrete fatigue measurement using standard and nonlinear regression model*, Applied Mechanics and Materials, 2012, vol. 121–126, pp. 2726–2729.

Seitl S., Bílek V. Keršner Z., *Comparison of Fatigue parameters of Alkali-Activated and ordinary portland cement based concretes*, IJRET: International Journal of Research in Engineering and Technology, 2014, vol. 3(13), pp. 203–208.

Seitl S., Bílek V., Šimonová H., Keršner Z., *Mechanical and fatigue parameters of two types of alkali-activated concrete*, Key Engineering Materials, 2016, vol. 665, pp. 129–132.

Šimonová H., Keršner Z., Seitl S., *Correction of fatigue parameter values of concrete using approximation of mechanical-fracture parameter values in time.* Proc. of Int. Conf. on ENGINEERING MECHANICS 2011, Svratka 2011, May Praha: Institute of Thermomechanics, Academy of Sciences of the Czech Republic, v.v.i., pp. 9–12.

Šimonová H., *Determination of Fatigue Characteristics of Concrete Using Fracture-Mechanics Parameteres*, Brno, PhD. Thesis (in Czech), 2013.

Šimonová H., Havlíková I., Keršner Z., Seitl S., S*tatistical evalution of fatigue tests of plain C30/37 and C45/55 class concrete specimens*, Proceedings of the 8th International Conference on Fracture Mechanics of Concrete and Concrete Structures FraMCoS, 2013, pp. 862–867.

Šimonová H., Kucharczyková B., Havlíková I., Seitl S., Keršner Z., *Complex Evaluation of Fatigue Tests Results of Plain C30/37 and C45/55 Class Concrete Specimens*, Key Engineering Materials, 2014, vols. 592–593, pp. 801–804.

Věchet S. Král P. *Únava materiálu: Únava materiálu úvod.* In NoM I – 6, Únava materiálu. [s.l.] : [s.n.], 2007, (in Czech). pp. 1–9.

Weibull W., *Fatigue testing and analysis of results*, Pergamon press, 1961.

5. Selected applications of acoustic methods in building materials monitoring

Libor Topolář[1], Luboš Pazdera[2], Michaela Hoduláková[3], Karel Mikulášek[4]

[1,2,3,4] Brno University of Technology, Faculty of Civil Engineering, Brno, Czech Republic,

5.1. Introduction

Non-destructive testing (NDT) is a process of inspecting, testing, and evaluating materials, components or assemblies for discontinuities, or differences in characteristics without destroying the serviceability of a system or its part. In other words, after an inspection or test is completed the part inspected can still be used.

The acoustic NDT methods are concerned with the state-of-the-art situation in the field of experimental studies of the physical properties of engineering materials. The evaluation of these properties has been a longstanding urgent problem in civil engineering and its importance is constantly increasing with the advent of novel types of engineering materials.

NDT methods are advantageous with its capacity to detect cracks and pores in building materials. In addition, they produce good results in the testing of such materials as metals and composites. The following are their major advantages: acceptable accuracy, safety in experiments, low cost, and the easy transportability of equipment to the place where the actual measurements are performed.

However, applying acoustic NDT to building composites poses certain difficulties due to their complex internal structure. An engineering material can be regarded as a composite of composites, it is inhomogeneous at the micro and macro levels, and can be characterized by such opposite properties as brittleness and softness, elasticity and inelasticity, properties that are characteristic of a liquid (fluidity) and a solid (shear strength), the presence of cracks, cavities, and pores that are filled with air or liquid (or with both air and liquid) (Brigante 2013).

Non-destructive acoustic analysis methods, the Impact Echo (IE) method as a traditional and the Acoustic Emission (AE) method as the non-traditional method for civil engineering, were used in several experiments.

5.2. Acoustic Emission Method

The AE method has been regarded as the prime candidate for structural health and damage monitoring in loaded structures for many years. It offers the user a number of inherent advantages; mainly, it is able to continuously monitor in situ and to examine the whole volume of a structure simultaneously with a limited number of sensors (Iturrioz 2014). Acoustic emission refers to the noise emitted by material and structures when subjected to stress. The stress types can be mechanical, thermal, or chemical. The emission is caused by rapid release of energy within a material due to events such as crack formation, and the subsequent extension occurring under an applied stress, generating transient elastic waves, which can be detected by piezoelectric sensors (Grosse 2008, Ohtsu 1996).

The main AE parameters (Surgeon 1999):

- Count - the number of times an AE signal crosses the threshold
- Duration - difference between the first and the last time an AE signal crosses the threshold
- Amplitude - maximum/minimum voltage excursion of an AE signal within duration

AE activity is attributed to the rapid release of energy in a material with the energy content of the AE signal being related to this energy release. The true energy is directly proportional to the area under the AE waveform (Sagar 2009):

$$AE\ energy_i = \int_{t_0}^{t_1} V_i(t)^2 dt \tag{5.1}$$

where:

i – the recorded voltage transient $V(t)$ of a channel

t_0 – the starting time of the voltage transient record

t_1 – the ending time of the voltage transient record

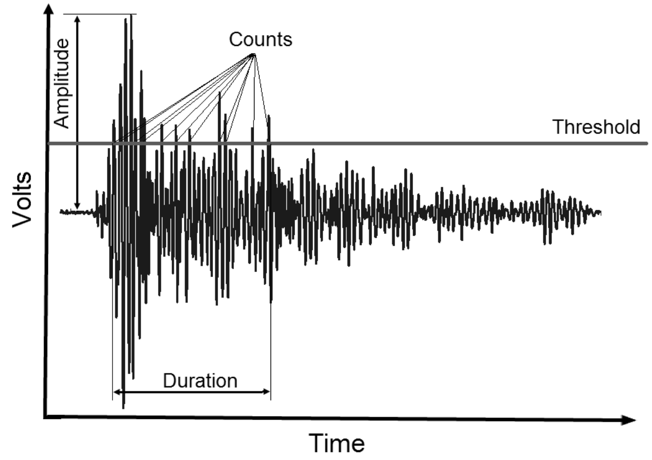

Fig. 5.1. Typical AE event

Various types of cracks generate different types of AE signals with varying parameters, such as frequencies and amplitudes. These differences can be related to the degree of damage to the structure or material composition. The smaller microcracks generate many small amplitude events while the bigger ones generate fewer events but with higher amplitudes. When the cracks are opening, as most of the energy has already been released, many events with small amplitudes are created. Furthermore, tensile cracks spawn large amplitude events while shear cracks create smaller amplitude signals (Iwanami 1997, Li 1995).

Acoustic emission equipment

To detect AE signals in experiments, a DAKEL XEDO measurement system was used consisting of AE sensors (MDK13 with inbuilt magnetic holder, IDK 09 and MTPA-15 with inbuilt preamplifier approx. 35 dB), amplifier (AS3K with 35 dB gain), and filter (100-800 kHz). The total amplification of the preamplifier and the main amplifier was set at 55 to 75 dB. The measurement system records such parameters as count, hit, event, maximum amplitude, rise time, duration, root mean square (RMS), and voltage and arrival-time difference. The waveform parameters are illustrated in Figure 5.1. Elimination of the noise is ensured by setting the threshold level at 200 - 400 mV according to the configuration of a particular experiment, or by filtering in a post-analysis of the data.

5.3. Impact-echo Method

As a non-destructive acoustic technique based on the idea that the mechanical characteristics of a specimen affect its spectral properties, the IE method analyzes the elastic impulse-induced mechanical wave (Liang 2001). A short-time mechanical impulse induced by a steel spherical body gives rise to a low-frequency pressure wave (Fig. 5.2). Thus, the generated wave propagates through the specimen's structure being rebounded by defects located in the specimen's bulk or on its surface. The time difference between the emitted and the rebounded waves is recorded by a sensor, which shows the signal waveform. In theory, the impact resembles a delta-function containing all possible frequencies. During wave propagation, each frequency component is affected by the geometry of the specimen, the material properties, defects, non-homogeneities, cracks or any other structural characteristics (Birgham 1988). The frequency spectrum of the gathered signal is calculated using Fast Fourier Transform (especially its dominant frequencies) giving an account of the condition of the specimen.

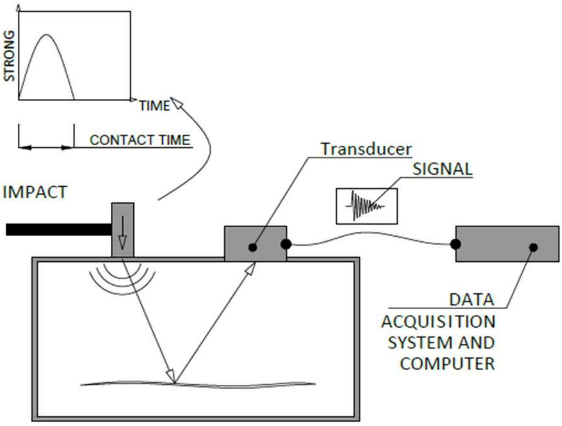

Fig. 5.2. Principle of the Impact Echo method

Impact-echo measurement

In order to generate the signal, a hammer of 12 g mass, originally suspended from a hanger, was released to fall down on the specimen from a height of 4 cm. The impulse was reflected by the surface but also by microcracks and defects of the specimen under investigation. The response was picked up by a MIDI type piezoelectric sensor. Its output voltage was fed into a TiePie engineering Handyscope HS3, which is a two-channel, digital, 16 bits oscilloscope. The piezoelectric sensor was placed at the end of the beam at the centre of the transverse side and the hammer hit was carried out on the opposite side in the direction of the longitudinal axis. The sensor was attached to the surface of the specimen by beeswax. Subsequently, a special smoothing algorithm was used to determine the dominant frequencies for each of the output signals.

5.4. Achieved results and discussion

5.4.1. Measurement during setting and hardening using waveguides

We studied a cement-based beam sized 360 mm x 50 mm x 50 mm. For the beam, fine-grained concrete mixture was used composed of 400 kg cement CEM II/B – S 32.5 and 1400 kg sand Želešice with the fraction of aggregate being 0 mm – 4 mm and 225 l water. The fine-grained concrete was modified on a vibration table. After casting, the fine-grained concrete was kept in the forms at room temperature for 24 hours before demoulding. Two specimens were measured simultaneously for each method. One specimen was sealed by PE foil to avoiding water exchange with the environment and the specimen was cured without any water exchange prevention. The second specimen was left free in the air without treatment. Four AE sensors were placed on the surface of both specimens (see Fig. 5.5. - left). Two sensors were placed on the first specimen and another two on the second one. For the IE method, the piezoelectric sensor was placed at one beam end in the longitudinal centre line of the beam and the hammer hit the opposite end of the beam in the direction of the centre line of the beam (see Fig. 5.3 - right).

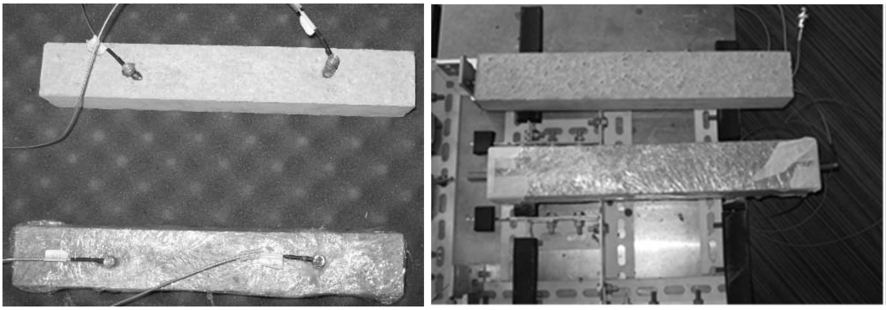

Fig. 5.3. Photography of Acoustic Emission (left) and Impact-echo (right) measurement

The measurement began after demoulding, that is, 24 hours later by preparing the fine-grained concrete mixture. The diagram in Fig. 5.4 shows how the cumulative count N_C depends on time t. The foil-covered specimen (solid line) had a significantly lower AE count than the specimen without cover (dashed line) during the measurement period (10 days). The higher AE activity is likely to be caused by a higher number of microcracks in the specimen (Pazdera 2010).

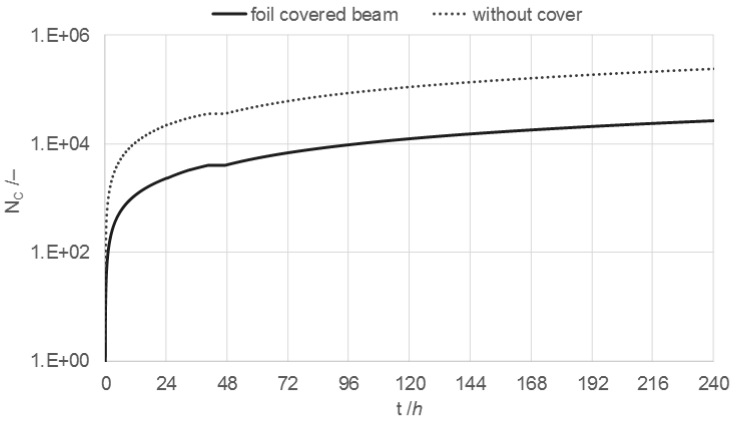

Fig. 5.4. Time-dependent cumulative counts of acoustic emission (N_C)

The graphs (Fig. 5.5 and Fig. 5.6) show the frequency spectrum. For two specimens (foil covered beam and beam without cover), each graph is shown at a different time from the moment of mixing.

Fig. 5.5 shows the frequency spectrum for specimens at the beginning the fine-grained concrete (that is, 24 hours after mixing). In the frequency spectrum, the foil covered specimen (solid line) has the frequency (marked A) at position 990 Hz. This frequency A is not visible in the specimen without cover (dashed line). During the hardening, the frequency A moved to the value of 1430 Hz (after 240 hours of mixing) as shown in Fig. 5.6. Another significant frequency (labelled B) only occurs during the monitoring of the foil cover specimen again. 24 hours after mixing (Fig. 5.5) it had a value of 2870 Hz and, after 240 hours of mixing (Fig. 5.6), this increased to 3230 Hz.

The frequency (marked C - foil cover specimen; C' - without cover specimen) is present in both specimens. The foil-cover specimen's frequency C within 24 hours after mixing was 3630 Hz and, at the end of monitoring, 5160 Hz. The corresponding frequency C' of the specimen without cover after 24 hours from mixing was 3390 Hz while, at the end of monitoring, its value was 4510 Hz. From this frequency, we can find the frequencies of higher orders which might indicate that it is a self-resonant frequency of the specimen.

At the end of the monitoring (that is, after 240 hours from mixing) 3 significant frequencies (marked X ', Y', Z ') were found in the specimen without cover, see Fig. 5.6. These frequencies were probably formed due to the non-linearities in the structure of the element. These non-linearities are due to the lack of water during the hydration of cement and, probably, cause damage to the structure of the specimen.

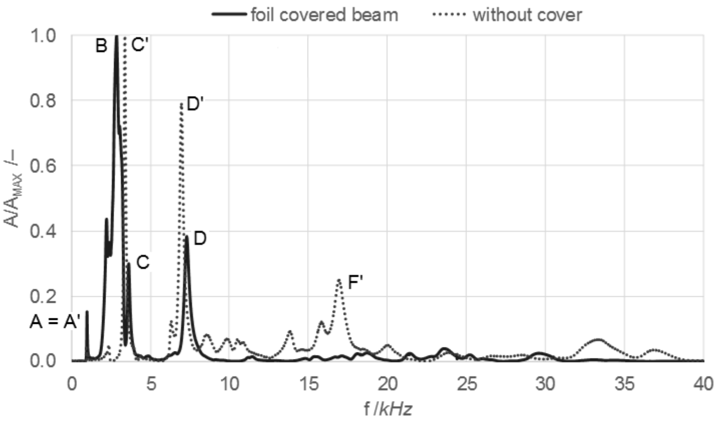

Fig. 5.5. Impact Echo – frequency spectrum 24 hours after the mixing

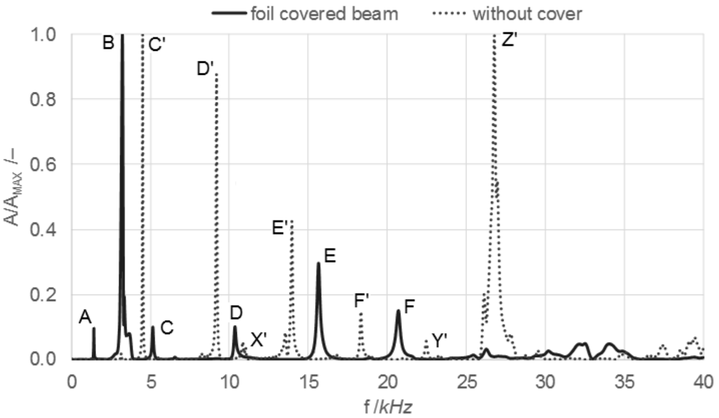

Fig. 5.6. Impact Echo – frequency spectrum 240 hours after the mixing

The diagram in Fig. 5.7 shows the dependence of weight loss m on time t. The foil-covered specimen (solid line) has a significantly lower weight loss than the one without cover (dashed line) during the measurement period (10 days). The foil-covered specimen used all the water added to the batch during mixing. The weight loss of the specimen without cover is caused by both the hydration and water evaporation.

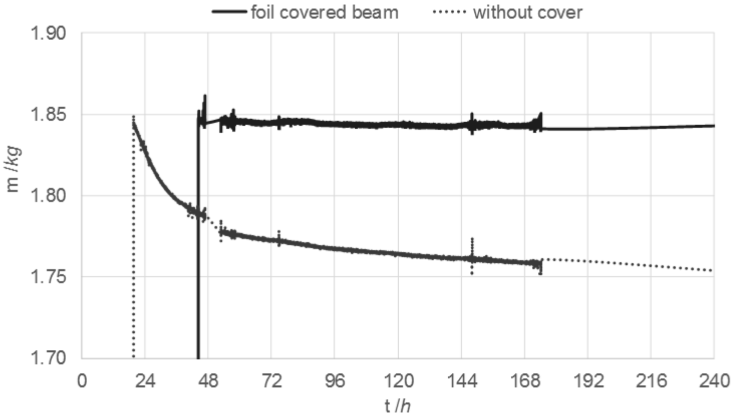

Fig. 5.7. The time (t)-dependent weight loss of the specimen (m).

5.4.2. The pilot measurement during the six freeze-thawing cycles

Two specimens sized 100 x 100 x 400 mm were measured simultaneously. Four AE sensors were placed on the surface of both specimens (see Fig. 5.8). Two sensors were placed on the first specimen and another two on the second one. Each sensor was kept in place by a specifically made holder for the contact between the sensor and the specimen surface to be as good as possible.

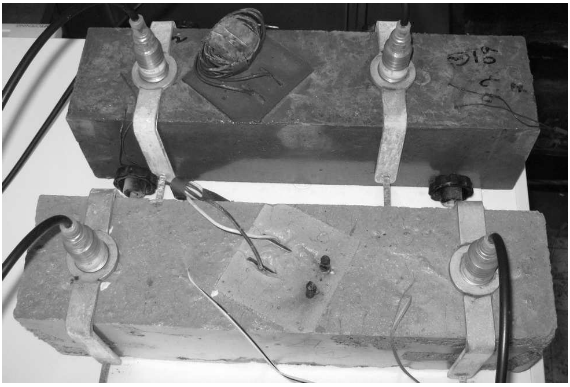

Fig. 5.8. Location of acoustic emission and temperature sensors and electrodes for monitoring electrical properties

The sensors are designed to be resistant to an aggressive salt solution and can be applied in temperatures from -30 to +30 °C without any problems (Zhang 2006). Both specimens were put into a freezer until the temperature fell down to -25 °C. Then, they were put into water with a temperature of 15 ~ 20 °C. As this was a pilot measurement, everything was done manually. For this reason, some of the longer cycles are shorter. To compare both specimens and test methods for this type of building material failure, the experiment was sufficient.

Temperatures T (°C) inside the specimens were measured by negative thermal resistors during the whole experiment being computed using the equation:

$$T = 0.03 \cdot \left(\frac{R_x}{R_{25}}\right)^4 - 0.83 \cdot \left(\frac{R_x}{R_{25}}\right)^3 + 7.49 \cdot \left(\frac{R_x}{R_{25}}\right)^2 - 33.92 \cdot \left(\frac{R_x}{R_{25}}\right) + 51.69, \quad (5.2)$$

where R_x is the measured resistance (Ω), R_{25} is a reference resistance at 25 °C (Ω). These sensors were embedded in concrete specimens.

The graphs in Fig. 5.9 and Fig. 5.10 show cumulative counts (N_C) and temperatures (T) over time (t). For the specimen with worse frost resistance, a significantly higher AE count was observed than for the one with better frost resistance during the measurement period (6 freeze-thaw cycles). It can be assumed that the greater numbers of counts are caused by higher numbers of microcracks in the specimen. Higher AE activity is observed as he temperature increases. As the temperature decreases the AE, the activity does not usually change very much. AE activities, i.e., micro-changes in the structure, are indicated within one and a half day from the start of temperature increase (Pazdera 2014). Thus, when specimens were pulled out from the freezer, micro-changes had been in progress for two days. When specimens were put back in the freezer for another two days, the AE activities continued (see Figs. 5.9 and 5.10).

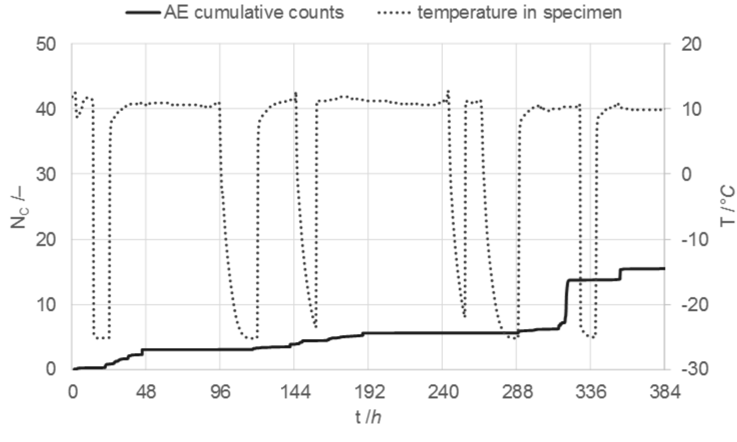

Fig. 5.9. The acoustic emission activity (N_C – left axis) and temperature (T - right axis) over time (t) - (specimen with better frost resistance)

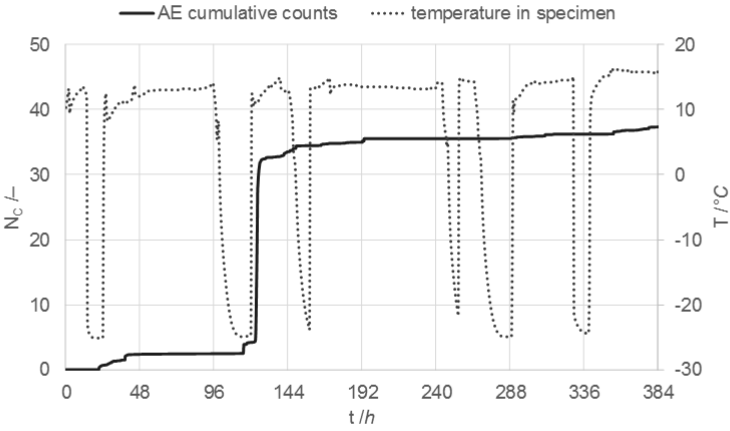

Fig. 5.10. Acoustic emission activity (N_C – left axis) and temperature (T - right axis) over time (t) - (specimen with worse frost resistance)

Both mixtures were monitored by the IE method, too. The specimen with better frost resistance (Fig. 5.11) shows two natural frequencies, f_1 = 2200 Hz and f_2 = 5500 Hz. Their positions after the application of six freezing cycles were similar. However, the frequency spectra of the specimen with worse frost resistance (Fig. 5.12) are different after six freezing cycles, which indicates a worse frost resistance of this specimen. The spectrum contained two frequencies, f_1 = 850 Hz and f_2 = 1990 Hz. After the degradation, these two frequencies were spread into seven frequency components. This is due to many small defects in the monitored structure.

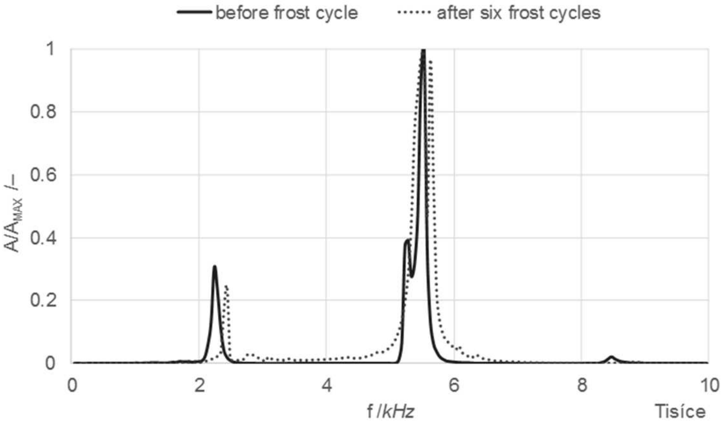

Fig. 5.11. Relative frequency spectrum of the concrete specimen with better frost resistance

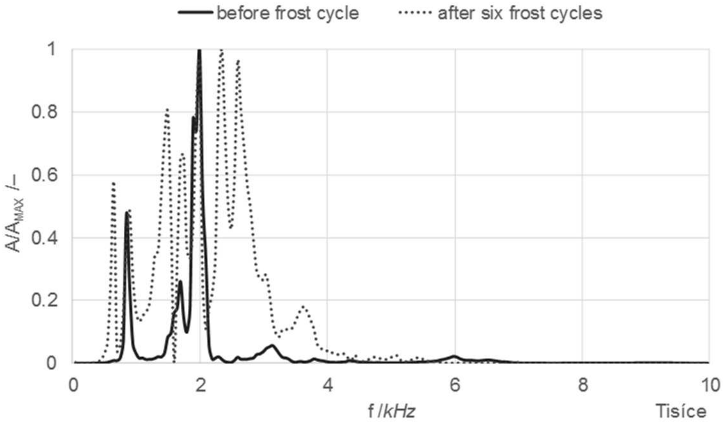

Fig. 5.12. Relative frequency spectrum of concrete specimen with worse frost resistance

5.4.5. Measurement of heat degradation specimens

For the experimental part, concrete specimens with dimensions of 100 x 100 x 400 mm were prepared. Seven sets of test specimens were manufactured. Each set was labelled with an ID number which corresponds to the temperature conditions maintained in the laboratory furnace during its heating. Specimens labelled 20 represent concrete specimens which dried freely in laboratory conditions with a temperature of (21±1) °C and were not further heated. The specimens (except for specimens labelled 20) were immersed in a water bath for 28 days. Then, they were dried first in the laboratory conditions and then in a ceramic furnace at temperature 110 °C for another 48 hours. The concrete specimens were heated in a programmable laboratory furnace Rhode KE 130B at the heating rate of 5 °C/min. Selected temperatures T= 200 °C, 400 °C, 600 °C, 800 °C, 1000 °C and 1200 °C were maintained for 60 minutes. Three-point bending (3PB) tests were performed after the specimens were exposed to prescribed thermal stress levels. Ten specimens from each set were tested. Four AE sensors were attached to the surface by beeswax – see in Fig. 5.15. The loading tests were carried out using a Heckert FPZ 100/1 testing machine at a laboratory in the Institute of Building Testing, Faculty of Civil Engineering, Brno University of Technology. Beam specimens with initial central edge notches were loaded under a 3PB test using the displacement-controlled method which is more suitable for monitoring the behaviour of specimens after crack initiation and during its propagation. The initial notch was made by a diamond blade sawed before testing. The depth of the notches was about 33 mm for all specimens (Topolář 2015).

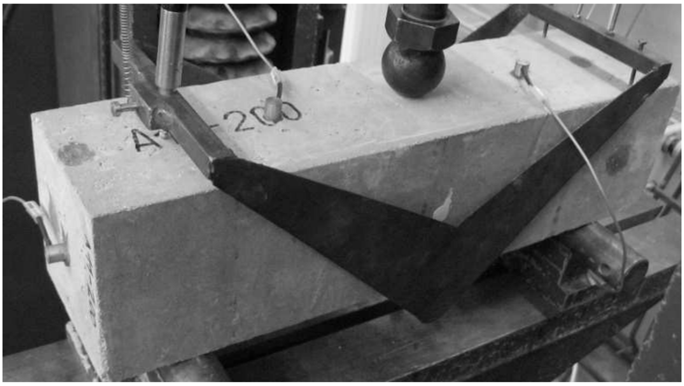

Fig. 5.15. The location of acoustic emission sensors on specimen during the three-point bending test

To describe AE signals which are formed during the three-point bending test in the specimens, the focus was on the number of events and AE energy. Fig. 5.14 and Fig. 5.15 present the dependence of the number of AE events on the thermal stress level. The waves which emerge and propagate within the specimen during the three-point bending test can affect the material element oscillations. The exposure to elevated temperatures causes a change of structure, leading to the change in the number of AE events. These changes can be accounted for by the process of concrete decomposition during the thermal stress application. Heating the concrete up to 100 °C results in the dehydration (loss of the chemically bound water) with the formation of Calcium-Silicate-Hydrate (C-S-H) and calcium hydroxide $Ca(OH)_2$ – Portlandite. As the temperature is further raised up to 200 °C, a dehydration of cementing compound begins resulting in the release of physically bound water along with the concurrent decomposition of hydrate. The first stage of decomposition of C-S-H and decomposition of gypsum $CaSO_4.2H_2O$ culminates between 150 °C and 170 °C. However, the number of AE events is lower than in the case of specimen labelled 20 (unheated), which indicates a lower quantity of new formed microcracks. At a temperature above 200 °C, physically bound water is released. Between 250 - 300 °C, the hydrated cement phases are decomposed. Further increase of temperature above 300 °C results in the decomposition of Portlandite [$Ca(OH)_2 \rightarrow CaO + H_2O$] and significant formation of microcracks. The formation of microcracks and Portlandite decomposition results in a significant increase in the amount of microcracks which arises before the ultimate tensile capacity of the test specimens during three-point bending test is reached. The decrease of the number of AE events is caused by quartz phase transition (in the silicate aggregate) from triclinic system to the hexagonal system (β at α 573 °C) after heating up to 600 °C (see Fig. 5.15). This resulted, together with the influence of the difference in the thermal expansion disruption bonds between aggregate and cementing compound, in the creation of a small number of microcracks during the 3PB test. When the heating temperature is increased to 800 °C, the second phase of C-S-H and also of calcium carbonate [$CaCO_3 \rightarrow CaO + CO_2$] decomposition begins. This decomposition leads to a decrease in the number and size of arising microcracks (see Fig. 5.15). In conjunction with the total decomposition of the cementing compound at the temperature of 1000 °C, the lowest value of the number of AE events (the smallest number of arising microcracks) was recorded for the specimens labelled 1000. For the specimens exposed to a thermal stress at a temperature of 1200 °C, a larger number and size of the microcracks formed were recorded again. This is due to a structural change, accompanied by the creation of new crystal phases [Wollastonite β ($CaO.SiO_2$)], which takes place in the specimen's structure at temperatures of above 1000 °C (Bian 2016, Gao 2016).

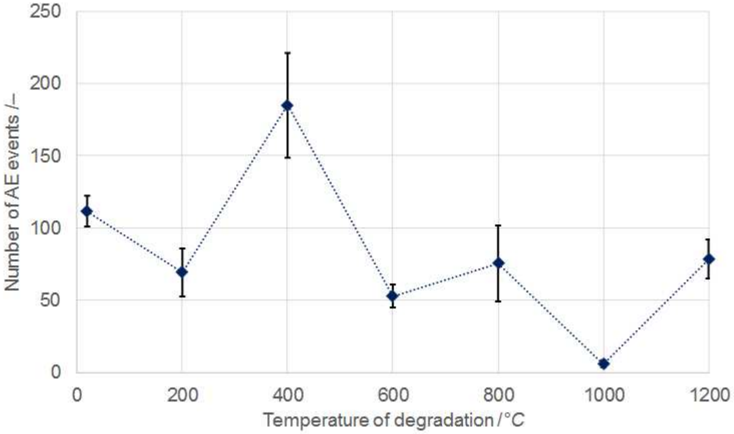

Fig. 5.14. The dependence of the number of AE events on thermal stress level (record to ultimate tensile capacity)

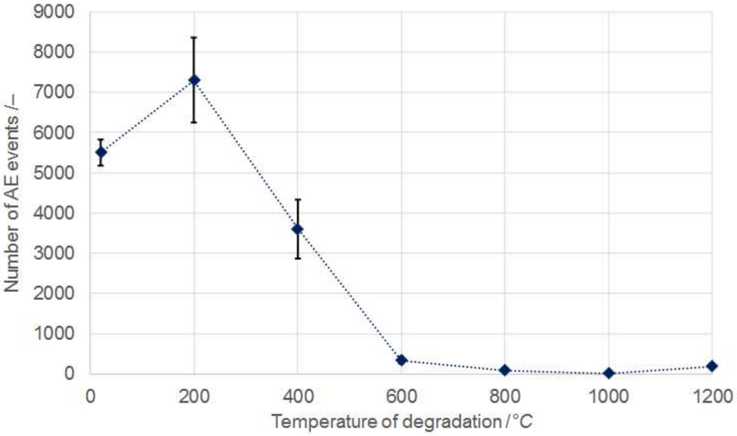

Fig. 5.15. The dependence of the number of AE events on thermal stress level (complete record of the measurement)

The values of AE energy (Fig. 5.16) are in correlation with the toughness of the particular set of concrete specimens. The highest value of AE energy was recorded for specimens exposed to the temperature of 200 °C which may indicate that also the toughness of the specimen is high (in comparison with unheated specimens labelled 20). This implies that structural changes prevent the crack growth because more energy is needed for fracture. Generally speaking, the rising heating temperature above 200 °C causes a decrease in the quantity of AE energy released during the three-point bending test that indicates the raising brittleness of the material. This behaviour of concrete is changed with a temperature of above 1000 °C when the Wollastonite is created and an increase in concrete toughness can be observed.

Figure 5.17 shows the evolution of the dominant frequency of longitudinal temperature-dependent waves. The longitudinal waves that propagate within the specimen can affect the mortar element oscillations. The exposure of a specimen to elevated temperatures causes a decrease of the dominant frequency, which leads to the conclusion that the material's elastic modulus for each composition also decreases. In the course of the degradation, the predominant frequencies are shifting towards the lower frequency range (Štefková 2016).

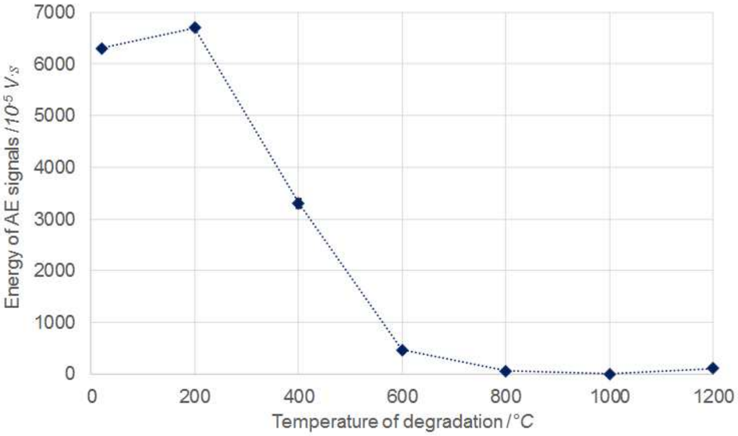

Fig. 5.16. The dependence of energy of AE signals on the degradation thermal stress level (complete record of the measurement)

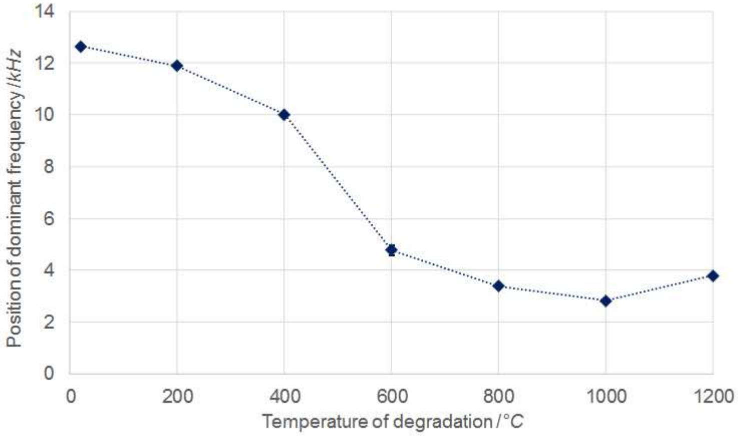

Fig. 5.17. The dominant frequency of longitudinal waves depending on the degradation thermal stress level

5.5 Conclusions

A combination of AE and IE methods is a powerful tool for detecting microcracks in building materials. While the AE method detects active (newly created) microcracks, the IE method detects the passive (already generated) ones. It can be assumed that higher numbers of microcracks cause a greater number of AE events and more numerous dominant frequencies in the frequency spectrum of the IE method.

In selected cases of measuring the setting of cured and uncured concrete specimens, the cyclic loading by freezing, and the thermally degraded specimens, the capacities are declared of both selected non-destructive testing methods, the one of acoustic emission as well as that of impact echo. Particularly the AE method makes it possible to describe the processes going on in the structure of an observed specimen on a continual basis.

Acknowledgement

This outcome has been achieved with the financial support of the project No. LO1408 "AdMaS UP - Advanced Materials, Structures and Technologies", supported by Ministry of Education, Youth and Sports under the „National Sustainability Programme I".

References

Bian H., Hannawi K., Takarli M., Molez L., Prince W., *Effects of thermal damage on physical properties and cracking behavior of ultrahigh-performance fiber-reinforced concrete*, Journal of Materials Science, 2016, vol. 51, issue 22, pp. 10066-10076.

Birgham E., *Fast Fourier Transform and Its Applications*, Prentice Hall, New Jersey, USA 1988.

Brigante M., Sumbatyan M.A., *Acoustic methods for the nondestructive testing of concrete: A review of foreign publications in the experimental field*, Russian Journal of Nondestructive Testing, 2013, vol. 49, issue 2, pp. 100-111.

Gao X., Zhang A., Li S., Sun B., Zhang L., *The resistance to high temperature of magnesia phosphate cement paste containing wollastonite*, Materials and Structures, 2016, vol. 49, issue 8, pp. 3423-3434.

Grosse C., Ohtsu M., *Acoustic Emission Testing*, Springer, Berlin, Germany 2008,.

Ohtsu M., *The history and development of acoustic emission in concrete engineering*, Magazine of Concrete Research, 1996, vol. 48, issue 177, pp. 321–330.

Iturrioz I., Lacidogna G., Carpinteri A., Lacidogna A., *Carpinteri: Acoustic emission detection in concrete specimens: Experimental analysis and lattice model simulations*, International Journal of Damage Mechanics, 2014, vol. 23, issue 3, pp. 327-358. DOI: 10.1177/1056789513494232

Iwanami M., Kamada T., Nagataki S., *Application of acoustic emission technique for crack monitoring in RC beams,* JCA Proc. Cement and Concrete, 1997, vol. 51, pp. 192-197.

Li Z., Xi Y., *Application of acoustic emission technique to detection of concrete cracking and rebar corrosion*, *NDT-CE: Int. Symposium Non-Destructive Testing in Civil Engineering*, Berlin, Germany, 1995,.

Liang M.T., Su P.J., *Detection of Corrosion Damage of Rebar in Concrete Using Impact-Echo Method*, Cement & Concrete Research, 2001, vol. 31, pp. 1427-1436. DOI: 10.1016/S0008-8846(01)00569-5

Pazdera L., Topolář L., Bílek V., Smutný J., Kusák I., Luňák M., *Measuring of Concrete Properties during Hardening*, in Proceedings of the 48th International Scientific Conference on Experimental Stress Analysis, Velke Losiny, Czech Republic, 2010.

Pazdera L., Topolar L., *Application acoustic emission method during concrete frost resistance*, Russian Journal of Nondestructive Testing, 2014, vol.50, issue 2, pp. 127-131. DOI: 10.1134/S1061830914020065

Sagar R.V., *An experimental Study on Acoustic Emission Energy and Fracture Energy of Concrete*. National Seminar & Exhibition on Non-Destructive Evaluation, India, 2009.

Surgeon M., Wevers M., *Modal analysis of acoustic emission signals from CFRP laminates*, NDT & E International, 1999, vol. 32, issue 6, pp. 311-322. DOI: 10.1016/S0963-8695(98)00077-2.

Štefková D., Timčaková K., Topolář L., Cikrle P., *Evaluation of the degree of degradation using the impact-echo method in civil engineering*, *Materiali in tehnologije*, 2016, vol. 50, issue 6, pp. 879-884. DOI: 10.17222/mit.2015.150.

Topolář L., Šimonová H., Misák P., *Effect of Concrete Mixture Composition on Acoustic Emission and Fracture Parameters Obtained from Three-Point Bending Test*, Advanced Materials Research, 2015, vol. 1100, pp. 152-155.

Zhang Y.M,, Chen S.X., Chen B., Sun W., *Dry shrinkage, frost resistance and permeability of rubber included concrete*, Key Engineering Materials, 2006,Vol. 302, pp. 120-124.

6. Comprehensive Monitoring of the Shrinkage and Structural Changes of Cement Composites during Setting and Hardening

Barbara Kucharczyková[1], Libor Topolář[2], Petr Daněk[3], Dalibor Kocáb[4], Ondřej Karel[5]

[1,3,4,5] Brno University of Technology, Faculty of Civil Engineering, Institute of Building Testing, Brno, Czech Republic

[2] Brno University of Technology, Faculty of Civil Engineering, Institute of Physics, Brno, Czech Republic

6.1. Introduction

Determination of the real shrinkage development of cement-based composites is ever more important not only for structural engineers and concrete manufacturers but it is also a very topical problem in the field of the development of mathematical models for the creep and shrinkage prediction in concrete structures (RILEM TC 2015). Advancement in technology and composition of building materials in turn requires advancement in test procedures used for the determination of new materials' physical and mechanical parameters. The main problem in the field of experimental measurement of shrinkage in cementitious materials is to capture the total volume change due to chemical reactions, plastic settlement and desiccation while recording all the characteristics that more or less influence the process and magnitude of shrinkage in particular stages of their setting and hardening.

The main aim of performed experiment was to find measurement equipment and test procedure suitable for obtaining comprehensive information about the structural and volume changes which are in progress especially during the early stage of cement composites setting and hardening.

6.2. Theoretical background

Immediately, after cement is mixed with water, structural and volumetric changes in fresh mixture are in progress (Bentz 2008, Newman & Choo 2003, Neville 2011, Bella et al. 2016). These changes are caused by many factors related to the environmental and curing conditions (Havlásek 2014) as well as to the properties and ratio of raw materials used in the fresh mixture (ed. by Kovler et al. 2006). One of the most monitored phenomenon, which is closely connected with above mentioned matters, is early-age cracking (ed. by Bentur 2003, Deshpande et al. 2007). The high risk of early cracks initiation and propagation occur especially in restrained (Ba et al. 2008, Dong et al. 2014, Loser & Leemann 2009) and massive structures (Lin et al. 2012, Nehdi et al. 2014) because of stresses developed by volumetric changes due to the chemical reactions, temperature development or drying. One of the current approaches to determination of relationship between structural and volumetric changes is the simultaneous measurement of relative length changes and acoustic responses due to chemical reactions, particles solidification or cracking. In recent years, the method of acoustic emission (AE) has also been widely used as a supplemental measurement method for the non-destructive monitoring of the changes in the specimen's internal structure during static and dynamic loading tests as well as for the monitoring of the behaviour of composite materials during setting and hardening (Topolář & Pazdera 2014, Topolář et al. 2016), (Qin et al. 2014, Pirskawetz et al. 2006). The previous studies shown that the AE technique is able to detect the early-age crack formation and cracking progress during the cementitious composite solidification (Qin et al. 2014, Kim & Weiss 2003).

Scientific sources provide a number of approaches to determining the value of particular types of concrete and mortars volume changes (shrinkage, swelling), e.g. (Reinhardt & Grosse 2005, PCA 2017, Holt 2001), (Kratochvíl et al. 2014, Barcelo et al. 2005 Soliman & Nehdi 2011, Mazzoli et al. 2015, Amin et al. 2010, Zhang et al. 2015, Chen et al. 2011, Chen et al. 2010, Yılmaztürk et al. 2004). However, these are mostly methods for separate determination of individual components of shrinkage in the early age. In these cases, the measurement is started immediately or very early after cement is mixed with water. Measurement methods intended to the long-term monitoring of the shrinkage progress due to drying are mostly based on the determination of the relative length changes and the measurement, in most cases, begins after specimens have been removed from their moulds, which is typically no sooner than after 24 hours of ageing. Such methods are summarized e.g. in (Newlands et al. 2008) or they are standardized in the national standards of various countries.

In important or complicated concrete structures, shrinkage is measured directly on a concrete element using a special type of wire strain gauge designed to be embedded in the concrete (Norisham et al. 2008, ed. By Tanabe et al. 2009, Stráský et al. 2014, Zich 2011) or other advanced monitoring technique (Ma et al. 2015).

Guidelines reflecting the recent advances in theoretical and experimental research in the field of the creep and shrinkage of cement composites (especially concrete) have been published under RILEM TC-242-MDC (chair Zdeněk P. Bažant). An article from 2015 (RILEM TC 2015) underlines the necessity of measuring weight losses, especially at the early stage of cement composite ageing, because this characteristic is an important input parameter for the development of mathematical models which are used for the prediction of concrete volume changes. The uncertainty involved in extrapolating drying shrinkage can be considerably reduced in case the weight loss is measured simultaneously with shrinkage (RILEM TC 2015).

6.3. Materials and methods

Testing techniques

In order to select measurement equipment and test procedure suitable for obtaining the relevant measurement outputs, several specifications, which were based on the experience gained over the last ten years in the field of concrete volume changes measurement, were taken into account. The main emphasis was posed on the accuracy, ability to setup the continual measurement with the adjustable storage frequency, ability of continuous measurement of all investigated parameters without specimens handling and ability of simultaneous measurement of all investigated parameters such as length changes, mass losses caused by free drying, temperature development inside the test specimen, acoustic responses of internal structure changes and ambient temperature and relative humidity.

Based on the above-mentioned requirements following measurement equipment was selected. The measurement of length changes was performed using the u-shaped stainless steel shrinkage drains of 1000 mm in length and with 60 × 100 mm in cross-section (Schleibinger Testing Systems 2017) were used. The gauging bases are defined by two anchors placed on heads of drains. One anchor is fixed and the other one is movable and sliding on three wheels. To avoid wall friction the drains were covered with polyethylene foam mat (MIRELON) of 2 mm thickness. The length changes were measured along the central axis of the specimens using an Inductive Standard Displacement Transducers WA2T (HBM 2017) with measuring range of 2 mm. The greatest linearity deviation of these sensors is 0.2% of measuring range. The sensors leaning against the movable anchor of the drain were mounted to the drain in desired position.

This measurement equipment is primarily designed for shrinkage measurement in the early stage of cement composites setting and hardening. In order to facilitate the subsequent long-term measurement of deformations special markers (Kucharczyková et al. 2011) were designed at the Brno University of Technology (BUT). These markers were embedded into the upper surface of the composite placed in the shrinkage drains (see Fig. 6.1.). In this way, two gauging bases were created for further measurement (see Fig. 6.1., Fig. 6.2.). This arrangement enabled the capture of the total relative length changes of the concrete since the moment the concrete is placed into the drain until its long-term ageing after the specimen is removed from the shrinkage drain.

To provide the continuous measurement of mass losses a special weighing table (Vymazal et al. 2015) was also designed at the Brno University of Technology (BUT). The measurement accuracy is guaranteed by a rigid frame and high sensitivity single point load cells of the accuracy class C3MR (HBM 2017). The max. weight capacity is 3kg. The construction and measurement details are under national patent protection (Vymazal et al. 2015).

The shrinkage drains filled with the fresh mixture were placed onto a special weighing table which enabled the simultaneous measurement length changes and mass losses of the test specimens. Measurement data obtained from drains and weighing table were automatically stored using a universal amplifier Quantum X - MX 840 (HBM 2017) with 8 individually configurable inputs (electrically isolated). The data storage frequency was 5Hz. The setup of particular measurement devices before the start of measurement and data storage frequency was performed using the PC software CatmenEasy.

In order to measure temperature development inside the test specimens the platinum thermal sensor COMET PT 1000 was embedded at the end of the shrinkage drains. Measured data were storage with a period of 5 min using a thermometer-logger S0151 for 4 external probes (COMET 2017).

Changes in the specimens' internal structure during the early stage of setting and hardening were monitored using the non-destructive passive method of AE. Magnetic AE sensors (type MDK13 with 35 dB preamplifier) were placed in positions predefined by embedded steel probes (waveguides), see Fig. 2 and Fig. 3, which provide the transfer of acoustic waves generated during material's setting and hardening to the AE sensor.

The internal structure changes were monitored with two AE sensors placed in each shrinkage drain during the measurement – the first one was placed near the movable head of the drain, the second one was located near the other end of the drain. In this way, the progress of events during cement composites setting and hardening was continuously recorded. AE signals were detected by the measuring equipment DAKEL XEDO with two channels for approx. 72 hours. Universal measurement and diagnostic system DAKEL XEDO was used for measurement. This equipment allows sampling of the signal from the AE sensors (speed up to 8 MSamples/sec), enumerates standard acoustic emission parameters, process emission events parameters to localize the feasible (potential) emission source.

The measurement of AE was started simultaneously with the start of relative length changes, mass losses and temperature measurement. In order to evaluate the origin of microcracks during setting and hardening, the measurement was focused on the number of overshoots which exceed the pre-set threshold, which is the most commonly used parameter of the acoustic emission activity. The presence of a high number of microcracks in the specimen is reflected in the high acoustic emission activity.

The ambient temperature and relative humidity were continuously recorded with a period of 15 min by an automatic gauging station COMET (COMET 2017). The above-described measurement equipment and configuration enabled simultaneous measurement of all the parameters being investigated.

The final arrangement of the measurement devices before starting the measurement is shown in Fig. 6.1.

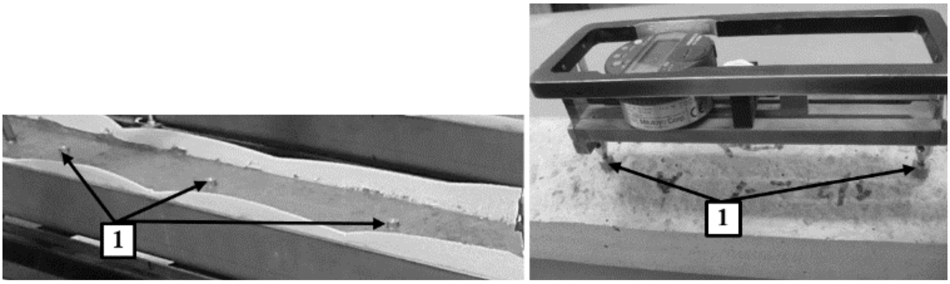

Fig. 6.1. Arrangement for long-term measurement using Hollan's strain gauge (1 – markers for long-term measurement)

The measurement in shrinkage drains can only be started after the concrete has set a little so that it does not push out the movable head of the drain with its own weight. With respect to the consistency of the fresh mixture, measurement was started approximately one hour after the composite was poured into the drains. Investigated parameters was measured in the drains placed on the weighing table in a laboratory at temperature of 21 ± 2 °C and relative humidity of 60 ± 10 % until the specimens was approx. 3 days old.

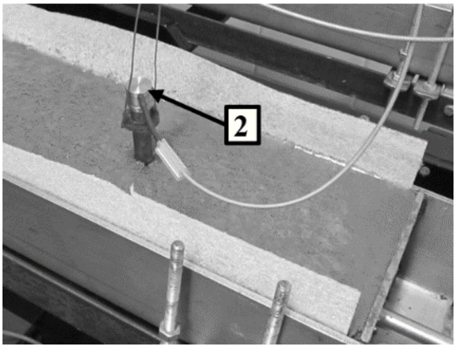

Fig. 6.2. AE sensor with waveguide in shrinkage mould

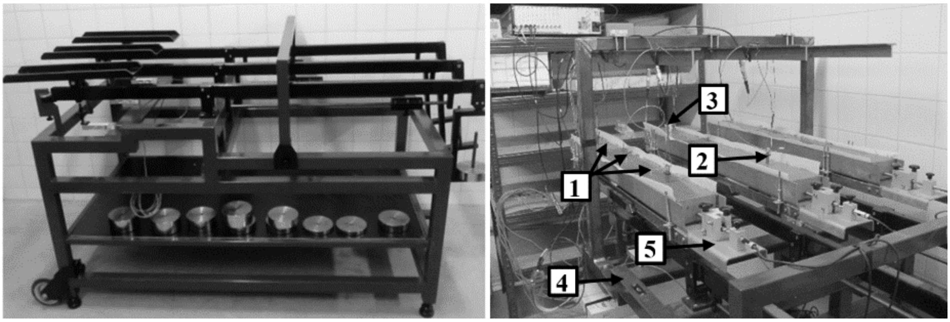

Fig. 6.3. Arrangement of measurement devices (1 – markers for long-term measurement; 2 – AE sensor with waveguide; 3 – temperature sensor; 4 – weighing table; 5 – shrinkage drain)

To verify the sensitivity and accuracy of the weighing table the top surface of the test specimens was not protected from drying. After 3 days the specimens were extracted from the drains and stored in a laboratory at a stable temperature of 21 ± 2 °C and relative humidity of 60 ± 10 %. Further measurements were performed using a Hollan's strain gauge which was fixed onto the surface of the specimens (see Fig. 1). The positions of the gauging points were predefined by the markers embedded at a spacing of 200 mm. The specimens were left to dry freely for the entire time of the measurement and were weighed at regular intervals.

Materials

The main aim of the experimental part was to verify the setup of the test equipment and test procedure intended for the determination of the volume changes in cementitious composites, especially in their early stage of setting and hardening. For this purpose, a fine-grained cement composite with a relatively high w/c ratio was designed and manufactured. The composition is based on the standard ČSN EN 196-1 (Part 1 2005). The fresh composite was made with quartzite sand with the maximum nominal grain size of 2 mm standardized according to ČSN EN 196-1 (Part 1 2005), Portland cement CEM I 42.5 R and water in ratio of 3:1:0.5 (S:C:W). A mixing device with controllable mixing speed was used for the preparation of the fresh mixture. The basic information about the composition, manufacturing and properties of the fresh composite are given in Table 6.1. The properties of the fresh composite were determined in accordance with ČSN EN 1015-3 (Part 3 2000) and ČSN EN 1015-6 (Part 6 1999). The basic properties of hardened composite are summarized in Table 6.2.

Table. 6.1. Properties of fresh composite

Composite ID	Composition [S:W:C]	w/c [-]	Mixing speed [revolutions/min]	Workability [mm]	Bulk density [kg/m^3]
0_04042016	3:1:0.5	0.5	20	140	2200

Table. 6.2. Properties of hardened composite

Composite ID	Age of specimens [days]					
	3	28	90	3	28	90
	Compressive strength [N/mm2] (standard deviation)			Dynamic modulus of elasticity [N/mm2] (standard deviation)		
0_04042016	27.28 (1.84)	36.53 (2.57)	37.62 (2.32)	27340 (669)	27735 (724)	28693 (492)

Note: For the purpose of performed experiment, the test specimens were intentionally no protected from drying during the whole time of ageing. This inappropriate way of curing probably led to decrease in the mechanical properties of the material being investigated.

6.4. Results and discussion

The results of the measurements performed are presented below. Fig. 6.4. shows the progress of relative length changes, relative mass losses and temperature inside the test specimens measured in the early stage of setting and hardening. This method of displaying the recorded data provides a better idea about the relations between the phenomena being investigated. Shortly after the start of the measurement, swelling (length increment, expansion) of the test specimens was recorded. However, decrease in mass of the test specimens was recorded during the same time period as well. An explanation of this phenomenon can be found in the composition of the cement composite and in the development of the temperature measured inside the test specimens. Looking on the material composition it can be stated that the w/c ratio of this composite was rather high (see Tab. 6.1.). No component segregation in the fresh mixture was observed either during the mixing or during the manufacturing of the test specimens. On the other hand, a relatively large amount of water rose to the upper surface of the test specimens after their manufacturing and storing. This phenomenon is commonly known as bleeding. After the plastic settlement has finished, the water which had bled onto the specimen upper surface is drawn back into the setting and later hardening cement paste, re-filling the pores created during cement hydration. This water re-absorption is one of the factors which cause the swelling of concrete (Holt 2001). Another substantial factor which affects the early swelling of cementitious composites is the thermal expansion due to the heat generated during hydration. The phenomenon of swelling/expansion is clearly visible from the measurements in the first 24 hours of ageing when the hydration heat is generated at the highest rate (approx. 200 J/g per 24 h) (Rovnaníková & Žalud 2015). The progress of temperature measured in the specimens confirmed this (see Fig. 4). The highest temperature was recorded approx. 10 hours after the start of measurement. At the same time, a surge of swelling is also visible. Its highest magnitude of 75 µm/m was recorded after 22 hours counted from the start of measurement. Concerning the recorded progress of mass losses, it is clearly visible that the sharp loss in specimens' mass was recorded just before reaching the maximum temperature.

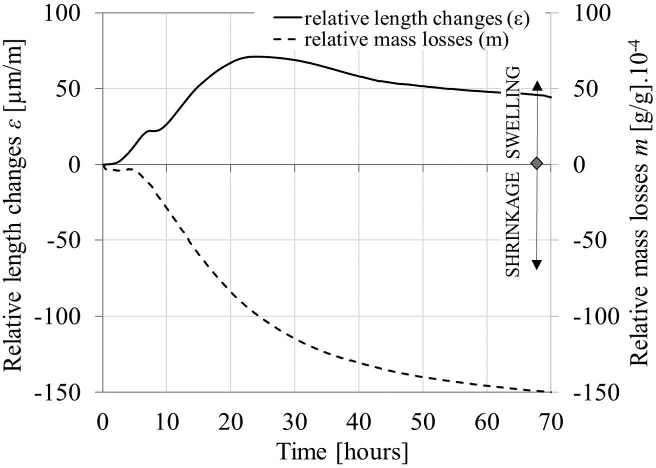

(a)

Fig. 6.4. Progress of relative deformations, relative mass losses and temperature measured inside the test specimens

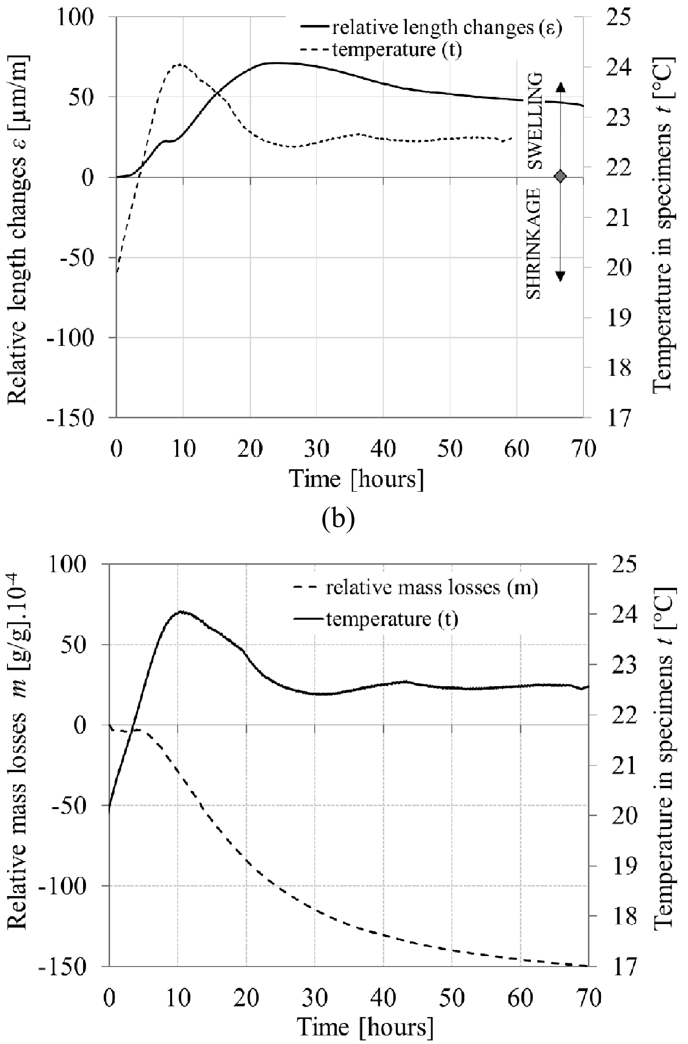

(b)

(c)

Fig. 6.4. cont. Progress of relative deformations, relative mass losses and temperature measured inside the test specimens

Fig. 6.5. shows the progress of relative length changes and mass losses in relation with the AE events obtained during the monitoring of the changes in the specimens' internal structure during the early stage of setting and hardening by means of AE measurement. The acoustic waves recorded by measurement

equipment were conversed to the number of overshoots for the purpose of results interpretation. This number of overshoots indicates the number and size of structural changes being in progress within a certain period. The more activity there is in the specimens' internal structure, the more overshoots are recorded per an interval of time. Fig. 6.5.(a) clearly shows that the activity recorded by the AE corresponded well with the progress of the composite relative length changes. The first high number of overshoots was recorded immediately after the start of the measurement. In this early stage of composite ageing, plastic settlement takes place, which is reflected in the high numbers of AE overshoots. After plastic shrinkage had finished, a period of swelling started. During the whole period of swelling only very low activity was recorded. The numbers of overshoot started to increase immediately after the swelling had stopped and the composite started to shrink (see Fig. 6.5.(a)). Based on the results, it can be assumed that no important internal changes are occurring during the stage of swelling. It means that probably neither water re-absorption nor thermal expansion are the initiators of cracks, in this case, and the composite gains strength without internal cracking. It should be emphasized that in this case the shape of specimen, especially its cross section, plays an essential role.

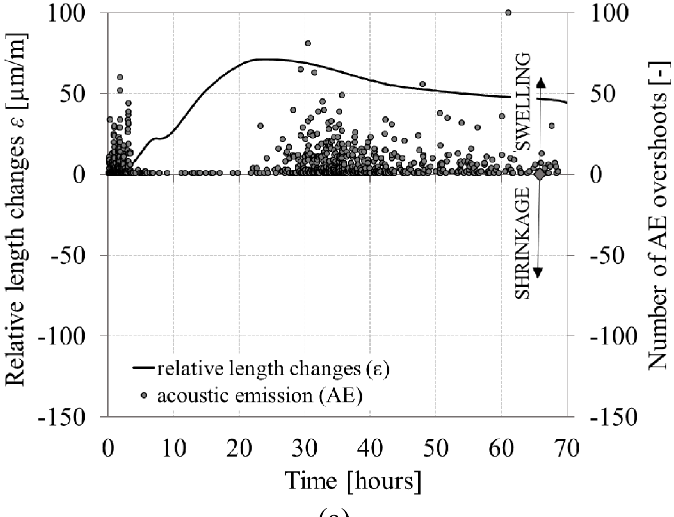

(a)

Fig. 6.5. Progress of relative deformations, mass loss and AE overshoots

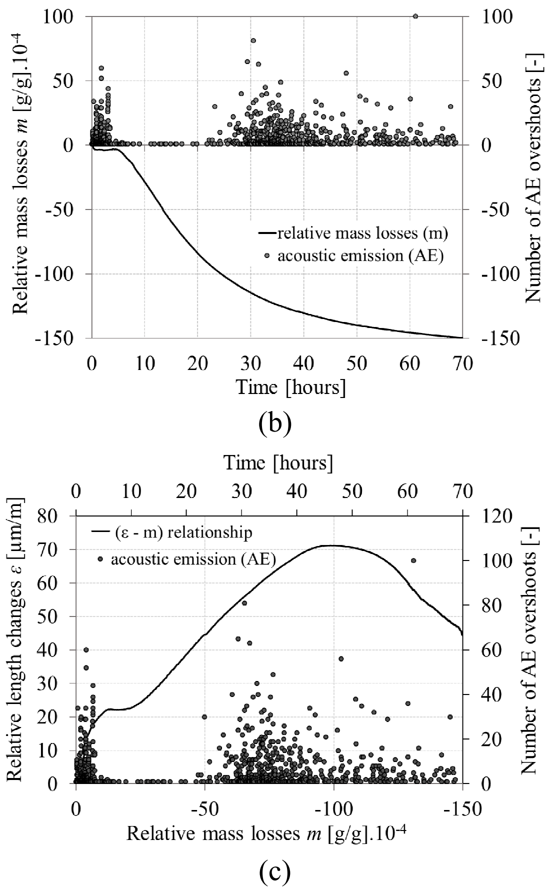

Fig. 6.5. cont. Progress of relative deformations, mass loss and AE overshoots

Concerning the progress of total volume changes, the period of initial expansion (swelling) appears not to be very significant in terms of its magnitude (see Fig. 6.6.(a)). However, from the perspective of strength development this phenomenon seems fairly interesting. Early age volume changes can influence tensile stress and crack formation in a hardened cement composite which is then visibly reflected in later development of its tensile and compressive strength as well as in the resistance of the composite to later crack formation and propagation. The period of swelling occurs within the first 24 hours when the cement composite is very delicate and the risk of internal cracking is very high. As stated above, the results of the measurements presented in Fig. 6.5. show a very low activity in the internal structure of hardened composite during the period of swelling – it can be assumed that no significant cracks are created. The initial expansion delayed the start of shrinkage by more than 20 hours. This delay can be of great benefit to the later development of physical and mechanical properties of the cement composite. The absence of early cracking in this period may result in overall increase in durability of the cement composite element.

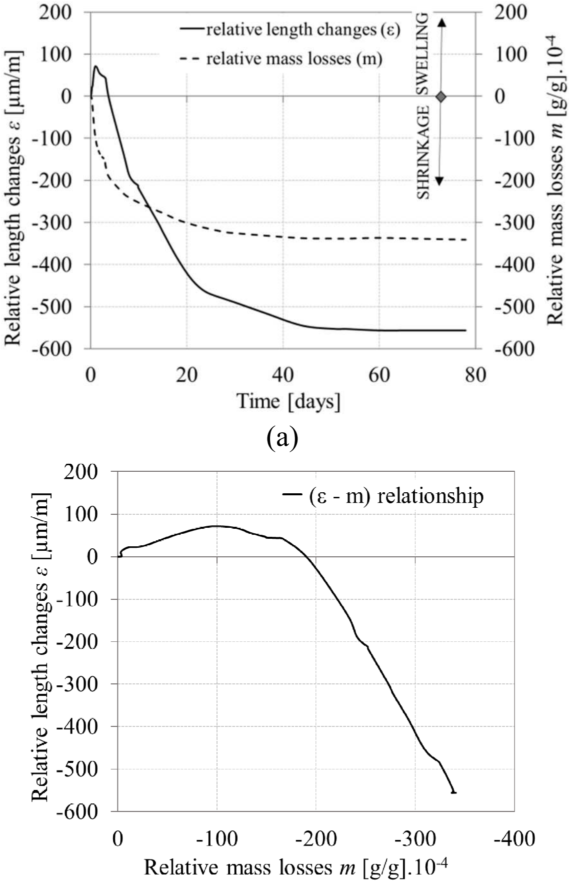

(a)

(b)

Fig. 6.6. Progress of relative deformations and mass losses measured over the whole time of the composite's ageing

6.4 Conclusions

The measurement technique described in this chapter and used in the experiment satisfies the requirements for the early age diagnosis of the material's behaviour. Readings obtained from the shrinkage drains, weighing table, apparatus for detection of AE and devices for temperature and humidity measurement provided comprehensive information about the behaviour of the material especially in the early stage of its setting and hardening.

In conclusion, the measurement results suggest the following:

- Measurements have to start as soon as the cement composite has been poured into a mould if a comprehensive assessment of the parameters influencing volume changes is to be made. The consistency of the fresh mixture as well as the capabilities and limitations of the measurement equipment must be taken into account. The shrinkage drains can be considered suitable for the measurement of volume changes in cement composites of varied workability. The measurement should usually be started no later than one hour after the composite is poured into the drain. Generally speaking, the lower the workability of the composite, the sooner the measurement can begin.
- Continuous measurement of the mass losses of the cement composite caused by free drying of the specimen surface provided useful data for result interpretation of the measurement of volume changes in cement composites. This data then be of great use in creating new mathematical models designed for the prediction of volume changes in cement composites as well as in fine-tuning existing ones. The measured progress of mass losses corresponds well to the progress of relative length changes and to the progress of temperature measured inside the test specimens. The relationship between relative length changes and relative mass losses was observed over the whole time of its ageing (see Fig. 6.5.(b) and Fig. 6.6.(b)). However, the initial part of the curve is influenced by water re-absorption and thermal expansion. Just before reaching the maximum temperature a sharp loss in specimen mass was recorded (see Fig. 6.4.(c)). The measurement results can provide information as to how much the water loss and release of hydration heat contribute to the overall progress of volume changes.
- The method of acoustic emission appears to be another suitable tool for determining the structural changes and occurrence of micro-cracks during the setting and hardening of a cement composite. In general, the higher the numbers structural changes and micro cracks, the greater a number of AE overshoots is recorded. The number of micro-cracks in the cement composite essentially affects its final mechanical properties (i.e. strength, modulus of elasticity, fracture parameters, durability, etc.). The application of the AE method for continual monitoring of cement composites during the setting and hardening can be instrumental in the early detection of micro disruptions. This information about the behaviour of the material may be later used for improving the material composition or adjusting the curing method which

csimonovan both lead to designing cement composite structures with better properties and higher durability.

- The testing technique described herein is currently commonly used at the Institute of Building Testing of BUT, FCE. The measurement results were published in following papers (Kucharczyková et al. 2017, Topolář 2017)

The presented results were obtained within the implementation of the project No. 17-14302S "Experimental analysis of the early-age volume changes in cement-based composites", supported by the GACR - Czech Science Foundation.

References

Amin M., Kim J-S. Dat T., Kim J-K., *Improving test methods to measure early age autogenous shrinkage in concrete based on air cooling*, The IES Journal Part A: Civil & Structural Engineering, 2010, 3(4), 244-256, DOI: 10.1080/19373260.2010.522314.

Ba H., Su A., Gao X., Tao Q., *Cracking tendency of restrained concrete at early ages*, Journal of Wuhan University of Technology-Mater. Sci. Ed, 2008, 23(2), 263-267, DOI: 10.1007/s11595-006-2263-7.

Barcelo L., Moranville M. Clavaud B., *Autogenous shrinkage of concrete: a balance between autogenous swelling and self-desiccation*, Cement and Concrete Research, 2005, 35(1), 177-183, DOI: 10.1016/j.cemconres.2004.05.050.

Bentz D.P., *A review of early-age properties of cement-based materials*, Cement and Concrete Research, 2008, 38(2), DOI: 10.1016/j.cemconres.2007.09.005.

Chen T.C., Ferraro C.C., Yin W.Q., Ishee C.A., Ifju P.G., *A novel two-dimensional method to measure surface shrinkage in cementitious materials*, Cement and Concrete Research, 2010, 40(5), 687-698, DOI: 10.1016/j.cemconres.2009.11.013

Chen T.C., Yin W.Q., Ferraro C., Charles C.A., Ifju P.G., *Shrinkage measurement of concrete using the cure-reference method*, Experimental Techniques, 2011,35(2), 61-67. DOI: 10.1111/j.1747-1567.2009.00577.x.

COMET 2017, http://www.cometsystem.com/

ČSN EN 1015-3:2000, *Methods of test for mortar for masonry - Part 3: Determination of consistence of fresh mortar (by flow table)*, Prague: ČNI (in Czech), This standard is the Czech version of the European Standard EN, 1015-3:2000.

ČSN EN 1015-6:1999, *Methods of test for mortar for masonry - Part 6: Determination of bulk density of fresh mortar*, Prague: ČNI (in Czech), This standard is the Czech version of the European Standard EN 1015-6:1999.

ČSN EN 196-1:2005, *Methods of testing cement - Part 1: Determination of strength,* Prague: ČNI (in Czech), This standard is the Czech version of the European Standard EN 196-1:2005.

Deshpande S,, Darwin D., Browning J., *Evaluating Free Shrinkage of Concrete for Control of Cracking in Bridge Decks*, Structural Engineering and Engineering Materials, SM Report, The University of Kansas Center for Research, Inc. Lawrence, Kansas, 2007, No. 89, Kansas.

Di Bella C., Griffa M., Ulrich T.J., Lura P., *Early-age elastic properties of cement-based materials as a function of decreasing moisture content*, Cement and Concrete Research, 2016, 89(2016), pp. 87-96, DOI: 10.1016/j.cemconres.2016.08.001.

Dong W., Zhou X., Wu Z., *A fracture mechanics-based method for prediction of cracking of circular and elliptical concrete rings under restrained shrinkage*, Engineering Fracture Mechanics, 2014, 131, pp. 687-701, DOI: 10.1016/j.engfracmech.2014.10.015.

Ed. by Bentur A., *Early age cracking in cementitious systems: Report of RILEM Technical Committee 181-EAS 'Early Age Shrinkage Induced Stresses and Cracking in Cementitious Systems'*, Bagneux: RILEM, 2003, Publ, ISBN 2912143330.

Ed. by Kovler K., Jensen O., Lura P., *Proceedings pro052: International RILEM Conference on Volume Changes of Hardening Concrete: Testing and Mitigation*, Bagneux, France: RILEM Publications, 2006,428 p. ISBN 2-35158-004-4.

Ed. by Tanabe T., Sakata K., Mihashi H., Sato R., Maekawa K., Nakamura H., *Creep, shrinkage and durability mechanics of concrete and concrete structures,* Proceedings of the eighth International Conference on Creep, Shrinkage and Durability of Concrete and Concrete Structures, Ise-Shima, Japan, Boca Raton: CRC Press, 2009, ISBN 9780203882955.

Havlásek P., *Creep and Shrinkage of Concrete subjected to variable Environmental Conditions*, Prague, PhD Thesis, CTU, Faculty of Civil Engineering, Supervisor: Jirásek Milan, 2014.

HBM, *Instruments-QuantumX: Universal and distributable-DAQQuantumX MX840B*. HBM: measure and predict with confidence, 2017 https://www.hbm.com.

HBM, *Sensors-displacement sensors-WA T. HBM: measure and predict with confidence*, 2017, https://www.hbm.com.

HBM, *Sensors-Load Cells [kg/lbf]-Single Point Load-CellsPW6C*. HBM: measure and predict with confidence, 2017, https://www.hbm.com.

Holt E., *Early age autogenous shrinkage of concrete*, Espoo: Technical Research Centre of Finland, 184 p. + app. 9p. ISBN 95-138-5870-7. *VTT Publications 446*, Technical Research Centre of Finland, 2001,.

Kim B., Weiss W.J., *Using acoustic emission to quantify damage in restrained fiber-reinforced cement mortars*, *Cement and Concrete Research*, 33(2), 2003, pp. pp. 207-214, DOI: 10.1016/S0008-8846(02)00978-X.

Kratochvíl M., Kadlec M., Terzijski I., Zvolánek L., *Autogenous Shrinkage and its Measurement since the Moment of Concrete Casting*, (Autogenní smršťování a jeho měření od okamžiku uložení betonu), Beton: Technologie, konstrukce, sanace, Praha: Czech Concrete Society, 2014, 14(3), pp. 64-67, ISSN 1213-3116 (in Czech)

Kucharczyková B., Daněk P., Misák P., Vymazal T., *Apparatus for measuring relative deformation of concrete and cement composites*, Czech Republic, CZ 21600 U1 Utility model, applied 16.10.2010, granted 12.1.2011, entered 6.1.2011, Available from: https://www.upv.cz/en/ip-rights/patents.html.

Kucharczyková B., Topolář L., Daněk P., Kocáb D., Misák P., *Comprehensive testing techniques for the measurement of shrinkage and structural changes of fine-grained cement-based composites during ageing*, Advances in Materials Science and Engineering, 2017, vol. 2017, Article ID 3832072, 10 p., DOI: 10.1155/2017/3832072.

Lin F., Song X., Gu X., Peng B., Yang L., *Cracking analysis of massive concrete walls with cracking control techniques*, Construction and Building Materials 31, 2012, pp. 12-21, DOI: 10.1016/j.conbuildmat.2011.12.086.

Loser R., Leemann A., Shrinkage and restrained shrinkage cracking of self-compacting concrete compared to conventionally vibrated *concrete*, Materials and Structures, 2009, 42(1), pp. 71-82, DOI: 10.1617/s11527-008-9367-9.

Ma P., Lin H., Lan H., Chen F., *Multi-dimensional SAR tomography for monitoring the deformation of newly built concrete buildings*, ISPRS Journal of Photogrammetry and Remote Sensing, 2015, 106,pp. 118-128, DOI: 10.1016/j.isprsjprs.2015.04.012.

Mazzoli A., Monosi S., Plescia E., *Evaluation of the early-age-shrinkage of Fiber Reinforced Concrete (FRC) using image analysis methods*, Construction and Building Materials, 2015, 101, pp. 596-601,

DOI: 10.1016/j.conbuildmat.2015.10.090.

Nehdi M., Shareef K., Algoneid K., *Mitigating thermal cracking in massive scc slab foundations for a wastewater pumping station*, Concrete International, 2014, 36(7), pp. 38-44.

Neville A.M., *Properties of Concrete,* 5th edition. 2011, ISBN 978-0-273-755-807.

Newlands M., Paine K., Vemuri N., Dhir R., A linear test method for determining early-age shrinkage of concrete, Magazine of Concrete Research, 2008,60(10), pp. 747-757, DOI: 10.1680/macr.2008.00004.

Newman J.,Choo B.S., *Advanced concrete technology: Concrete properties*, Amsterdam: Elsevier, 1 ed., 2003, ISBN 07-506-5104-0.

Norisham I., Omenzetter P., Lipscombe P., *Monitoring system for in-situ measurement of creep and shrinkage effects in a prestressed concrete bridge*, In: 20th Australasian Conference on the Mechanics of Structures and Materials*,* Toowoomba, Australia 2008, pp. 767-771.

PCA 2017, The Portland Cement Association, http://www.cement.org.

Pirskawetz S., Weise F., Fontana P., *Detection of early-age cracking using acoustic emission.* In: Proceedings pro052: International RILEM Conference on Volume Changes of Hardening Concrete: Testing and Mitigation, Bagneux, France: RILEM Publications, 2006, pp. 385-392, ISBN 2-35158-004-4.

Qin L., Ren H-W., Dong B-Q., Xing F., *Acoustic emission behavior of early age concrete monitored by embedded sensors*, Materials, 2014, 7(10), pp. 6908-6918, DOI: 10.3390/ma7106908.

Reinhardt H.W., Grosse C.U., *Advanced testing of cement based materials during setting and hardening*, Bagneux, France: RILEM Publications, 2005, 341 p. ISBN 29-121-4381-0.

Rilem T.C., *RILEM draft recommendation: TC-242-MDC multi-decade creep and shrinkage of concrete*, Materials and Structures, 2015, 48(4), pp. 753-770, DOI: 10.1617/s11527-014-0485-2. ISSN 13595997.

Rovnaníková P., Žalud O., *Effect of admixtures and fine grain of aggregate on the portland cement hydration, In: Trvanlivost 2015*, Brno: Faculty of Civil Engineering (in Czech), BUT, 2015, pp. 123-136.

Schleibinger Testing Systems 2017, http://www.schleibinger.com.

Soliman A., Nehdi M., *Effect of drying conditions on autogenous shrinkage in ultra-high performance concrete at early-age*, Materials and Structures, 2011, 44(5), pp. 879-899, DOI: 10.1617/s11527-010-9670-0.

Stráský J., Zich M., Novotný P., *Bridges with progressivelly erected decks,* In: CIV - SPRING 2014, Calgary, pp. 19-22, https://csce.ca/custom-content/uploads/2012/04/CIV-Spring2014-DE.pdf?e2716b

Topolář L., Pazdera L., *Acoustic emission in protected and non-protected concrete during the first 24 hours*, Applied Mechanics and Materials, 2014, pp. 149-1152, DOI: 10.4028/www.scientific.net/AMM.578-579.1149.

Topolář L., Misák P., Kocáb D., Matysik M., *Applying method of acoustic emission for monitoring of different concrete mixture during setting and hardening*, Solid State Phenomena, 2016, 249, pp. 91-95, DOI: 10.4028/www.scientific.net/SSP.249.91.

Topolář L., Pazdera L., Kucharczyková B., Smutný J., Mikulášek K., *Using acoustic emission methods to monitor cement composites during setting and hardening,* Applied Sciences, 2017, 7(5), 451, DOI: 10.3390/app7050451.

Vymazal T., Daněk P., Kucharczyková B., Misák P., *Continuous measurement method of cement composite weight losses in early phase of setting and hardening, and apparatus for making the same*, Czech Republic, CZ 304898 B6 Patent, CZ 304898 B6 Patent, granted 26.11.2014, entered 7.1.2015. Available from: https://www.upv.cz/en/ip-rights/patents.html

Yılmaztürk F., Kulur S., Pekmezci B.Y., *Measurement of shrinkage in concrete samples by using digital photogrammetric methods*, Research Gate, 2004,.

Zhang J., Gao Y., Han Y., Wang J. *Evaluation of shrinkage induced cracking in early age concrete: From ring test to circular colum*, International Journal of Damage Mechanic, 2015,DOI: 10.1177/1056789515618531.

Zich M., *The concept of a long-term monitoring of highway d47 bridges (Koncepce dlouhodobého sledování mostů na dálnici D47)*, Beton: Technologie, konstrukce, sanace, Prague: Czech Concrete Society, 11(4), ISSN 1213-3116. (in Czech), 2011.

7. Impedance spectroscopy, a method to determine physical and chemical properties of construction materials

Miroslav Lunak[1], **Ivo Kusak**[1]
[1] *Institute of Physics, Faculty of Civil Engineering, Brno University of Technology, Veveri 95, 602 00 Brno, Czech Republic*

7.1. Introduction

Impedance spectroscopy (IS) is a method that employs the impedance frequency dependence to characterize various solids and liquids. To carry out the characterization, IS employs the impedance and phase versus frequency plots, or the so called Nyquist plot, i.e., displaying the impedances in the complex plane throughout the entire frequency range. IS has become a popular method of material research and development, requiring relatively simple electric measurements, which are non-destructive in most cases, and can be automated easily.

To characterize polarization processes, permittivity and impedance are most frequently used in practical applications. As follows from Maxwell's material equations (Szántó 2003), the permittivity is a proportionality constant between the electric field intensity vector and the electric induction vector. An analogous approach can be used to express the impedance and its components.

An ideal dielectric is made up of a substance containing only charges that are bound by electrostatic forces. A real dielectric differs from the ideal one by free electric charges which are causing an undesirable electric conductivity. The physics of dielectric deals with the motion of electric charges. Only electric polarization takes place in ideal dielectrics. Under the influence of an electric field, bound charges shift from their equilibrium positions by a short, limited distance. If the substance contains polar molecules, the electrically bound charges are oriented in the direction of the electric field (Palai-Dany 2009).

Different polarization mechanisms are distinguished with regard to the state and behaviour of the dielectrics in an electric field. Several different polarization types frequently happen to occur simultaneously, stronger mechanisms overlapping the weaker ones (Kocman 1971).

There are a number of the impedance measuring methods. In this paper, we describe a new method, designed by ourselves, to measure and analyse physical and chemical properties of construction materials, indicating the equations and circuit diagrams employed.

The impedance being a complex quantity, at least two related quantities must be measured to determine the impedance. The quantities most frequently used are the electric resistance and the phase change across the unknown impedance. The measuring methods differ from each other in several factors, which are above all the price, frequency and impedance range and automated measurement feasibility.

7.2. Measuring systems and block diagrams

Following devices have been used for the testing of building materials by means of the impedance spectroscopy method: Agilent 33220A RC generator, Agilent 54645A double channel storage oscilloscope, Agilent 82357A PC card, IEEE-488 communication cables and coaxial cables with BNC connectors (Kusák, Luňák).

To measure electric properties of two-pole and four-pole networks, a ZNC vector analyser made by Rohde & Schwarz can be used as a stand-alone analysing unit. The instrument is equipped, among others, with a SPEAG-made DAK-12 probe, which is primarily designed to measure and analyse the permittivity and its components.

The mentioned devices are integrated into an automated measuring unit.

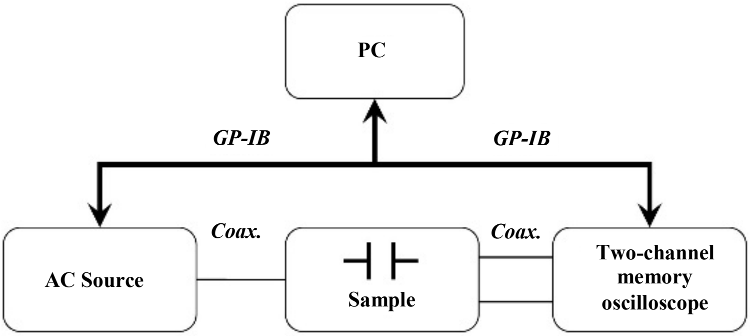

Fig. 7.1. Interconnection of Agilent 33220A RC generator, the specimen and the testing system by means of cables

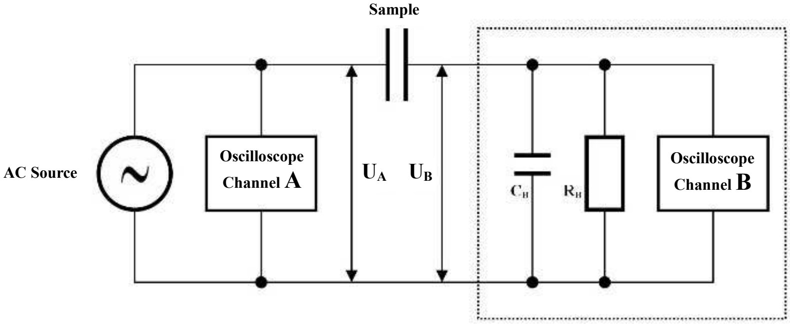

Fig. 7.2. Detailed instrument connection: AC voltage supply, specimen under test, double-channel oscilloscope (the dashed-line limited region indicates the oscilloscope B-channel input parameters)

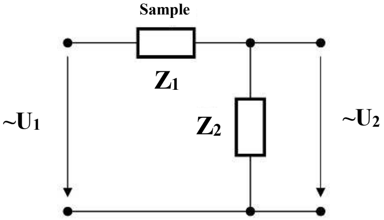

Fig. 7.3. A simplified circuit diagram.

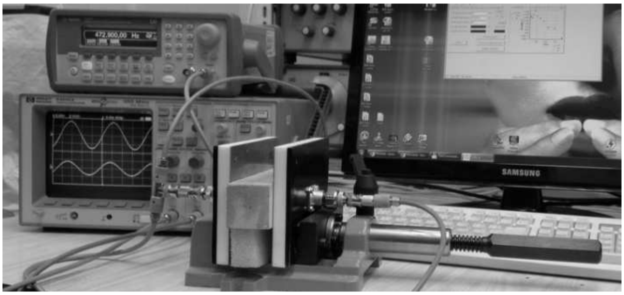

Fig. 7.4. The measuring setup: an AC voltage supply (Agilent 33220A RC generator), double channel oscilloscope, specimen under test in a fixture, and PC with a measuring software.

Depending on the branch of science employing IS, there are different variants of the measuring setup layout. In electrochemistry, the material is collected in electrochemical containers (cells), which are adapted for two-, three- and four-electrode measurements. In the thin film branch, conducting electrodes are deposited on the specimen under investigation, or, depending on the measured specimen surface properties (conductivity, roughness), conducting pastes or coats of paint are used.

The fixture consists of an outer part, which is made of a steel section of appropriate seize and strength. From the outside, a borehole is drilled, around which a nut of chosen size is welded. A threaded rod with a handle passes through the nut. The threaded rod fits close on a metal bed, which is fastened to a metal slab by spot weld. The slab encircles a teflon plate to distribute the pressure from the screws over the teflon plate surface. The teflon plate is attached by means of small bolts. Opposite this teflon plate, another teflon plate is attached at the outer fastener. Brass plate electrodes are affixed to roughened inner surfaces of the teflon plates by means of a two-component adhesive. Lead-in cables are soldered with tin to the brass electrode outer sides to connect them to measuring instruments. Under both of the teflon plates, there is the third teflon plate.

The brass contact electrodes have an area of 3 x 10 cm. The thickness of the electrode brass sheet is 0.7 cm. The outer earthed shielding is made of the same brass sheets, which were connected to the frame by means of four M4 bolts and riveting nuts for each pressure plate. The brass electrodes were affixed to the roughened teflon surfaces by means of a two-component adhesive. The pressure steel plates have an area of 13.5 x 11 cm and a thickness of 4 mm. A teflon plate of the same area as the pressure plates and a thickness of 11.5 mm serves as an insulating element. The slab encircles a teflon plate to distribute the pressure from the screws over the teflon plate surface. The electrode lead-out wires are connected to an N-type flange-mounted coaxial connector. Taking into account a large number of coaxial cable terminations, the output can be modified to fit BNC, SMA, FME and other connectors. The frame of the whole fixture consists of a cast-iron vice with a threaded bar. The electrode pressure force on the specimen surface is being adjusted manually by the operator.

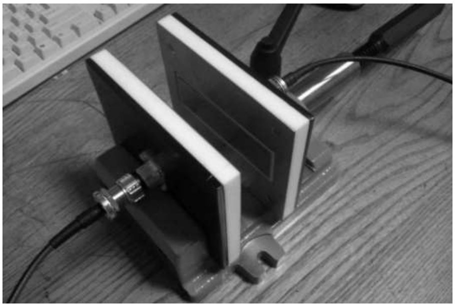

Fig. 7.5. Overall appearance of the fixture for applying plate electrodes to slab specimens of variable thickness

7.3. Formulas applied

To characterize polarization processes, the permittivity and the impedance are most frequently used in practical applications. As follows from the Maxwell's material equations (Szántó 2003), the permittivity is a proportionality constant between the electric field intensity vector and the electric induction vector. An analogous approach can be used when expressing the impedance and its components.

The formulas given below have already been rearranged to correspond to the circuit diagram with the particular measuring instruments used (Fig. 7.4).

In the impedance spectroscopy, the frequency dependence of the quantities in question is being evaluated on the basis of the voltage ratios and phase shifts between the oscilloscope A, B, inputs.

The measured gain L is defined as

$$L = 20 \log K \tag{7.1}$$

where $K=U_B/U_A$ (U_B, U_A are electric voltages in the B, A oscilloscope inputs, respectively). It appears that the system (specimen) of Fig. 7.3 is best represented by a parallel RC equivalent circuit.

The next step to take is therefore to express the phase of the impedance consisting of a precision resistor, R_B, and a precision capacitor, C_B, in B input of the phase and gain measuring instrument. It is

$$\varphi_B = -\arctan \omega R_B C_B \tag{7.2}$$

The impedance of the R_B, C_B parallel network in the B input of the phase measuring instrument is

$$Z_B = \frac{\sqrt{R_B^2 + (\omega R_B^2 C_B)^2}}{1 + (\omega R_B C_B)^2} \tag{7.3}$$

and the phase of the measured impedance Z is

$$\varphi_1 = \varphi_B + \arctan \frac{\sin \Delta\varphi}{\dfrac{U_B}{U_A} - \cos \Delta\varphi}. \tag{7.4}$$

The absolute value of the measured impedance will therefore be

$$Z = \frac{Z_B \cdot \sin \Delta\varphi}{\dfrac{U_B}{U_A} - \sin(\varphi_B - \varphi_1)}, \tag{7.5}$$

(Here, $\Delta\varphi$ is the phase shift between the A, B inputs of the double-channel oscilloscope, φ_1 –is the phase of the specimen under measurement).

The real and imaginary parts of the impedance Z are

$$\mathrm{Re}(Z) = Z \cdot \cos\varphi_1 \qquad \mathrm{Im}(Z) = Z \cdot \sin\varphi_1 . \tag{7.6}$$

Hence, the loss factor of the insulating material, which is defined as the ratio of the real and imaginary part of the impedance Z, is

$$\tan\delta = \frac{\mathrm{Re}(Z)}{\mathrm{Im}(Z)} = \frac{1}{\tan\varphi_1} . \tag{7.7}$$

Depending only on the material itself but not on the specimen geometry, the loss factor is a very important material constant.

The resistance of the parallel *RC* network representing the measured system then is

$$R = \mathrm{Re}(Z) \cdot (1 + \tan^2\varphi_1) . \tag{8.7}$$

and its capacity

$$C = -\frac{\tan\varphi_1}{\omega R} \tag{9.7}$$

A theory of dielectric polarization was formulated by Debye (MacDonald, J R 1987) for homogeneous materials. However, experiments carried out on real materials and the respective conclusions did not show to be in agreement with the fundamental theories. K S Cole and R H Cole and, also, Fuoss and Kirkwood, started from the Debye's theory to derive models of a dielectric which appear to fit experiment results and conclusions (Mentlík 2006) more closely. The behaviour of a dielectric in an AC electric field is best described in terms of the complex relative permittivity. Debye has derived a formula for the complex relative permittivity, ε^*, of weakly polar liquid dielectrics, as follows:

$$\varepsilon^*(j\omega) = \varepsilon_\infty + \frac{\varepsilon_\mathrm{s} - \varepsilon_\infty}{1 + j\omega\tau} , \tag{7.10}$$

Here τ is the relaxation time, independent of the time, however dependent on the temperature, ε_S – static permittivity (frequency → 0 Hz), ε_∞ – optical permittivity (frequency → ∞ Hz), angular frequency $\omega=2\pi f$, f – frequency of the exciting electric field.

Following equation holds for the loss factor tan δ:

$$\tan\delta = \frac{\varepsilon''(\omega)}{\varepsilon'(\omega)} = -\frac{(\varepsilon_\mathrm{S} - \varepsilon_\infty)\omega\tau}{\varepsilon_\mathrm{S} + \varepsilon_\infty\omega^2\tau^2} . \tag{7.11}$$

There are several different relaxation times in a real dielectric. Their distribution is described by a distribution function. Exact determination of a suitable distribution function being difficult, an approximation by a properly selected analytical function is usually carried out. According to Cole's function, the complex relative permittivity can be expressed as follows:

$$\varepsilon^*(j\omega) = \varepsilon_\infty + \frac{\varepsilon_S - \varepsilon_\infty}{1 + (j\omega\tau_1)^{1-\alpha}}, \tag{7.12}$$

Here, τ_1 is the most probable relaxation time, around which the particular relaxation times are distributed according to a distribution function $f(\tau)$, where α is a distribution parameter ($0<\alpha<1$).

J R MacDonald suggested an equivalence between the complex relative permittivity as described by equations (10), (12), and the formulas for the complex impedance Z (MacDonald 1987). Formulas for the real and imaginary components of the complex relative permittivity have been derived and, based on the above mentioned equivalence, equations for the components of the complex specific impedance have been obtained (Barsoukov 2005).

Cole and Davidson have expressed the complex relative permittivity by squaring the whole numerator in formula (12) ($0<\gamma<1$).

$$\varepsilon^*(j\omega) = \varepsilon_\infty + \frac{\varepsilon_S - \varepsilon_\infty}{(1 + j\omega\tau_1)^{\gamma}} \tag{7.13}$$

Havriliak and Negami have put forward a new formula for ε^*, which is, according to their literature search, applicable to complex structure materials (MacDonald 1987).

$$\varepsilon^*(j\omega) = \varepsilon_\infty + \frac{\varepsilon_S - \varepsilon_\infty}{(1 + (j\omega\tau_1)^{1-\alpha})^{\beta}} \tag{7.14}$$

Here, α is a parameter, characterizing the width of the relaxation spectrum ($0<\alpha<1$), β is a parameter characterizing the dispersion curve asymmetry ($0<\beta<1$). The behaviour of a dielectric can now be described by means of five parameters, namely, ε_S, ε_∞, α, β, τ_1; unfortunately, their determination is rather difficult (MacDonald 1987).

Using an appropriate software package, parameters of the three model types will be searched for the material under investigation. The degree of correlation between the model and experiment properties is expressed by means of Pearson's correlation coefficient r.

7.4. Modelling on the basis of ceramic shard specimen measurement results

The ceramic shard specimens have been manufactured using Chvaletice fly ash, their firing temperature being 1 050 °C. The firing losses amounted to 11.2 %. The volume density was about 2 005 kg/m^3. The water absorption capacity: 7.5 %. The bending strength: 24.7 MPa. The grain size distribution: about 5 % on a 0.063 mm sieve. The different specimens differed in the admixture only. The specimen thickness was 10 mm.

Brass plates of a surface area of 40x23 mm, which are pressed against the specimen surface by means of a screw fixture, were used to interface the specimen.

Admixtures

Bentonite ($Al_2O_3.4SiO_2.nH_2O$) - clay. It is a white to light-yellow powder material featuring a specific chemical composition. It is used as ceramics plasticizing agent in the ceramic industry. In this research, a non-activated bentonite, in which the calcium and magnesium ions have not been replaced by activation by sodium ions, has been used. The apparent volume density was 936 kg/m3, pH = 8.7.

Sodium water glass Na_2SiO_3 of a silicate module of 1.6 and a density of 1 560 kg.m^{-3} has been used to prepare the specimens.

Phosphoric acid - application of H_3PO_4 to aluminates results in the generation of aluminium phosphates - $AlPO_4$, which are decomposing at temperatures over 1 500 °C, giving rise to P_2O_5, which escapes. Mechanical properties improve with growing temperature, particularly, in the presence of Cr_2O_3 (Tupy, M).

The loss factor is a material characteristic, whereas the remaining two quantities are related to the specimen type in question only. Prior to the model application, the values of the variables (Re*Z*, Im*Z*) have been divided by the specimen thickness and multiplied by the electrode surface area (it is assumed that only the electric field in the space between the electrodes plays the role; in view of the high material resistivity, the effect of the field beyond the electrodes is neglected). In this way, specific resistance (Real $z(f)$, Re $z(f)$) and reactance (Imag $z(f)$, Im z(f)) versus frequency plots have been obtained for the material under investigation. At the same time, from our readings of (Re$Z(f)$, Im$Z(f)$, the real ($\varepsilon_{\mathrm{real}}$ (f)) and imaginary ($\varepsilon_{\mathrm{imag}}$ (f) components of the complex relative permittivity versus frequency functions have been derived and calculated, which have also been modelled (having been denoted ε' a ε'' formerly). In what follows, the complex relative permittivity will also be briefly termed the complex permittivity.

Three types of the model will be distinguished. Model No. 1 – based on mathematical formula 12, model No. 2 – based on method No. 13, model No. 3 – based on mathematical formula 14. The parameter τ_1, which appears in the mentioned terms, will be designated τ.

The measurements were carried out at common laboratory conditions (room temperature, 24 °C, air humidity, 30 %, atmospheric pressure, 1 000 hPa approximately), silver-based conducting paint was not spread over the specimen faces.

The different specimens are referred to in an abbreviated way, the admixture, which is characteristic for each specimen, being mentioned in the specimen designation (bentonite 5 %, bentonite 10 %, phosphoric acid, water glass, etc.).

Over 50 points have been obtained for each characterization. The measurements were carried out at frequencies ranging from 40 Hz to 1 MHz .

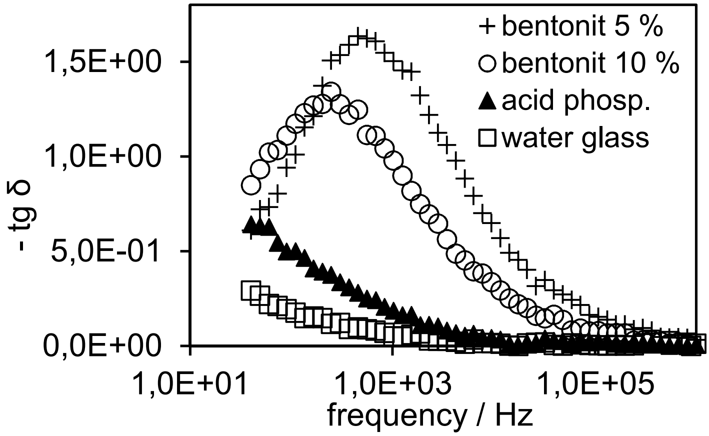

Fig. 7.6. Loss factor versus frequency plots for all ceramic specimens

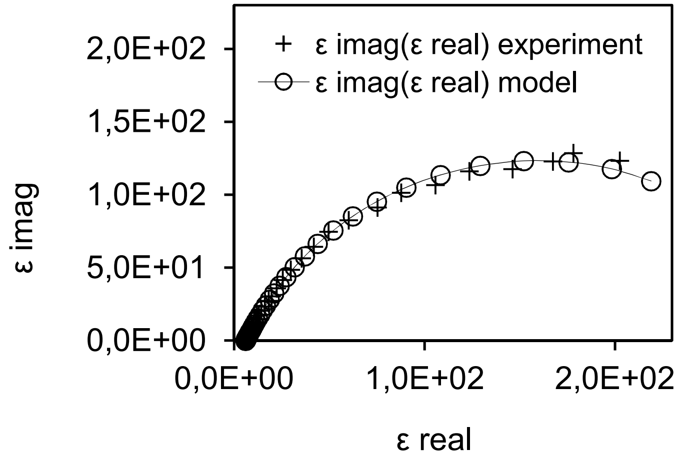

Fig. 7.7. Measured and model plots of the complex permittivity imaginary component versus the complex permittivity real component. 5 % of bentonite containing ceramics. Model type 2, based on the loss factor spectrum shape best fit.

Heavy differences are apparent in the spectra of ceramics specimens featuring different admixtures (see Fig 7.6). The loss factor is minimum for water-glass-admixtured ceramics. From this function frequency-upwards, the difference from the same function for a phosphoric-acid-admixtured specimen is steadily decreasing with growing frequency. Local peaks are observed in ceramics with bentonite, higher peaks being observed for 5 % of bentonite. The peaks occur at different frequencies of the electric voltage. The last two mentioned spectra show slight imperfections in the curve continuity. As they are observed at different frequencies, the spectrum imperfections are not attributed to a measuring instrument effect. Resonance or damping effects, which depend on the excitation signal frequency, may have caused the mentioned irregularities of the spectra. However, the presence of another local peak cannot be foreclosed, another relaxation time may also be assumed.

Table. 7.1. Model parameter values for the loss factor spectrum of ceramics specimen with admixture. Model type: 1. Here, ε_∞ denotes the optical permittivity, ε_S, the static permittivity.

No.	approx. spectrum	parameter	Material				unit	Note:
			Admixtured ceramics					
			bent. 5 %	bent. 10 %	phosph. acid	water glass		
1	tg $\delta(f)$	ε_∞	6.1	6.7	4.9	6.5	-	**model 1**
2		ε_S	361	272	73	58	-	
3		τ	0.003	0.007	0.092	0.5	s	
4		α	0.206	0.25	0.369	0.433	-	
5		r	0.9979	0.999	0.9977	0.992	-	

The optical permittivity values obtained from ceramics specimens containing 5 % of bentonite and 10 % of bentonite do not correspond to the relative permittivity values obtained from our preliminary measurements. For a 5 % admixture of bentonite, the relative permittivity was 20 at 100 Hz, for 10 % of bentonite, the same quantity featured a value of 15 at 100 Hz. If phosphoric acid was added, the relative permittivity equalled 5, for a water-glass-admixtured ceramics, the value dropped to 4. In these cases, the optical permittivity values are closer to the preliminary values than in the case of bentonite-admixtured ceramics. This may be connected with the presence of a peak in the loss factor spectrum of bentonite-admixtured ceramics.

Now, we are going to apply the type 2 model to the same experimental data set.

The model spectrum of Fig. 7.7 is decreasing more abruptly at the lowest frequencies than in the case of model 1 spectrum. The match is not ideal in this region. However, it has been retained, for the sake of a better fit in the higher frequency region. A slight rectification of the curve is apparent at higher frequencies, however, it is not perceptible in the coordinate system used. Our selection of the specimen characterization method starting as low as 40 Hz proved to be suitable and advantageous. In this way, errors in the spectrum shape can be easily eliminated, particularly in the region of maximum values of the imaginary component of the complex relative permittivity.

Based on a different model, we have obtained almost identical values of the optical permittivity, namely, from the loss factor spectrum. The γ parameter is almost identical for bentonite-admixtured ceramic specimens. The correlation coefficient values are distinctly lower than in the cases mentioned before for most of our best-fit approximations.

Table 7.2. Model parameter values for ceramics specimen loss factor spectrum. Model type. 2. Here, ε∞ denotes the optical permittivity, εs, the static permittivity.

No.	approx. spectrum	Parameter	Material				unit	Note:
			Admixtured ceramics					
			bent. 5 %	bent. 10 %	phosphor acid	water glass		
1	tg *δ*(*f*)	ε_∞	6	6.5	5	6.4	-	**model 2**
2		ε_s	286	152	250	27	-	
3		τ	0.003	0.004	1.11	0.1	s	
4		γ	0.757	0.765	0.586	0.589	-	
5		r	0.9983	0.9941	0.9971	0.9921	-	

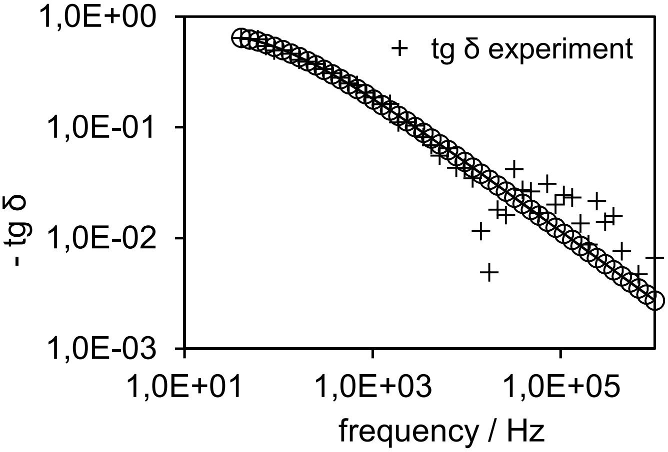

Fig. 7.8. Loss factor versus frequency plot for a phosphoric-acid-admixtured ceramics. Model type: 3. Together with a model curve. Both axis values are plotted in logarithmic coordinates.

Finally, let us present the 3rd model based modelling. As an example, we take the loss factor spectrum for a specimen of ceramics with a phosphoric acid admixture.

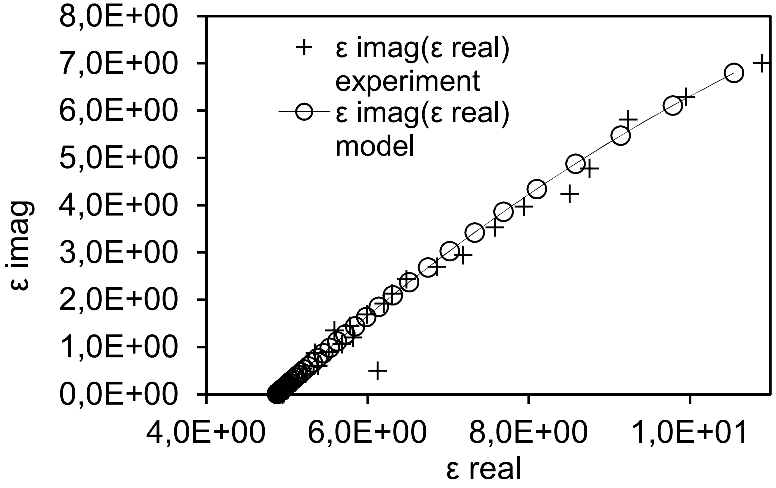

Fig. 7.9. Measured and model plots of the complex permittivity imaginary component versus the complex permittivity real component. Phosphoric-acid-admixtured ceramics. Model type: 3, based on the loss factor spectrum shape best fit.

Fig. 7.8 illustrates the measured value spread on the loss factor curve for a phosphoric acid admixtured ceramics at the lowest loss factor values. Logarithmic scale coordinate axes. The spread takes place at higher frequencies.

The complex relative permittivity imaginary component versus real component diagram is substantially rectified in comparison with the same diagram of bentonite-admixtured ceramic (not shown here). Measured values are slightly scattered around the model curve throughout the spectrum. The complex permittivity component values do not exceed 10. The first estimate of the optical permittivity can be found based on the position of the curve virtual intersection with the real component axis.

Table 7.3. Model parameter values for ceramics specimen loss factor spectrum and complex permittivity value spectrum for ceramics specimens. Model type: 3. Here, ε_∞ denotes the optical permittivity, ε_S, the static permittivity.

No.	Approx. spectrum	Parameter	material				unit	Note:
			Admixtured ceramics					
			bent. 5 %	bent. 10 %	phosph acid	water glass		
1	tg $\delta(f)$	ε_∞	6.1	6.7	4.9	6.3	-	**model 3**
2		ε_S	320	215	36	19	-	
3		τ	0.003	0.007	0.029	0.036	s	
4		α	0.148	0.126	0.096	0.16	-	
5		β	0.928	0.809	0.693	0.65	-	
6		r	0.9986	0.9989	0.9976	0.988	-	
7	Real $\varepsilon(f)$	ε_∞	6.2	6	4.9	6.5	-	
8		ε_S	313	208	49	45	-	
9		τ	0.003	0.006	0.04	0.069	s	
10		α	0.161	0.12	0.252	0.124	-	
11		β	0.969	0.86	0.857	0.829	-	
12		r	0.9996	0.9991	0.9941	0.9813	-	

The optical permittivity values feature the same magnitudes as those of the previously mentioned models, whereas the static permittivity values are different. The most probable relaxation times, as resulting from our measurements, are substantially different, first of all, for no-bentonite ceramics specimens.

The α parameter nears 0.1 for all ceramics specimens, giving evidence of a rather higher width of the relaxation time distribution curve. The lower value pertaining to phosphoric-acid-admixtures ceramics specimens is in a good agreement with our expectations, taking into account the loss factor versus frequency plot shape. The same parameter value, as measured on water-glass-admixtured specimens, is slightly higher than for the other specimens, which would mean a construction of the relaxation time spectrum. Such a conjecture cannot be ruled out, in view of the probable position of the loss factor peak deep in the low-frequency region.

The β parameter tends to unity for a 5 %-bentonite ceramics. For the remaining specimens, this parameter has lower but still relatively high values. This would support the hypothesis of a high symmetry of the relaxation time distribution. The values of this parameter, as determined from the loss factor spectrum, are in a good agreement with the values, which have been determined from the complex relative permittivity real component curves.

Application of model No. 3 to the complex relative permittivity imaginary component versus frequency has not resulted in any satisfactory agreement with the experiment. No realistic physical results have been obtained in the case of 10 %-bentonite ceramics.

7.5. Conclusions

Non-destructive testing (NDT) of construction materials by means of electric methods is a rarely used technique. For alternating electric fields, a method consisting in impedance measurements at different exciting frequencies was successfully used. The impedance spectroscopy is not applicable to materials featuring a high electric resistance, due to the part dimensions and slit formation impracticability.

Being characterized by the impedance spectroscopy method, the specimens featured differences in the loss factor spectra which appeared to depend on the frequency. Thanks to the application of three model types of the dielectric, we managed to get the values of ε_s, ε_∞, α, β, γ, τ parameters. The regression coefficient reached a maximum value for model No. 1, being followed by model No. 3. The lowest value was shown by model No. 2.

The model of the dielectric proved to be best suited for bentonite-admixtured ceramic bodies' characteristics.

Acknowledgment

This paper has been worked out under the project GAČR No. 16-02261S and project LO1408 "AdMaS UP - Advanced Materials, Structures and Technologies", supported by Ministry of Education, Youth and Sports under the „National Sustainability Programme I".

References

Barsoukov E., MacDonald J. R., *Impedance spectroscopy: theory, experiment, and applications*. 2nd ed. /. Hoboken, N.J.: Wiley-Interscience, 2005, xvii, 595 p.

Kocman V. *Fyzika a technologie elektrotechnických materiálů - Izolanty A.* Praha: SNTL - Nakladatelství technické literatury, 1971, 526 p.

Kusak I., Lunak M., Schauer P. *Tracing of Concrete Hydration by Means of Impedance Spectroscopy (New Tool for Building Elements Testing*), Applied Mechanics and Materials, 2013, vol. 248, pp. 370-378.

MacDonald J. R., *Impedance spectroscopy, emphasizing solid materials and systems*, Bibliography, Canada 1987, 346 p.

Mentlik V., *Dielektrické prvky a systémy, BEN* – technická literatura, Praha 2006, 240 p.

Palai-Dany T., Dielektrická spektroskopie karboxymetylcelulózy v časové oblasti. *Brno: Vysoké učení technické v Brně, Fakulta elektrotechniky a komunikačních technologií*, 140 s. Vedoucí disertační práce Doc. Ing. Karel Liedermann, CSc, 2009,.

Szántó L, *Maxwellovy rovnice a jejich názorné odvození*. BEN – technická literatura, Plzeň, 112 p, 2003.

Tupy M., Sotiriadis K., Kusak I., Lunak M., Stefkova D., Petranek V., *Exposure of Mortars Modified with Rubber Aggregates and Polymer Admixtures to Acid Environments and Elevated Temperature Conditions,* Journal of Materials in Civil Engineering, American Society of Civil Engineers (ASCE), United States, 2015, vol. 28, pp. 91-99.

8. Simulation quality of the probability of the reinforced concrete corrosion initiation evaluation

Tuan Le Duc[1,2], **Petr Konečný**[2]
[1] *Faculty of Civil Engineering, Saigon Technology University, 180 Cao Lo Str., Ward 4, Dist. 8, HCMC 700000, Vietnam*
[2] *VSB – Technical University of Ostrava, Faculty of Civil Engineering, Department of Structural Mechanics, L. Podeste 1875, 708 33 Ostrava-Poruba, Czech Republic*

8.1. Introduction

Steel reinforced concrete (RC) is widely used in building structures while it is rather vulnerable to harsh environment such as chloride exposure. Therefore, durability of RC structures during their service lifetime needs to be controlled to ensure proper function and performance. As a result, special attention should be paid during the durability design of RC structures in chloride environment. Many researchers focussed on the development of durability design of RC structures in recent decades (see e.g. Collepardi et al., 1972, Stewart & Rosowsky, 1998, Weyers et al., 1998, Hooton et al., 2001, Marsavina et al., 2009, Szweda&Zybura, 2013, Bentz et al. 2013, Tang S.W. et al., 2015). Since the concrete is heterogeneous material and also the other parameters governing the durability of reinforced concrete structures shows high variability, the probabilistic approach gained wider support in recent years (Keršner et al., 1996, Tikalsky, et al., 2005, Konečný, et al., 2007, Vořechovská et al., 2009, Konečný et al., 2011, Teplý & Vořechovská, 2012, Ghosh et al., 2017). Thus, probability-based design method has been a clear trend due to its ability to capture the effects of random interaction of interrelated phenomena in comparison with deterministic method.

The Monte Carlo type technique is often applied for the evaluation of probability of limit state exceedance. Such analysis with simple Monte Carlo simulation might require very large computational effort in comparison with more efficient procedures such as stratified simulation techniques and advanced simulation techniques (McKay et al., 1979, Melchers, 1989, Novák et al., 1998). The efficiency of these methods has been proved in case of low probability events. However, the issue of question herein is efficiency of the enhanced procedures in the evaluation of probability of time-dependent events such as durability related to corrosion initiation. To answer this question, a comparative assessment of durability analysis of illustrative ideal RC bridge deck without cracks with three different simulation techniques of Monte Carlo type is carried out: the simple simulation Monte Carlo, a stratified simulation technique, Latin Hypercube Sampling (McKay et al., 1979, Novak et. al, 1998) and an advanced simulation technique, Importance Sampling (Melchers, 1989). Results obtained from the assessment are analyzed on the basic of convergence and sensitivity analysis.

8.2. Methodology

Since the concrete chloride induced corrosion that involves parameters of high natural variation, the probabilistic assessment is applied in order to evaluate the risk of corrosion initiation, and the SBRA Marek et al. (2003) is used.

The penetration rate of chloride into concrete is generally modeled as a function of depth and time by using Fick's Second Law of Diffusion:

$$\frac{\partial C(x,t)}{\partial t} = D_c \frac{\partial^2 C(x,t)}{\partial x^2}, \tag{8.1}$$

where:

$C(x,t)$ – the chloride ion concentration at a distance x from the surface of concrete in time t

D_c – effective diffusion coefficient, which characterizes the concrete ability to withstand the penetration of chlorides

Solution for the differential equation (8.1) with boundary conditions (Collepardi, et al., 1972) can be expressed as:

$$C(x,t) = C_0\left\{1 - erf\left(\frac{x}{\sqrt{4.D_c.t}}\right)\right\} \qquad ,(8.2)$$

where:

C_0 – chloride concentration on the exposed surface of concrete (%)

erf – error function

Chloride threshold is the concentration of chlorides at the reinforcement level with sufficient content to initiate the corrosion. It is calculated by percentage of chloride per mass of cementitious material.

Equation (8.2) is widely used for 1D analysis without taking into account of a combined transport of water and chloride ion and influence of a crack (Tikalsky, et al., 2005). Its numerical solution is represented by the following polynomial:

$$C(x,t) = C_0\left\{1 - \frac{2}{\sqrt{\pi}}\sum_{n=0}^{14}\frac{(-1)^n\left(\frac{x}{\sqrt{4D_c t}}\right)^{2n+1}}{n!(2n+1)}\right\} \tag{8.3}$$

with n is the number of members of a polynomial.

For chloride induced corrosion, the limit state equation can be written as:

$$RF_t = C_{th} - C(x,t), \tag{8.4}$$

where:

RF_t – reliability function
C_{th} – chloride threshold

The input parameters may be described as single value or treated as random variable parameters in order to address random character of the studied problem. The probabilistic approach is adopted herein with the help of three Monte Carlo-based methods described below:

Monte Carlo method is based on a process of repeated random sampling to obtain numerical results. Its methodology includes: creating the sample, running the model and analyzing the data. It is worth noticing that the main advantages of Monte Carlo approach are: (i) simplicity of numerical implementation for complex cases; (ii) reliability and accurateness. Its drawback, however, is computation burden related with complex problems and large number of samples.

To compensate for above mentioned disadvantage of simple Monte Carlo (MC) method, a variance reduction technique such as Latin Hypercube Sampling (LHS) is necessary to have reasonable results within reasonable time. This is a special type of MC simulation approach, using the stratification of the theoretical probability distribution function of input random variables (McKay M.D. et al. 1979). The space of each random variable is divided into subsets of equal probability and outcome is generated from those subsets (Novak D. et al. 1998). Using this stratified simulation technique, reliability analysis is just repeated through sufficient repetitions lower than those of the simple MC. Simulations of random variable inputs are carried out systematically through the distribution function and are randomly mixed to secure their random interaction. This technique has better estimates of reliability function statistical parameters. Thus, expressing reliability level in the form of index β is suitable. Also the Cornell probability of failure may be computed from the standard normal distribution with the mean value and the standard deviation.

Importance Sampling (IS) is another type of advanced simulation techniques, focusing in the failure region and hence obtaining faster convergence to the true probability of failure (Melchers R.E. 1989). In this advanced technique, simulations of random variable inputs are carried out randomly and proportional to the suitable distribution function Y_i^* and the reliability level is described as:

$$p_f \approx \frac{1}{N}\sum_{i=1}^{N} g(Y_i^*) \prod_{j=1}^{k} m_{i,j}\left(X_{i,j}^*\right), \tag{8.5}$$

where:

N – number of simulations

k – number of variables

$g(Y_i^*)$ – reliability margin value based on suitable distribution Y_i^*

$m_{i,j}(X_{i,j}^*) = \frac{X_{i,j}}{X_{i,j}^*}$ – ratio between original probability of $X_{i,j}$ occurrence and occurrence from suitable distribution $X_{i,j}^*$

The initiation of corrosion due to chloride penetration is considered as a serviceability limit state (SLS) and it does not immediately results in extreme consequences to the structure. It’s necessary that designed reliability well matches with the actual performance of structure throughout the expected service life. Therefore, the computed probability of corrosion initiation will be compared with target probability. A failure probability of 10^{-1} for SLS are recommended (fib, 2006). For a life-span of 50 years, target probability of corrosion initiation of 25% is proposed (Tikalsky 2003) and adopted in (Konečný, 2007).

To make a comparative assessment of durability analysis as targeted, simulations were carried out with three different simulation techniques: simple MC, LHS and IS with number of samples (N) up to 100.000 for each in selected points of time: 10 years, 20 years, 30 years, 40 years and 50 years. The process is repeated 30 times in order to address the variability of evaluated probability of failure itself. The resulting probability is expressed with mean value and expected range (mean ± 3×standard deviation). Thus, if normal distribution is considered for the description of variability of probability of failure estimation then 99.73 % of resulting probabilities shall be found within expected range.

8.3. Typical durability analysis

The input parameters for the sample simulation of durability analysis are given in Table 8.1. Results from simple MC technique in the case of N=10.000 and t=10 years are shown in Fig. 8.1. The figure contains histograms of chloride concentration at reinforcement level, chloride threshold and reliability function. Also 2D scatter of concentration at reinforcement level and chloride threshold are available on the Fig. 8.1.

Table 8.1. Input data for probability analysis

Parameters	Range/Value	Probability density function	Reference documents
Surface chloride content, C_0 (% weight of cement)	0.21 – 1.63	Histogram	Weyers, et al., 1998
Reinforcement depth, x (m)	0.04 – 0.11	Histogram	Sohanghpurwala and Scannell, 1994
Effective diffusion coefficient, D_c ($m^2/s*10^{-12}$)	0 - 25	Histogram	Sohanghpurwala and Scannell, 1994
Critical chloride content, C_{th} (% weight of cement)	0.09 – 0.51	Histogram	Darwin et al., 2009

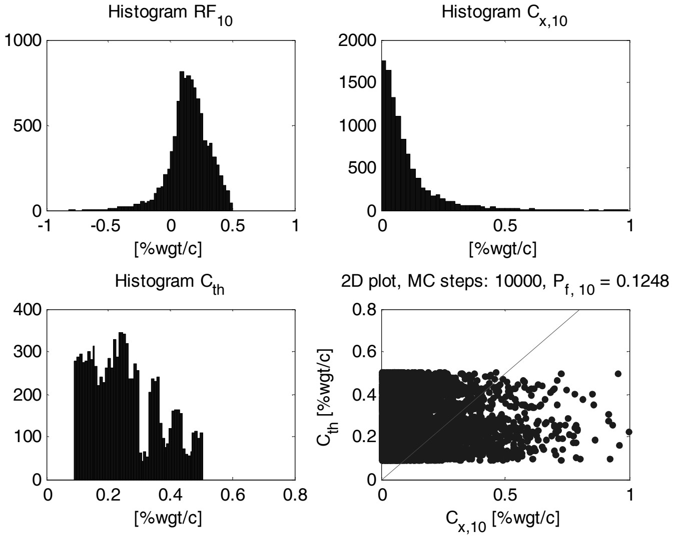

Fig. 8.1. Results from one sample simulation with simple MC technique

And Fig. 8.2 presents probability of corrosion initiation for one simple MC simulation with N=10.000 and chloride exposure time up to 50 years.

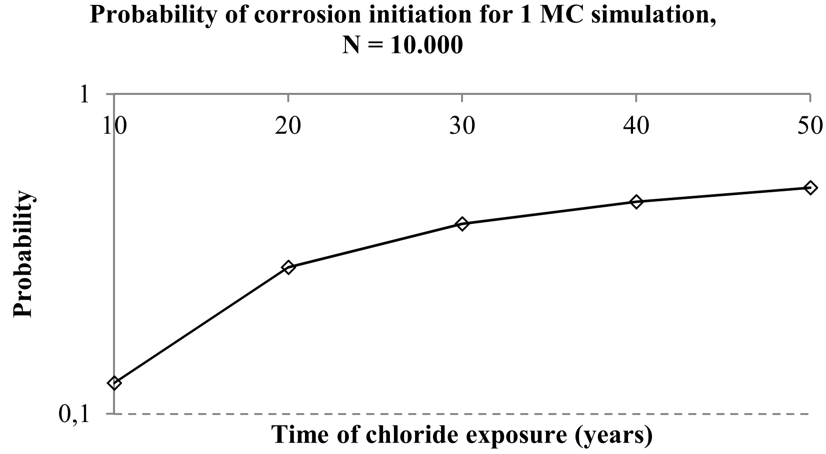

Fig. 8.2. Probability of corrosion initiation for one simple MC technique during simulated life span.

8.4. Numerical experiments

If the MC simulation with 10.000 steps is repeated 30 times then the statistics of probability of corrosion initiation for selected time are computed (mean, standard deviation). The process is also repeated for thousand and hundred thousand simulation steps. Thus, the effect of number of simulations on the probability of corrosion initiation is studied and clearly shown in Fig. 8.3, Fig. 8.4 and Fig. 8.5.

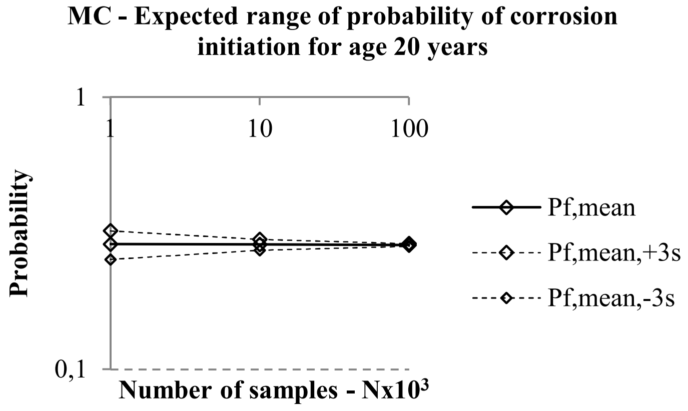

Fig. 8.3. The influence of number of simulations to the probability of corrosion initiation with simple MC technique at time 20 years

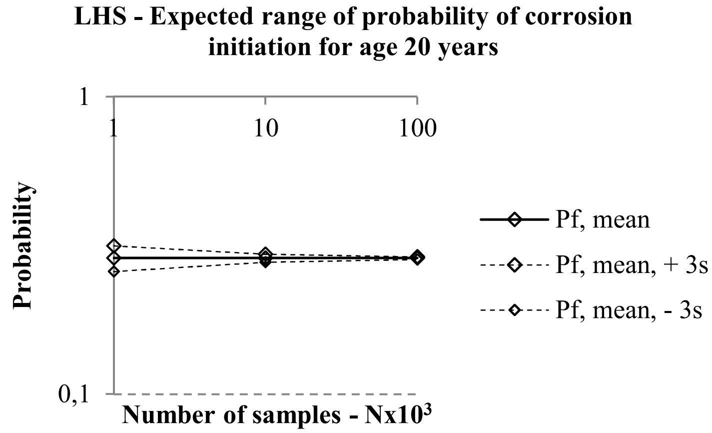

Fig. 8.4. The influence of number of simulations to the probability of corrosion initiation with LHS technique at time 20 years

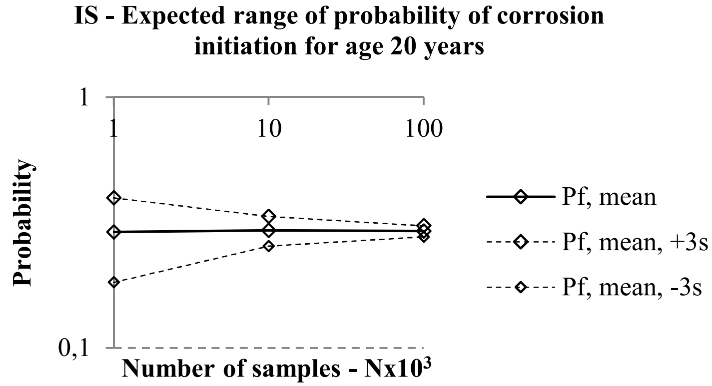

Fig. 8.5. The influence of number of simulations to the probability of corrosion initiation with IS technique at time 20 years

In addition, it is important to note that durability of RC structures vary significantly over the passage of time. The studied RC slab is not an exception. This variation is sure to make the durability of the slab reduce over the time and then its functional performance. In contrast, the probability of corrosion initiation increases with time. Therefore, the variation over the time of the probability of corrosion initiation is also studied here for all three simulation techniques (MC, LHS and IS) and typically described in Fig. 8.6, Fig. 8.7 and Fig. 8.8, respectively.

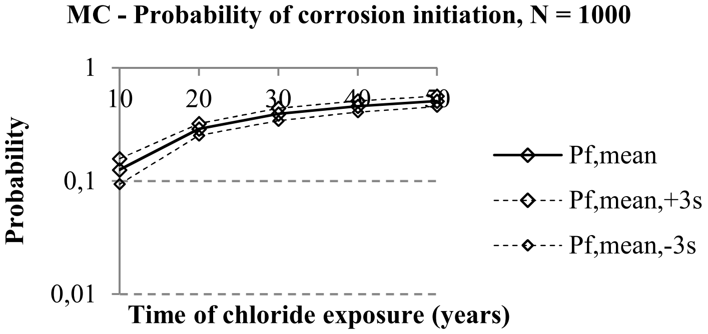

Fig. 8.6. The variation over the time of the probability of corrosion initiation with simple MC technique and N=1000

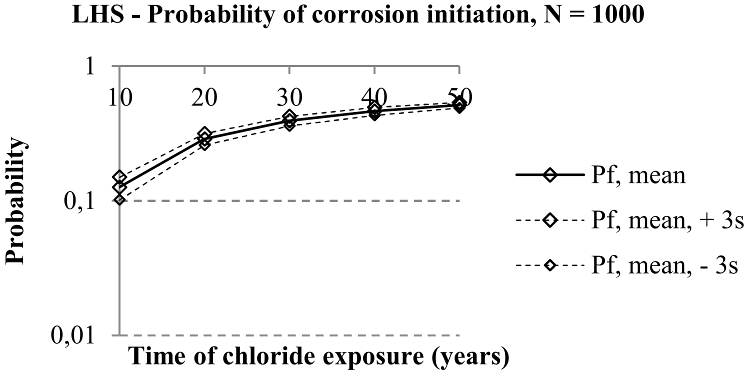

Fig. 8.7. The variation over the time of the probability of corrosion initiation with LHS technique and N=1000

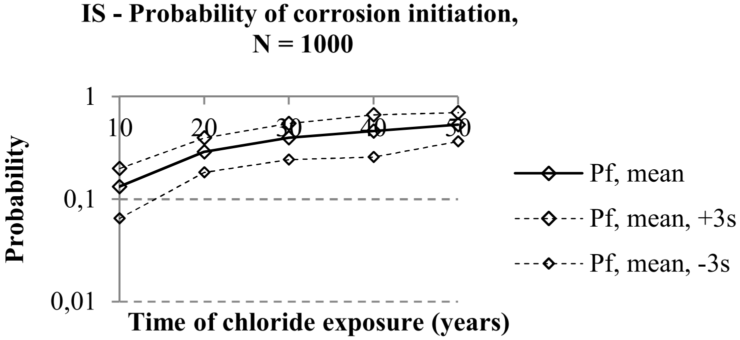

Fig. 8.8. The variation over the time of the probability of corrosion initiation with IS technique and N=1000

8.5. Results

Total of 1350 simulations for mentioned ideal RC slab using three different techniques were done. Results from all three simulation techniques are combined and compared to have a clear assessment of the durability of the slab under chloride penetration. The assessment is carried out through two main parameters: the probability of corrosion initiation and coefficient of variation of the probability of corrosion initiation. The probability of corrosion initiation and its confidence bound for each value of time are depicted in Fig. 8.9, Fig. 8.10, Fig. 8.11, Fig. 8.12 and Fig. 8.13. The coefficient of variation of the predicted probability of corrosion initiation for each value of time is presented in Fig. 8.14, Fig. 8.15, Fig. 8.16, Fig. 8.17 and Fig. 8.18.

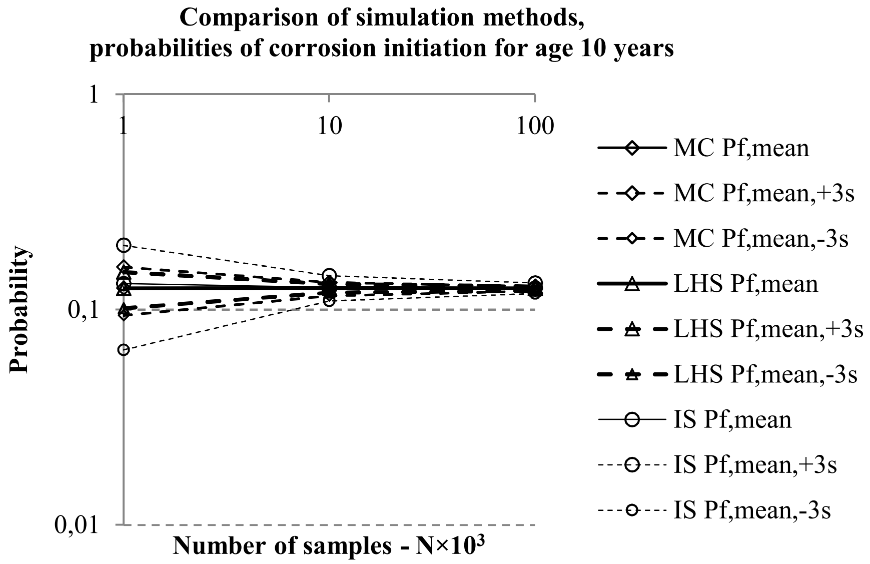

Fig. 8.9. Estimated probability of corrosion initiation at time 10 years

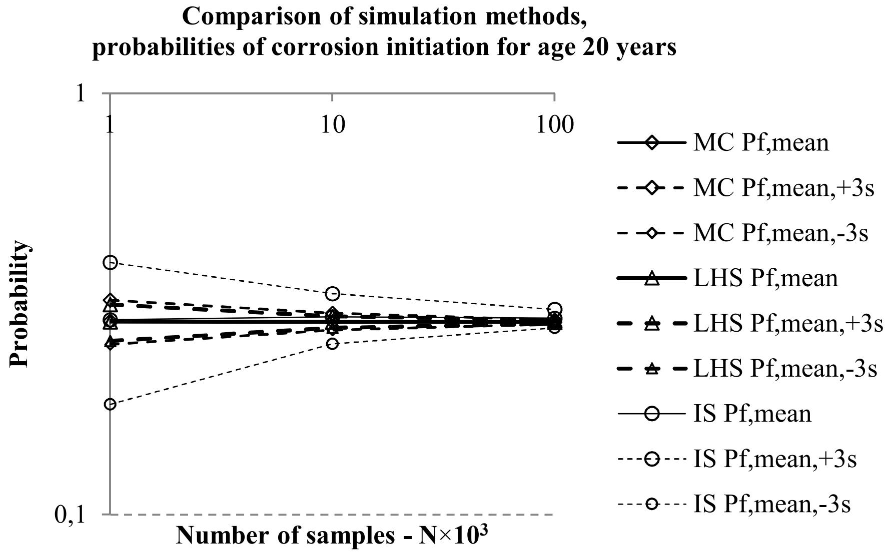

Fig. 8.10. Estimated probability of corrosion initiation at time 20 years

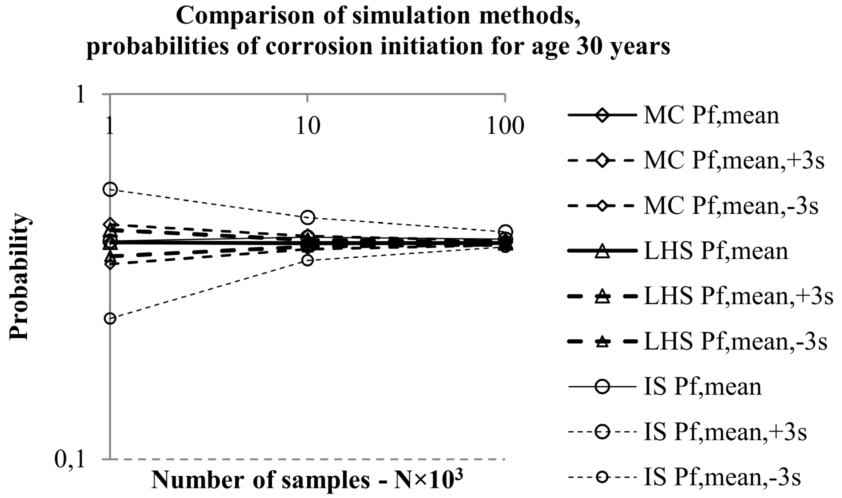

Fig. 8.11. Estimated probability of corrosion initiation at time 30 years

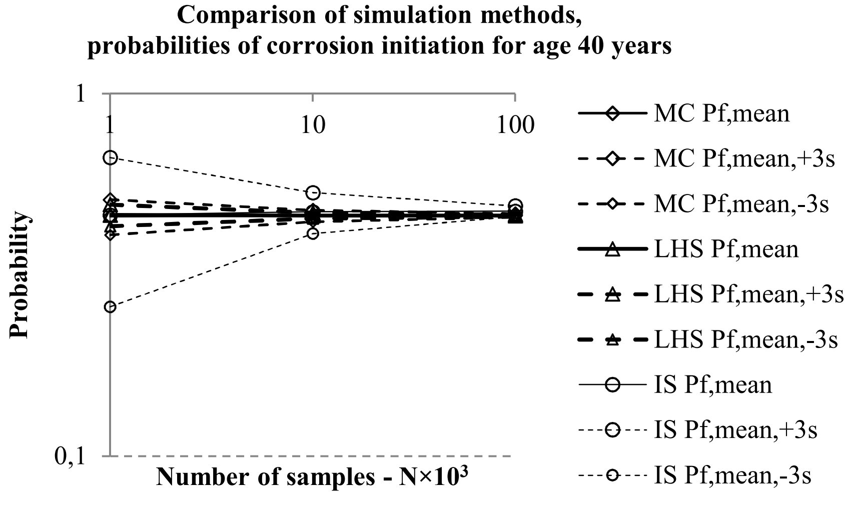

Fig. 8.12. Estimated probability of corrosion initiation at time 40 years

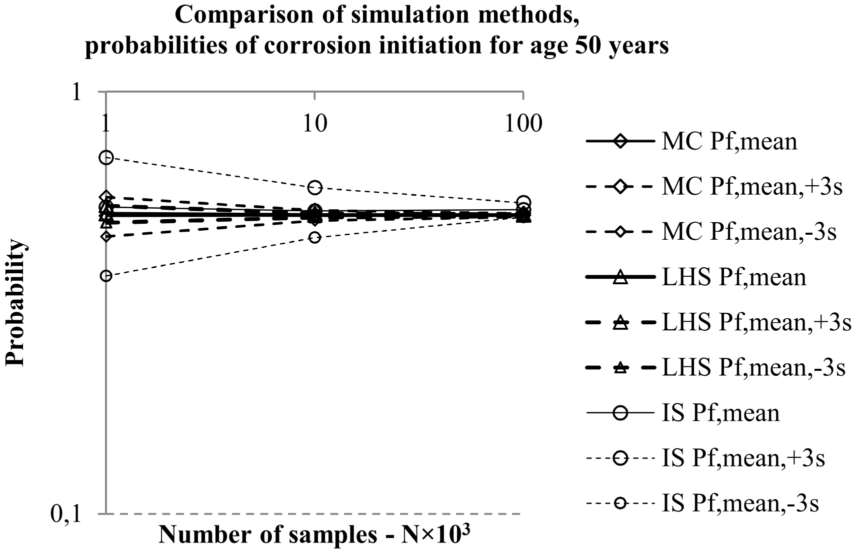

Fig. 8.13. Estimated probability of corrosion initiation at time 50 years

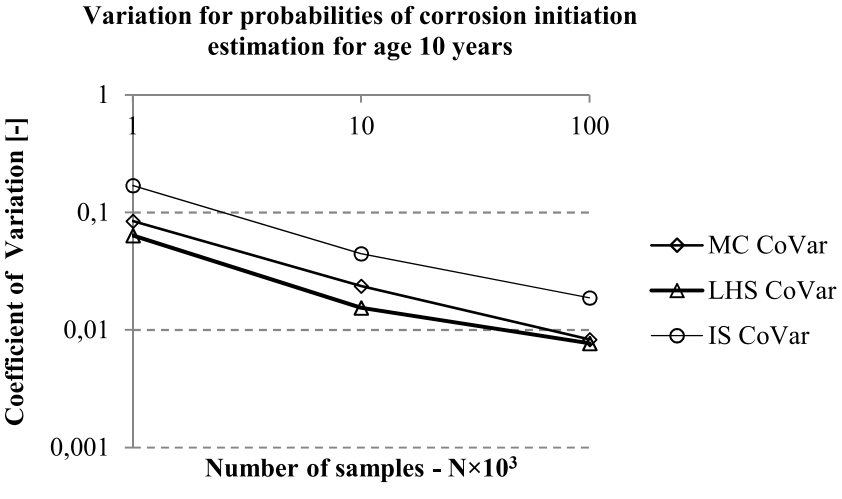

Fig. 8.14. Variation of estimated probability of corrosion initiation at time 10 years

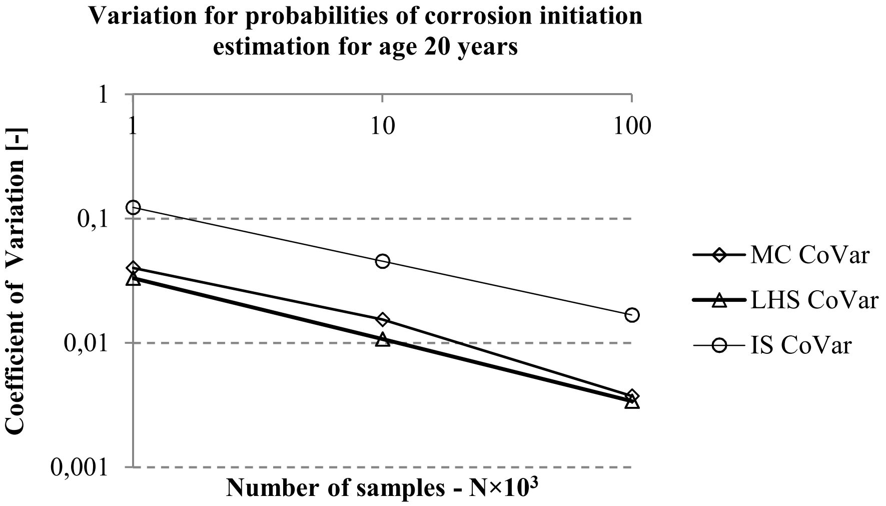

Fig. 8.15. Variation of estimated probability of corrosion initiation at time 20 years

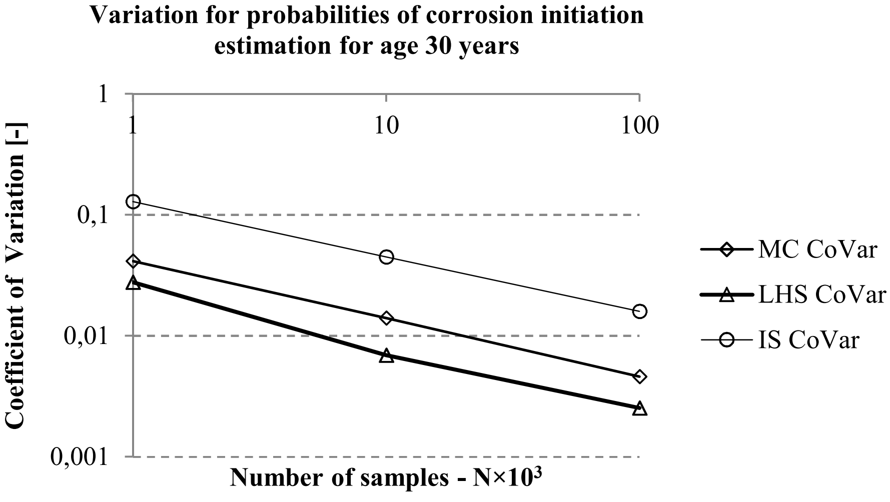

Fig. 8.16. Variation of estimated probability of corrosion initiation at time 30 years

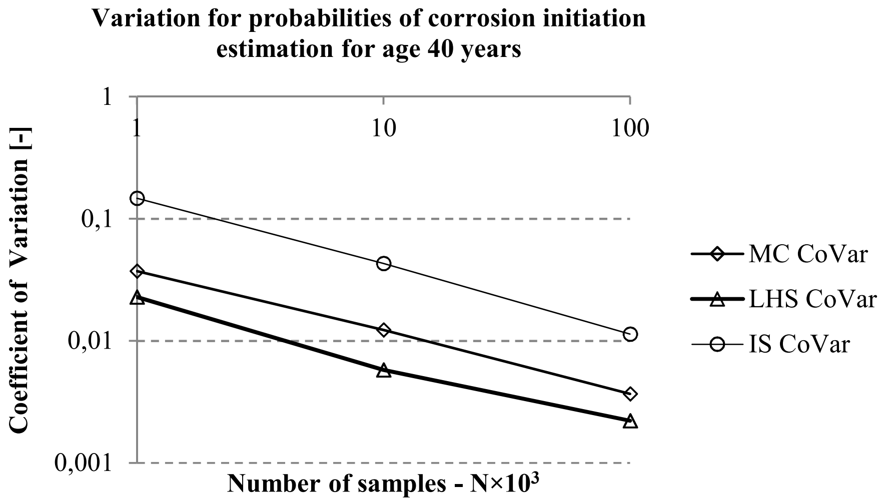

Fig. 8.17. Variation of estimated probability of corrosion initiation at time 40 years

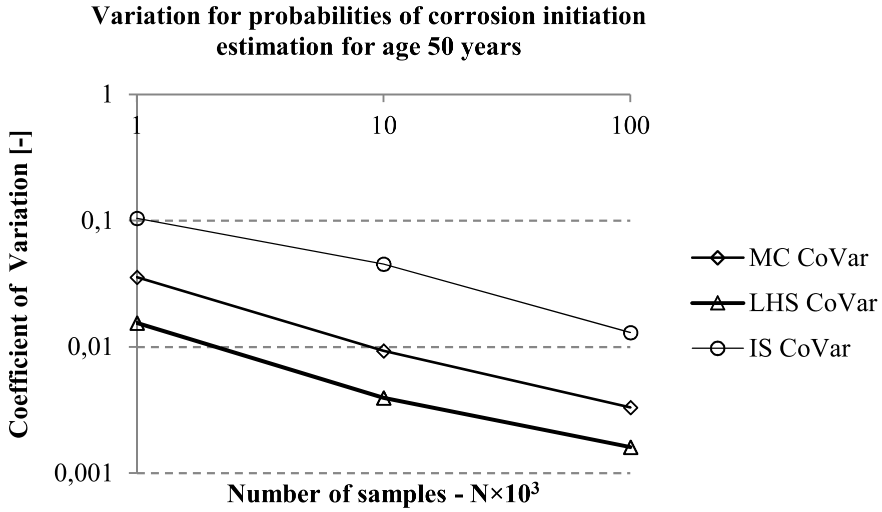

Fig. 8.18. Variation of estimated probability of corrosion initiation at time 50 years

8.6. Summary and conclusions

The probability-based durability assessment of a RC ideal slab with respect to ingress of chloride was carried out through using the scheme of SBRA in which three different MC simulation based techniques were applied, including simple MC, LHS and IS. Random input parameters were introduced via bounded histograms. Fick's Second Law of Diffusion was implemented to model the penetration rate of chloride into concrete. A limit state equation was used to describe chloride induced corrosion. Durability analysis was done by numerical experiment with a total 1350 simulations. Age of the slab and number of simulation samples were the two main parameters of this study.

The values of probability of corrosion initiation resulted from three simulation techniques are very close together on which those of from simple MC and LHS techniques are almost the same while results from IS technique are more scattered, especially with N=1000.

Estimated probability of corrosion initiation at age 10 years is around 12.5% in case of simple MC and LHS techniques while that of IS technique is 12.7%. All these values are larger than the targeted probability, 10%, as recommended by Lausanne for SLS. Furthermore, at the age of 50 years, predicted probability of corrosion initiation is about 51% with simple MC and LHS techniques and approximately 52.3% with IS technique, doubled than the target probability of 25% proposed by Tikalsky.

It's also remarkable from the results that probability of corrosion initiation rapidly converged as number of simulation samples increase and this is true for all three simulation techniques.

In all 5 considered points of time (10 years, 20 years, 30 years, 40 years and 50 years), variation of probability of corrosion initiation is ranging circa from 0.1 to 0.01 and is similar in case of simple MC and LHS techniques. While in case of IS technique, the variation coefficient is circa 3 to 5 times higher comparing to simple MC and LHS approaches. In addition, it is substantial noted that variation rate of the probability when using IS technique sharply increase with age of the slab. The difference of results in IS technique from the other two techniques can be explained by the facts that with this simulation technique, the actual simulation does not go through actual distribution, it goes through a uniform one.

It will be valuable to continue testing with more complicated models such as 2D chloride ingress one. Also combination of durability, serviceability and safety criterion in case of RC beam, column and frame in chloride exposure will be of special interest.

Acknowledgement

Financial support from VŠB-Technical University of Ostrava by means of the Czech Ministry of Education, Youth and Sports through the Institutional support for conceptual development of science, research and innovations for the year 2017 is gratefully acknowledged.

References

Bentz D.P. et al., *Modelling of the influence of transverse cracking on chloride penetration into concrete*. Cement & Concrete Composites, 2013, 38, pp. 65-74.

Collepardi M., Marcialis A., Turrizuani R., *Penetration of Chloride Ions into Cement Pastes and Concretes*, Journal of American Ceramic Research Society, V55, 1972, No. 10, pp. 534-535.

Darwin D., Browning J., O'Reilly M., Xing L., Ji J.*, Critical Chloride Corrosion Threshold for Galvanized Reinforcing Bars*, ACI Mat., J., 2009, pp. 176-183, DOI: 10.14359/56465.

Fib 2006, Model Code for Service Life Design, 2006.

Ghosh P., Konečný P., Lehnere P., Tikalsky P.J., *Probabilistic time-dependent sensitivity analysis of HPC bridge deck exposed to chlorides*, Computers and Concrete, 2017, vol. 19, issue 3, pp. 305-313.

Hooton, R.D. et al. *Prediction of Chloride Penetration in Concrete,* Federal Highway Administration, Washington, D.C., 2001, No. FHWA-RD-00-142, pp. 405.

Keršner Z., Novák D., Teplý B., Bohdanecký V., *Concrete Carbonation, Reinforcing Steel Corrosion and Cooling Tower Durability.* Sanace, (in Czech),1996, No. 4, pp. 21-23.

Konečný P., Tikalsky P.J., Tepke D.G., *Performance Evaluation of Concrete Bridge Deck Affected by Chloride Ingress: Simulation-Based Reliability Assessment and Finite Element Modeling*, Transportation Research Record, 2007, vol. 2020/2007.

Marek et al., *Probabilistic Assessment of Structures using Monte Carlo Simulation. Background, Exercises and Software*, 2nd edition, Academy of Sciences of Czech Republic, 2003.

Marsavina L. et al., *Experimental and numerical determination of the chloride penetration in cracked concrete*, Constr. Build. Mat., 2003, 2009, 23(1), pp. 264-274.

McKay M.D., Beckman R.J., Conover W.J., *A Comparison of Three Methods for Selecting Values of Input Variables in the Analysis of Output from a Computer Code*, Technometrics, 1979, 21(2): 239-245.

Melchers R.E., *Importance Sampling in Structural Systems*, *Structural Safety*, 1989, 6(1), pp.3-10.

Novak D., Teply B., Kersner Z., The role of Latin Hypercube Sampling Method in Reliability Engineering, *Structural Safety and Reliability*, 1998, 1-3, pp. 403-409.

Konečný P., Brozovsky Pratanu Ghosh P., *Evaluation of Chloride Influence on the Cracking in Reinforced Concrete using Korozeeneck Software*, Transactions of VSB – Technical University of Ostrava, 2011, No.1, 2011, Vol.XI, Civil Engineering Series, paper #6.

Sohanghpurwala and Scannell W.T., *Verification of Effectiveness of Epoxy-Coated Rebars*, Final Report to Pennsylvania Department of Transportation, Project No. *94-005,* 1994, pp. 97.

Stewart M.G., Rosowsky D.V., *Time-dependent reliability of deteriorating reinforced concrete bridge decks*. Structural Safety, 1998, 20(1), pp. 91-109.

Szweda Z. A., Zybura A., *Theoretical model and experimental tests on chloride diffusion and migration processes in concrete*. Procedia Engineering. 2013, 57, pp.1121–1130.

Tang S.W., Yao Y., Andrade C., Li Z.J., *Recent durability studies on concrete structures*, Cement and Concrete Research, 2015, 78, pp.143-154.

Teplý B., Vorechovská D., *Reinforcement corrosion: Limit states, reliability and modelling*. Journal of Advanced Concrete Technology, 2012, 10, pp. 353-362.

Tikalsky P., *Chapter 20 – Durability and Performance-Based design using SBRA in Probabilistic Assessment of Structures using Monte Carlo Simulation. Background, Exercises and Software*, 2nd edition, Academy of Sciences of Czech Republic, 2003.

Tikalsky P.J., Pustka D., Marek P., *Statistical Variations in Chloride Diffusion in Concrete,* ACI Structural Journal*,* 2005, 102(3), pp. 481-486.

Vorechovska D., Podrouzek J., Chroma M., Rovnanikova P., Teply B., *Modelling of Chloride Concentration Effect on Reinforcement Corrosion*, Computer-Aided Civil and Infrastructure Engineering, 2009, 24, pp. 446–458.

Weyers R.E., Pyc W., Springel M.M., Estimating the service life of epoxy-coated reinforcing steel, *ACI Mat.* J., 1998, pp. 546-557.

9. Multi-parameter fracture mechanics: Practical use

Lucie Malíková[1,2], Stanislav Seitl[1,2], Zbyněk Keršner[1]
[1] Brno University of Technology, Faculty of Civil Engineering, Institute of Structural Mechanics, Brno, Czech Republic
[2] Academy of Sciences of the Czech Republic, Institute of Physics of Materials, v.v.i., Brno, Czech Republic

9.1. Introduction

Classical linear elastic fracture mechanics is certainly the most common tool for assessment of fracture response/behaviour of various structures/materials. It considers the stress intensity factor (SIF) as the single parameter expressing the amplitude of the near-crack tip stress field and controlling the (un)stable crack growth. This well-known theory is derived for brittle materials and is rather sufficiently described. Nevertheless, there exist materials where the fracture process occurs not only at the crack tip (and in its very vicinity) but it takes place in a large zone of structure ahead of the crack tip. The material behaviour in this region is mostly nonlinear and is not explained and described adequately. Moreover, if the zone with nonlinear behaviour is of a large extent (comparable to the structural dimensions), the size/geometry/boundary effect cannot be omitted, see (Ayatollahi and Akbardoost 2012, Duan et al. 2007 or Karihaloo et al. 2006).

It has been shown that the so-called multi-parameter approach for approximation of the crack-tip stress and displacement fields can help to express the stress distribution better than if the only one or two parameters are used (as it is usual), see e.g. (Šestáková 2014, Veselý et al. 2014) for more details. Further investigations in this area are introduced in this paper. The Williams expansion (WE), see (Williams 1957), is used for the stress state description and subsequently also as an input for the fracture criteria enabling prediction of the crack path and estimation of the plastic zone size. It means that the criteria are used in a kind of their generalized form. This study represents a short summary of the authors' complex investigations devoted to influence of the higher-order terms of the WE on various fracture characteristics/phenomena (near-crack-tip stress field approximation, crack propagation angle, plastic zone extent, etc.), see for instance the works cited above in this paragraph or ((Šestáková) Malíková 2013a) for more details.

9.2. Theoretical background

The main idea of this paper is based on the theory derived by Williams (Williams 1957). He showed that the stress and displacement fields around the crack tip in an elastic isotropic homogeneous body subjected to an arbitrary remote loading can be expressed in a form of a series expansion, particularly as a power series. Thus, the stress tensor and displacement vector components for a cracked plate loaded in a combination of the I and II loading mode can be written as:

$$\sigma_{ij} = \sum_{n=1}^{\infty} A_n \frac{n}{2} r^{\frac{n}{2}-1}\, {}^{\sigma}f_{\mathrm{I},ij}(\theta, n) + \sum_{m=1}^{\infty} B_m \frac{m}{2} r^{\frac{m}{2}-1}\, {}^{\sigma}f_{\mathrm{II},ij}(\theta, m) \quad (9.1)$$

and

$$u_i = \sum_{n=0}^{\infty} A_n \frac{n}{2} r^{\frac{n}{2}}\, {}^{u}f_{\mathrm{I},i}\,(\theta, n, E, \nu) + \sum_{m=0}^{\infty} B_m \frac{m}{2} r^{\frac{m}{2}}\, {}^{u}f_{\mathrm{II},i}(\theta, m, E, \nu) \quad (9.2)$$

Where:

i, j – $i, j = \{x, y\}$,

r, θ – polar coordinates (assuming the origin of the coordinate system at the crack tip and the crack faces lying on the negative x-axis)

${}^{\sigma}f_{I,ij}(\theta, n)$ – known functions which can be found in various fundamental works on fracture mechanics and related papers (Williams 1957, Ayatollahi and Nejati 2011, Anderson 2004)

${}^{\sigma}f_{II.ij}(\theta, m)$ – ditto

${}^{u}f_{I.i}\,(\theta, n, E, \nu)$ – ditto

${}^{u}f_{\mathrm{II}.i}(\theta, m, E, \nu)$ – ditto

E, ν – material parameters, i.e. Young's modulus and Poisson's ratio

A_n, B_m – depend on the specimen geometry and boundary conditions; they are constant for a particular crack propagation configuration and for a particular relative crack length $\alpha = a/W$, respectively (a is the crack length and W is the specimen width).

It should be mentioned that the first (singular) term coefficients, A_1 and B_1, in Eq. 9.1 are related to the well-known mode I and mode II stress intensity factors K_I and K_II, respectively ($K_\mathrm{I} = A_1\sqrt{2\pi}$, $K_\mathrm{II} = -B_1\sqrt{2\pi}$). These parameters are dominant for $r \to 0$, which is the main idea of the conventional linear elastic fracture mechanics approach. It means that in materials where brittle fracture occurs and where the extent of the failure zone around the crack tip is negligibly small, the stress intensity factor can be used as the single-controlling parameter for failure assessment.

Coefficients of the higher-order terms (n, $m > 1$) were somewhat ignored in the past and are generally not connected to any conventional fracture parameters; except for the second term that corresponds to the in-plane T-stress. Generally, this parameter can contribute to a more accurate utilization of the fracture resistance value obtained from measurements on laboratory size specimens within the fracture response assessment of a real structure (applied mainly in the case of brittle fracture of metals, ceramics etc.). However, it has been shown that other higher-order terms can also possess an essential importance, especially if the non-linear zone extent around the crack tip is very large in relation to the structure dimensions, which occurs in elastic-plastic and quasi-brittle materials. In these cases, the higher-order terms of the WE should be taken into account for description of the stress state near the crack tip in order to describe it with sufficient precision in the entire region, where the quasi-brittle fracture response or(and) the crack-tip plasticity takes place. Thus, when more than two terms of the Williams asymptotic expansion are considered, an approach applying the so-called multi-parameter fracture mechanics is referred to.

9.3. Over-deterministic method

Numerical techniques (such as the finite element method, FEM) for estimation of the coefficients of the WE are unavoidable in most engineering tasks. Moreover, the coefficients of the third and the higher-order terms of the crack tip asymptotic field are not easy (and common) to obtain. So far, there have been only a few FE techniques introduced, enabling calculation of the coefficients of the higher-order terms. For instance, (Karihaloo and Xiao 2001) have improved and extended the hybrid crack element (HCE) introduced by (Tong et al.1997). (Su and Fok 2007) applied the fractal FE method (FFEM) together with 9-node Lagrangian hybrid elements to calculate the coefficients of the WE. Also the boundary collocation method (BCM) can be used (Xiao et al. 2004). However, all the methods mentioned above use advanced mathematical procedures and more extensive and deeper knowledge of the special elements or FE code is unavoidable. Therefore, the so-called over-deterministic approach (ODM) based on the formulation of linear least-squares is employed in this paper (well described for instance in (Ayatollahi and Nejati 2011). The main advantage of this method is that conventional finite elements can be used for the solution and only knowledge of the displacement field near the crack tip is required. Note that a more general approach of the eigenvector solution is presented in work by (Carpenter 1985).

The application of the ODM is based on Eq. 9.2, which is crucial and requires displacement field data as inputs. Thus, the evaluation procedure starts with a standard numerical simulation of a cracked specimen where a set of nodes (usually from a vicinity of the crack tip) is chosen and their coordinates and displacements are used as inputs for Eq. 9.2. In particular, two components, u and v, of the displacement vector exist in each node (in a 2-dimensional task) and therefore two equations can be written. Consequently, a system of $2k$ algebraic equations for variables A_n and B_m exists, where k represents the number of nodes selected around the crack tip for the ODM application. In order to satisfy the principle of the method (based on an over-determined system of equations), a relation between the number of nodes selected around the crack tip k and the numbers of terms of the power series considered for the stress state approximation N, M has to follow the inequality $2k > N + M + 2$.

It generally holds that the number of the higher-order terms N, M can be chosen arbitrarily, but there exist some empirical restrictions/recommendations with regard to improving the results, see for instance (Ayatollahi and Nejati 2011). The authors of the present paper have also devoted several publications to parametric studies on the ODM accuracy, convergence, or mesh sensitivity etc. (Šestáková (Malíková) 2013b).

9.4. Computational tools

Ordinary FEM. It has been mentioned above that a conventional FE analysis is sufficient for application of the over-deterministic method. Therefore, a standard finite elements model of the cracked configurations under investigation was created and analysed in Ansys FE software (ANSYS 2005). 2D 8-node iso-parametric elements with quadratic basis functions (labeled as PLANE82 in the Ansys FE system) were used for modelling of the specimen. The existence of the mid-side nodes (KSCON) in the elements used for modelling of the crack tip in the specimens is very important for the KCALC built-in procedure for evaluation of stress intensity factor value. The crack-tip singularity in the stress field is enabled to be simulated/described by means of shifting of the mid-side nodes towards the crack tip.

Mathematica software. The procedure for calculation of the Williams expansion coefficients (via ODM) was programmed in Mathematica software (Wolfram Mathematica 2007). The same code has been used for analytical reconstruction of the stress field, which resulted in the creation of contour plots of stress distribution in the cracked specimens (Veselý et al. 2014).

9.5. Fracture mechanics tasks under investigation

9.5.1. Stress field reconstruction

The values of the higher-order terms coefficients for a selected mixed-mode geometry (Angled Edge-Crack under uniaxial Tension, AECT, see Fig. 9.1) were determined for a wide range of relative crack lengths in order to obtain suitable polynomial approximations by means of fitting the data calculated. These formulas can then be used for reconstruction of the stress/displacement field for an arbitrary crack length. In Fig. 9.2 the stress fields obtained from the Williams approximation are compared with results calculated numerically for the relative crack length $\alpha = 0.8$; note that Rankine failure criterion is considered.

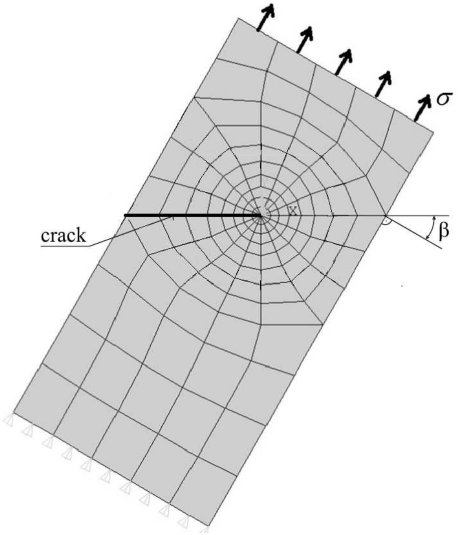

Fig. 9.1. Schema of the cracked mixed-mode geometry under investigations

It is observed that the lower stress levels and/or stress fields farther from the crack tip should be reconstructed by means of more than only one or two parameters (as it is common for brittle materials where the singular stress is dominant because the fracture occurs only in a small region very close to the crack tip). The so-called multi-parameter fracture mechanics approach presented in this work is more general and can be applied for larger range of materials with various (non-linear) fracture behaviour. Unfortunately, the sufficient number of higher-order terms necessary for accurate stress and displacement field description within a body with a crack depends on the size of the region in question and cannot be generalized.

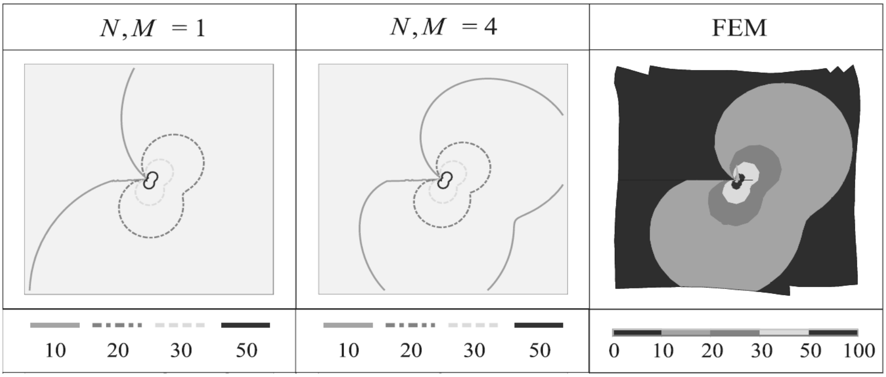

Fig. 9.2. Comparison of σ_1 principal stress field in the AECT specimen with the relative crack length $\alpha = 0.8$ reconstructed by means of the WE using various numbers of terms of the power series (1 and 4, respectively) with the numerical solution obtained directly from FEM

Note that the study performed is of larger extent, see (Malíková and Veselý 2015) for more details. It can be seen that the higher-order terms of the WE can be important. According to the study presented, the multi-parameter fracture mechanics approach is necessary especially when the stress field is influenced by the boundary conditions (short/long cracks) and/or when the stress field is investigated at larger distances from the crack tip. Accurate stress distribution is essential for further fracture analyses, such as estimation of the fracture process zone size (and its relation to other fracture effects), crack propagation direction (Shahani 2009, Ševčík et al. 2013) fracture toughness (Sahgafi et al. 2010), size effects (Ayatollahi and Akbardoost 2012, Ayatollahi and Akbardoost 2014), etc.

9.5.2. Crack path investigation

An anti-symmetrical four-point bending specimen (EA4PB), see Fig. 9.3, has been chosen for investigation of the crack propagation and the maximum tangential stress (MTS) criterion applied in order to find the kink angle γ.

The criterion was used in its well-known explicit form (Sih and Erdogan 1963 or Qian and Fatemi 1996), see Eq. 9.3, as well as in its generalized form, see Eq. 9.4, considering the $\sigma_{\theta\theta}$ approximation via WE taking into account various numbers of the initial terms of the series:

$$\gamma = 2 \arctan \frac{-2K_{\mathrm{II}}}{K_{\mathrm{I}} + \sqrt{K_{\mathrm{I}}^2 + 8K_{\mathrm{II}}^2}} \qquad (9.3)$$

$$\frac{\partial \sigma_{\theta\theta}}{\partial \theta} = 0 \quad , \quad \frac{\partial^2 \sigma_{\theta\theta}}{\partial \theta^2} < 0 \tag{9.4}$$

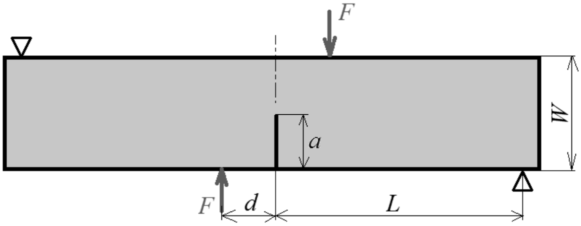

Fig. 9.3. Schema of the cracked anti-symmetrical four-point bending specimen

If the crack path through a specimen shall be estimated by means of the MTS criterion, knowledge of the tangential stress distribution is essential. In Fig. 9.4 the deformed anti-symmetrical four-point bending specimen with a propagating crack is plotted; $\sigma_{\theta\theta}$ contour lines in the most important region near the crack tip are highlighted.

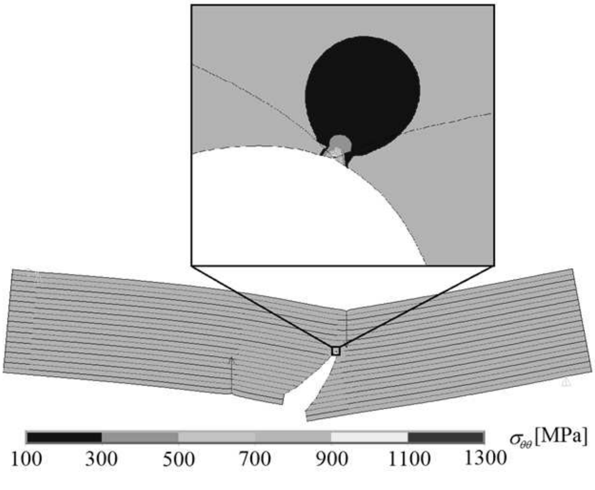

Fig. 9.4. Tangential stress contour lines in the deformed (200 times enlarged) anti-symmetrical four-point bending specimen with a propagating edge crack with its tip in a depth of 24 mm in the specimen

Several first steps of the crack path through the specimen investigated are presented in Fig. 9.5. The crack paths have been calculated by means of both the classical MTS criterion (when only the first singular term of the expansion is taking into account) and the generalized form of the MTS criterion (when the initial 2, 3, 4 or 5 terms of the WE are taking into account). Both criteria have been applied on various radii.

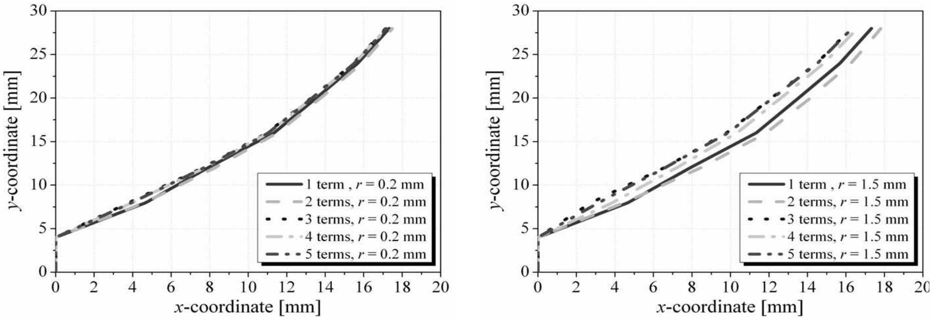

Fig. 9.5. Crack paths through the specimen calculated via generalized MTS criterion taking into account various numbers of terms of the WE and applied on the radius of 0.2 mm (left) and 1.5 mm (right) around the crack tip

In this study, see more details in ((Šestáková) Malíková 2013a), the Williams expansion derived for description of stress/displacement crack-tip fields is introduced as a tool for generalization of the classical MTS criterion used for determination of the crack propagation direction in an anti-symmetrical four-point bending specimen. The study presented shows that if the distance from the crack tip, where the criterion shall be applied, is large enough, using the multi-parameter fracture mechanics approach, i.e. the generalized MTS criterion, gives more accurate estimation of the crack path. Application of the classical MTS criterion in this case could decrease the accuracy because it predicts that the crack does not propagate so rapidly as the crack path estimation from the generalized MTS criterion shows.

9.5.3. Plastic zone extent estimation

The same mixed mode configuration as in the previous section, see Fig. 9.3, was chosen for the presented study because of its generality in comparison to specimens loaded in pure mode I or pure mode II. In this analysis, the plastic zone extent is investigated by means of the Rankine criterion for the selected EA4PB mixed-mode configuration. Particularly, the influence of the number of the WE terms considered for the stress components approximation on the plastic zone size estimation is studied. In Fig. 9.6 comparison of the plastic zone size calculated via FEM with results calculated from the same criterion by means of the WE with various numbers of the initial terms. Three different cases are simulated:

materials with the critical stress/tensile strength value $\sigma_c = 4$, 6 and 8 MPa are assumed. Note that the dimensions of the plotted area are 15.4 mm × 15.4 mm.

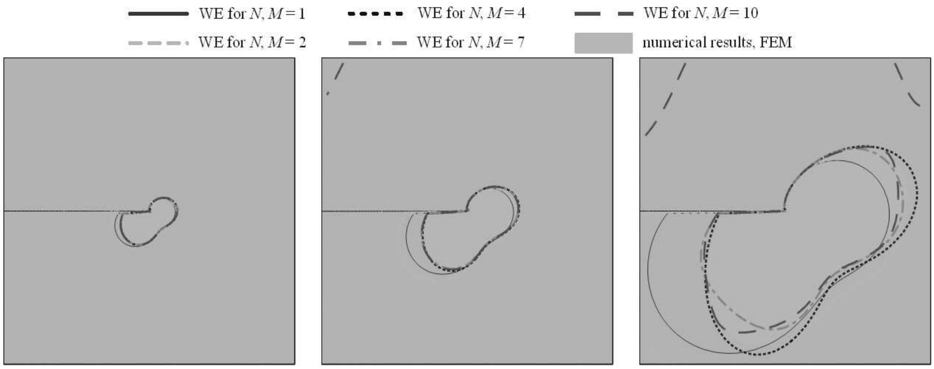

Fig. 9.6. Comparison of the plastic zone sizes calculated via FEM using Rankine criterion for the chosen EA4PB configurations with results calculated from the same criterion when the stress components are approximated via the WE with various numbers of the initial terms and considering the critical stress value: $\sigma_c = 8$ MPa (left); $\sigma_c = 6$ MPa (middle); $\sigma_c = 4$ MPa (right)

The plastic zone extent was investigated in an eccentric asymmetric four point bending specimen using the Rankine/maximum stress criterion, see more details in (Malíková and Veselý 2014). By means of varying the tensile strength of the material in the numerical model of the cracked specimen, it is shown that when the nonlinear zone extent is small enough, the classical one- or two-parameter fracture mechanics concept can be applied. On the other hand, when the stress field needs to be investigated also in larger distances from the crack tip, i.e. the plastic zone extent is comparable to the typical specimen dimensions, using the WE with more higher-order terms for the stress field approximation can be very advantageous. Then, a generalized form of the criterion is spoken about and its utilization can contribute to better description of the occurring failure process.

9.6. Conclusions

This chapter should represent a short summary of the authors' complex investigations devoted to influence of the higher-order terms of the WE on various fracture characteristics/phenomena (near-crack-tip stress field approximation, crack propagation angle, plastic zone extent, etc.). It is shown that the higher-order terms can play a significant role for some specific test configurations and can help to increase the accuracy of assessment of fracture mechanics tasks.

Acknowledgement

Financial support from the Czech Science Foundation (project No. 15-07210S 16-18702S) is gratefully acknowledged.

This work is dedicated to the memory of our wonderful colleague, Dr. Václav Veselý, who recently passed away.

References

Anderson T.L. *Fracture mechanics: Fundamentals and Applications*, CRC Press, Boca Raton, 2004.

ANSYS Program Documentation *User's manual version 10.0*. Swanson Analysis System, Inc., Houston, 2005.

Ayatollahi M.R., Akbardoost J., *Size effects on fracture toughness of quasi-brittle materials – A new approach*, Engineering Fracture Mechanics, 2012, vol. 92, pp. 89–100.

Ayatollahi M.R., Akbardoost J., *Size and geometry effects on rock fracture toughness: Mode I fracture*, Rock Mechanics and Rock Engineering, 2014, vol. 47, pp. 677–687.

Ayatollahi M.R., Nejati M., *An over-deterministic method for calculation of coefficients of crack tip asymptotic field from finite element analysis*, Fatigue & Fracture of Engineering Materials & Structures, 2011, vol. 34, pp. 159–176.

Carpenter W.C., *The eigenvector solution for a general corner of finite opening crack with further studies on the collocation procedure*, International Journal of Fracture, 1985, vol. 27, pp. 63–74.

Duan K., Hu X.Z., Wittmann F.H., *Size effect on specific fracture energy of concrete*, Engineering Fracture Mechanics, 2007, vol. 74, pp. 87–96.

Erdogan F., Sih G.C., *On the crack extension in plates under plane loading and transverse shear*, Journal of basic engineering, 1963, vol. 85(4), pp. 519–527.

Karihaloo B.L., Abdalla H.M., Xiao Q.Z., *Deterministic size effect in the strength of cracked concrete structures*, Cement and Concrete Research, 2006, vol. 36, pp. 171–188.

Karihaloo B.L., Xiao Q.Z. *Accurate determination of the coefficients of elastic crack tip asymptotic field by a hybrid crack element with p-adaptivity*, Engineering Fracture Mechanics, 2001, vol. 68, pp. 1609–1630.

Malíková L., Veselý V., *Significance of higher-order terms of the Williams expansion for plastic zone extent estimation demonstrated on a mixed-mode geometry*, Procedia Materials Science, 2014, vol. 3, pp. 1383–1388.

Malíková L., Veselý V., *The influence of higher order terms of Williams series on a more accurate description of stress fields around the crack tip*, Fatigue & Fracture of Engineering Materials & Structures, 2015, vol. 38 (1), pp. 91–103.

Qian J., Fatemi A., *Mixed mode fatigue crack growth: a literature survey*, Engineering fracture mechanics, 1996, vol. 55(6), pp. 969–990.

Saghafi H., Ayatollahi M.R., Sistaninia M., *A modified MTS criterion (MMTS) for a mixed-mode fracture toughness assesssment of brittle materials,* Materials Science and Engineering A, 2010, vol. 527, pp. 5624–5630.

Shahani A.R., Tabatabaei S.A. *Effect of T-stress on the fracture of a four point bend specimen*, Materiasl & Design, 2009, vol. 30, pp. 2630–2635.

Su R.K.L., Fok S.L., *Determination of coefficients of the crack tip asymptotic field by fractal hybrid finite elements*, Engineering Fracture Mechanics, 2007, vol. 74, pp. 1649–1664.

(Šestáková) Malíková L., *Crack path investigation using the generalized maximum tangential stress criterion: antisymmetrical four-point bending specimen*, Applied Mechanics and Materials, 2013a, vol. 436, pp. 108–113.

Šestáková (Malíková) L., *How to enhance efficiency and accuracy of the over-deterministic method used for determination of the coefficients of the higher-order terms in Williams expansion*, Applied Mechanics and Materials, 2013b, vol. 245, pp. 120–125.

Šestáková L. *Using the multi-parameter fracture mechanics for more accurate description of stress/displacement crack tip fields*, Key Engineering Materials, 2014, vol. 586, pp. 237–240.

Ševčík M., Hutař P., Náhlík L., Seitl S., *The effect of constraint level on a crack path*, Engineering Fracture Mechanics, 2013, vol. 29, pp. 83–92.

Tong P., Pian T.H.H., Lasry S.J., *A hybrid element approach to crack problems in plane elasticity*, International Journal of Numerical Methods in Engineering, 1997, vol. 7, pp. 297–308.

Veselý V., Frantík P., Sobek J., Malíková (Šestáková) L., Seitl S., *Multi-parameter crack tip stress state description for estimation of nonlinear zone width in silicate composite specimens in component splitting/bending test geometry*, Fatigue & Fracture of Engineering Materials & Structures, 2014, vol. 38 (2), pp. 200–214.

Williams M.L., *On the stress distribution at the base of stationary crack*. Journal of Applied Mechanics ASME, 1957, vol. 24, pp. 109–114.

Wolfram Mathematica Documentation Center, Wolfram Research, Inc., Champaign, 2007.

Xiao Q.Z., Karihaloo B.L., Liu X.Y., *Direct determination of SIF and higher order terms of mixed mode cracks by a hybrid crack element*, International Journal of Fracture, 2004, vol. 125, pp. 207–225.

10. Selected problems of the foundation slab under the residential building

Katarína Tvrdá[1]

[1] Slovak University of Technology, Faculty of Civil Engineering, Bratislava, Slovakia,

10.1. Introduction

Building structures always rest on the eareth´s surface, so it is necessary to analyze these structures in interaction with subsoil. The use of FEM introduced a lot of advantages to modeling of structures in interaction with the subsoil. It allows the inhomogeneous subsoil, anisotropy to be implemented into the calculation. Such a slab can be modelled in different ways. One possible way is the one-parametric – Winkler´s model of subsoil. For such a model there are various methods of calculating the soil stiffness shown in the chapter 10.2.1. The foundation slab was modeled in ANSYS software used the Shell63 element, which allows including the ground mass into the analysis. In the case of modeling of foundation slabs on elastic half-space, it is necessary to model a quite large portion of ground mass, outside the active depth of deformation. For assessing the structure, international standards and regulations, together with the National Annexes, have been used. Eurocodes also permit assessment of building structures based on probabilistic analysis. Numerous authors have been dealing with probability analyses: Haldar & Mahadevan 2000, Marek at al. 2003, Krejsa & Kralik 2015, and others.

10.2. Foundation slab in interaction with subsoil

An inseparable part of a building structure is the ground mass on which the structure is built. This massive area is infinite, however in modeling of structures in interaction with the subsoil it must have its limits. It is therefore important to choose the right mathematical and material model, which describes the background of the problem. The elastic foundation can be modeled with these types of models:

- Winkler subsoil model (One-parametric model),
- Pasternak subsoil model (Two-parametric model),
- Boussinesq model (Theory of elastic half space).

10.2.1. Winkler subsoil model

Winkler model is the first model of the subsoil, based on the hypothesis of setting coefficient (coefficient of subgrade stiffness), which assumes that at any point of the subsoil there is the load $p(x,y)$ directly proportional to deflection $w(x,y)$ in this point, but it is not dependent on the deflection at the other points. There is drawback in the instability of the setting coefficient (subgrade stiffness) k which depends not only on the material properties of the subsoil, but on the dimensions and the shape of the foundation structure as well. A slab on an elastic foundation is controlled by partial differential equation (10.1).

$$D\,\nabla^2\nabla^2\,w(x,y) + k\,w(x,y) = p(x,y) \tag{10.1}$$

Where:

D – slab constant - see eq. 10.2,
k – elastic foundation stiffness,
$p(x,y)$ – contact stress,
$w(x,y)$ – deflection.

$$D = \frac{E\,h^3}{12\,(1-\nu^2)} \tag{10.2}$$

Where:

E – modulus of elasticity of the material of slab,
h – thickness of slab,
ν – Poisson´s ratio,

Contact stress $p(x,y)$ in point can by calculated by the eq. (10.3) and is independent on the deflection at another point.

$$p(x,y) = k\,w(x,y) \tag{10.3}$$

The pressure in any spring is directly proportional to its pressing and is independent from the other springs. Despite the defect of this model, Winkler's hypothesis can be used very successfully for a material with a low shear stress.

The elastic foundation stiffness can be calculated by individual authors:

Gorbunov - Posadov $$k = \frac{2E}{\pi(1-\nu^2)}\frac{1}{R} \tag{10.4}$$

Pasternak $$k = \frac{E}{H(1-\nu^2)} \tag{10.5}$$

Vlasov-Leontiev $$k = \frac{E_{oed}}{H(1-\nu^2)} \tag{10.6}$$

Barvašová $$k = \frac{E}{H(1-\nu)} \tag{10.7}$$

Prakasm
$$k = \frac{1.13\,E}{(1-\nu^2)}\frac{1}{\sqrt{A}} \tag{10.8}$$

For a rectangle slabs ($2b < 2a$)
$$k = \frac{E}{16\,a\,(1-\nu^2)}\left[3.1\left(\frac{a}{b}\right)^{0.75} + 1.6\right] \tag{10.9}$$

Formulas see eq. (10.4) - (10.7) may be applied to soil foundation, where the relatively thin layer H lies on a hard base. For the foundations of larger planar dimensions as the foundation slabs the relations see eq. (10.8) - (10.9) are useful. In the case where the arrangement of the foundation structure s is available, the relationship see eq. (10.10) can be used to calculate
$$k = \frac{p}{s}, \tag{10.10}$$

where

p – contact stress,

s – setlement.

10.2.2. Pasternak subsoil model or two-parametric model

Two-parametric model of the subsoil is defined by Pasternak so that the contact stress p is defined according to the deflection surface of $w\ (x, y)$ and coefficients C_1 - coefficient of friction in the vertical direction (N / m^3), and C_2 - coefficient characterizing the shear spreading of the effects of the load (N / m) obtained using energy principles. This model allows to take into account deformations beyond the foundation.
$$D\,\nabla^2\nabla^2\,w(x,y) + C_1\,w(x,y) - C_2\left[\frac{\partial^2 w(x,y)}{\partial x^2} + \frac{\partial^2 w(x,y)}{\partial y^2}\right] = p(x,y) \tag{10.11}$$

10.2.3. Boussinesq model – theory of elastic half space

Elastic half-space is another type of mathematical - material model of the elastic subsoil. The theory of elastic continuous half-space implies that the background forms a continuous, homogeneous and perfectly elastic body of an infinitely large size, limited from above by the plane on which lies the underlying building structure. Sometimes it is called the Boussinesq soil model. The model is characterized by two material constants derived from experimental measurements (E - modulus of elasticity and ν - Poisson´s constant). Numerical methods are primarily used to solve contact problems (subgrade model - elastic half-space) to appropriately extend the closed form solutions while offering the possibility of more realistic capturing the interaction characteristics with the subsoil building structure for different boundary conditions. The most famous is the FEM. Theoretical assumptions of Boundary Element Method - BEM and Finite Element

Method - FEM in interaction were dealt by Zienkiewicz & Taylor 2000, Jendželovský & Baláž 2014, Sumec et al. 2010, Kotrasova & Kormanikova 2016, Klucka et al. 2014 and others.

Elastic foundation is modeled by spatial (3D) finite elements. Finite elements of different shapes can be used for the modeling. The most commonly used form are solid block elements with 8 nodes, and three displacements at each node. In modeling of elastic half-space it is necessary to create a sufficiently large volume of grown earth, which depends on supports, boundary conditions. The support may be rigid, flexible or by infinite finite elements.

For the analysis of interaction foundation sla with the subsoil (static bonds on the contact surface) two basic models can be defined: computational model of bilateral bonds - continuous model, calculation model with unilateral bonds - discrete model.

10.3. Probability analysis

To determine the reliability of probabilistic methods, first the performance criteria are defined on the basis of functional relationship between the first n input variables, called bases random variables Xi, where $i = 1, 2, ..., n$. This relationship is called a function of reliability (security, usability, feature or function, or function failure reliability reserves) and is marked as see eq. (10.12)

$$F_s = RS = g\,(X_1, X_2, \cdots, X_n). \tag{10.12}$$

A functional dependency $g\,(X_1, X_2, \cdots, X_n)$ is a computational model that is based on simplifying assumptions and represents the idealization of physical reality.

Failure functions $g\,(X_i)$ express conditions of probability (reserve) and can be represented as a function of stochastic parameters. They may be defined as a simple (e.g. for one section) or as complex structures, for more cross-sections (e.g. all finite-element model).

The reliability function can be also defined as:

$$F_s = RF = R - S \tag{10.13}$$

where:

R – is the resistance of the structure function (yield strength, allowable deflection, stress),

S – is a function of the load (max. stress in the structure, max. deflection).

The function is reliable if $F_s \geq 0$, failure occurs if $F_s < 0$ and $F_s = 0$ is the limit function.

The probability of failure can be simply defined as:

$$P_f = P[R < S] = P[R - S < 0] \tag{10.14}$$

where:

P_f – is generally given by the expression (10.15),

$$P_f = \iint \cdots \iint_{g(X)<0} f_X(X_1, X_2, \cdots, X_n)\, dX_1\, dX_2 \cdots dX_n \tag{10.15}$$

where the function $f_X(X_1, X_2, \ldots, X_n)$ represents the multiple density of probability function for continuous random variables or multiple probability function for discrete random variables, where integration is transferred over the entire area of failure $g(X) < 0$.

In deterministic calculation we entered the input parameters as the fixed constants. When we used probability calculation, the input parameters specified in the range were accidental due to inaccuracies in manufacture and the determination of material characteristics. The individual parameters varied according the diagrams.

10.3.1. Response surface analysis design

Response Surface Methods are based on the fundamental assumption that the influence of the random input variables on the random output parameters can be approximated by mathematical function. Hence, Response Surface Methods locate the sample points in the space of random input variables such that an appropriate approximation function can be found most efficiently; typically, this is a quadratic polynomial. In this case the approximation function $\hat{U}$ is described by eq. (10.13)

$$\hat{U} = c_0 + \sum_{i=1}^{NRV} c_i X_i + \sum_{i=1}^{NRV} \sum_{j=1}^{NRV} c_{ij} X_i \,.\, X_j, \tag{10.13}$$

where c_0 is the coefficient of the constant term, c_i, $i = 1,...NRV$ are the coefficients of the linear terms and c_{ij}, $i = 1,...NRV$ and $j = i, ...,NRV$ are the coefficients of the quadratic terms.

To evaluate these coefficients a regression analysis is used and the coefficients are usually evaluated such that the sum of squared differences between the true simulation results and the values of the approximation function is minimized. Hence, a response surface analysis consists of two steps:

- Performing the simulation loops to calculate the values of the random output parameters that correspond to the sample points in the space of random input variables.
- Performing a regression analysis to derive the terms and the coefficients of the approximation function.

The fundamental idea of Response Surface Methods is that once the coefficients of a suitable approximation function are found, then we can directly use the approximation function instead of looping through the finite element model. To perform a finite element analysis might require minutes to hours of computation time; in contrast, evaluating a quadratic function requires only a fraction of a second. Hence, if using the approximation function, we can afford to evaluate the approximated response parameter thousands of times. A quadratic polynomial is sufficient in many cases of engineering analysis (for example, the evaluation of the thermal stress mentioned above). For that evaluation, the Young's modulus and the thermal expansion coefficient both have a linear effect on the thermal stresses, which is taken into account in a quadratic approximation by the mixed quadratic terms. However, there are cases where a quadratic approximation is not sufficient; for example, if the finite element results are used to calculate the lifetime of a component. For this evaluation, the lifetime typically shows an exponential behavior with respect to the input parameters; thus the lifetime results cannot be directly or sufficiently described by a quadratic polynomial. But often, if you apply a logarithmic transformation to the lifetime results, then these transformed values can be approximated by a quadratic polynomial. The ANSYS PDS offers a variety of transformation functions that you can apply to the response parameters, and the logarithmic transformation function is one of them.

10.3.1.1. Central composite design sampling

A central composite design consists of a central point, the N axis point plus 2^{N-f} factorial points located at the corners of an N-dimensional hypercube. Here, N is the number of random input variables and f is the fraction of the factorial part of the central composite design. A fraction $f = 0$ is a called a full factorial design, $f = 1$ gives a half-factorial design, and so on. The PDS gradually increases the fraction f as you increase the number of random input variables. This keeps the number of simulation loops reasonable. The fraction f is automatically evaluated such that a resolution V design is always maintained. A resolution V design is a design where none of the second order terms of the approximation function are confined with each other. This ensures a reasonable accuracy for the evaluation of the coefficients of the second order terms.

The locations of the sampling points for a problem with three random input variables is illustrated below, see Fig. 10.1.

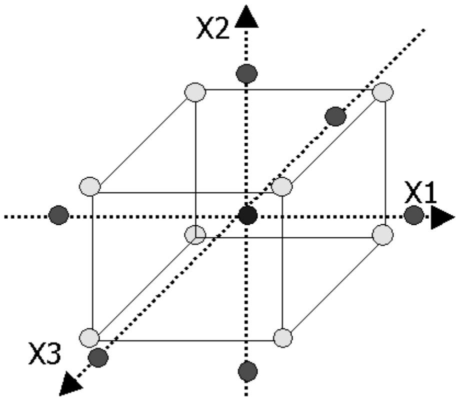

Fig. 10.1. Locations of sampling points for problem with three input variables for CCD

The number of sample points (simulation loops) required for a central composite design as a function of the number of random input variables is given in the table, see tab. 10.1.

Table. 10.1. The number of simulation loops required for a central composite design

Number of random input variables	1	2	3	4	5	6
Number of coefficients in a quadratic function (with cross-terms)	3	6	10	15	21	28
Factorial number *f*	N/A	0	0	0	1	1
Number sample points (simulation loops)	N/A	9	15	25	27	45

10.4. Analyses of the foundation slab under residential building

10.4.1. Deterministic approach

The analysed foundation slab is located under residential building. It is made of concrete of the class *C25/30* with material properties as follows: $E_x = 31\ GPa$, Poisson's ratio $v = 0.2$, size *12 x 12 m*, with thickness *0.6 m*. The foundation slab is loaded with singular forces from columns $F = 914 - 3342\ kN$ according to the loading area, see Fig.10.2.

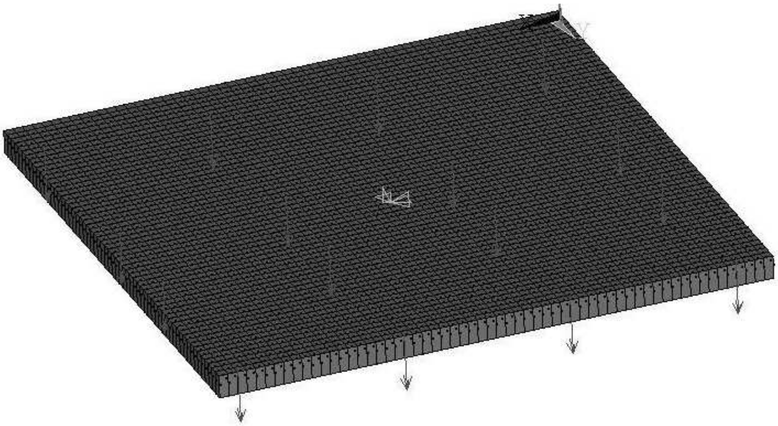

Fig. 10.2. Model of the foundation slab

The foundation slab is rested on a layered subsoil:

- *0 – 1.5 m* from the foundation gap *G5* – clayey gravel, dense
- *1.5 – 9 m* *G2* –Poorly graded gravel
- *9 – 14 m* *F8* – clay with medium plasticity.

The stiffness of the subsoil was determined as $k = 46\ 000\ kN/m^3$ according to formula (10.10). The easiest way to model a slab on en elastic foundation is to use SHELL 63 elements, where it is possible to introduce the stiffness coefficient of the subgrade via the EFS command.

Final deflection of the foundation slab rested on layered subsoil from the deterministic approach is shown in Fig. 10.3.

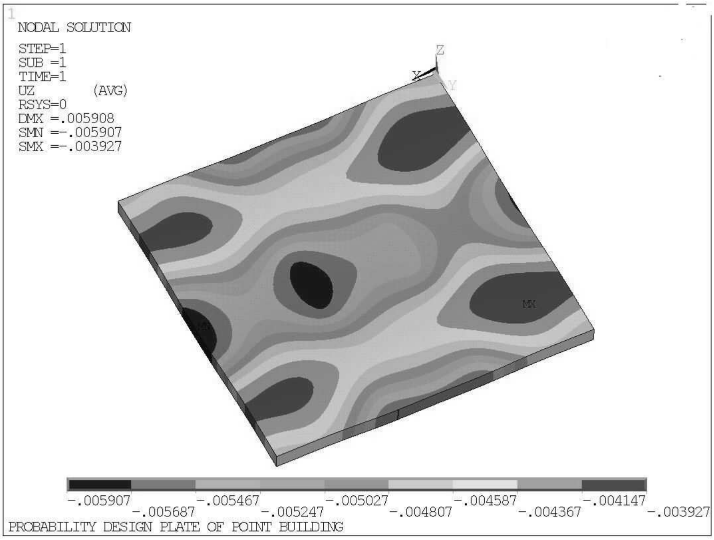

Fig. 10.3. Deflection of the foundation slab from the deterministic analysis

10.4.1. Probabilistic approach

The individual input parameters in the probabilistic analyses are varied according to Tab. 10.2. Change of geometric properties of the foundation slab was defined via thickness *H* and via a change in thickness of the foundation slab - *Hvar_*. The stiffness of the slab was determined via Young´s modulus *EX* and via variable factor *Evar_*., see Fig.10.4. Stiffness of the elastic subsoil was defined via *k* and through a variable factor *KKvar_*. The load was determined through *F* and via variable *Fvar_*.

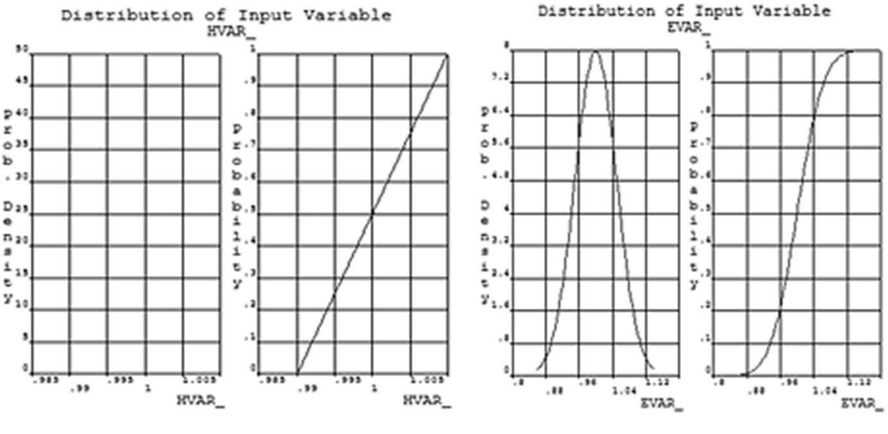

Fig. 10.4. Histogram of input variable *Hvar_* and *Evar_*

Table. 10.2. Specification of the random input variables

Name	Charact. value	Value	Variable Param.	Histogram	Mean or Min. value	St. Dev. or Max.value
Concrete slab						
Young´s modulus	EX [kPa]	3.1E+07	Evar_	GAUS	1	0.05
Poisson´s ratio	mi [-]	0.2	mivar_	GAUS	1	0.05
Thickness	H [m]	0.5	Hvar_	UNIF	-0.01	+0.01
Soil						
Elastic foundation stiffness	k [kN/m3]	4.6E+4	KKvar_	GAUS	1	0.05
Load						
Forces	F1 – F4 [kN]	914-3342	Fvar_	LOG1	1.0	0.1

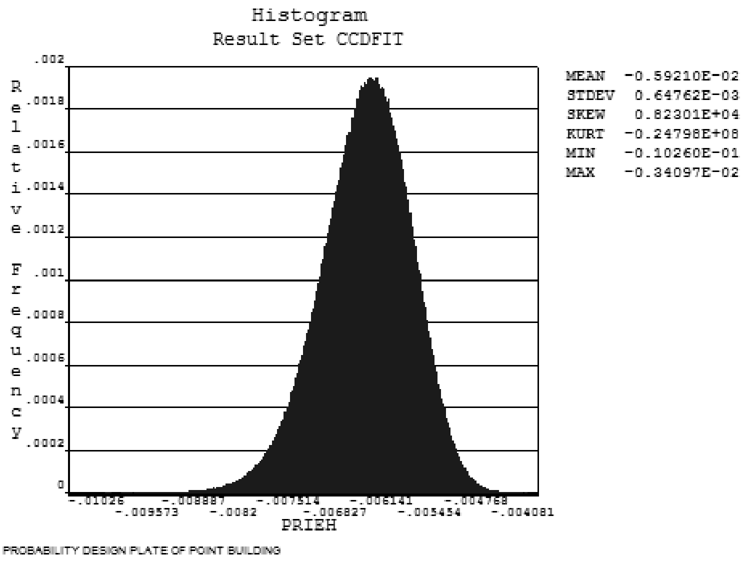

Fig. 10.5. Histogram of max. deflection PRIEH

Resulting from variability of input quantity 25 simulations on the base of RSM method were performed. The probability of exceeding the limit deflection of the foundation slab was calculated from five millions Monte Carlo simulations for 25 simulations of approximation method RSM on the structural FEM model, see Fig. 10.5.

According to the CDF - Cumulative Distribution Function) we can determine probability of the corresponding parameter PRIEH (the maximum value of deflection). The probability that max deflection is less than – 7.0 mm, representing that the design is at 5.6 e-2 unreliable.

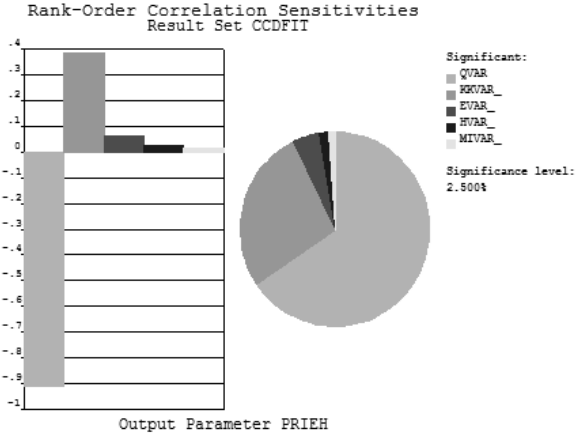

Fig. 10.6. Rank-order correlation sensitivities of output variable PRIEH

The evaluation of the probabilistic sensitivities is based on the correlation coefficients between all random input variables and a particular random output parameter. Either Spearman rank order correlation coefficients or Pearson linear correlation coefficients may be used based on user's specifications. To plot the sensitivities of a certain random output parameter, the random input variables are separated into two groups: those that are significant (important) and those that are insignificant (not important) for the random output parameter. The sensitivity plots will only include the significant random input variables, see Fig.10.6.

10.5. Conclusions

The main aim of this chapter was the deterministic and probabilistic analysis of the foundation slab under the residential building rested on layered subsoil. It was modeled in software Ansys. The layered subsoil was included in the calculation using the stiffness coefficient of the subgrade. From deterministic analysis max. deflection of the foundation slab rested on the layered subsoil was -5.9 mm. After deterministic analysis probability analysis was performed. The goal was to determine the probability of exceeding the deflection limit in the foundation gap by 6 variable input parameters. The probability of failure is equal to 5.6e-2 in the case of deflection limit -7.0 mm (determined by the investor), using 5 million Monte Carlo simulations for 25 cycles of the RSM approximation method on the FEM model.

References

Haldar A., Mahadevan S., *Probability, Reliability and Statistical Methods in Engineering Design*, John Viley&Sons. New York, 2000.

Jendželovský N., Baláž L., *Modeling of a gravel base under the cylindrical tank, Advanced Materials Research*, 2014, Volume 969, pp. 249-252.

Klucka R., Frydrysek R., Mahdal M., *Measuring the deflection of a circular slab on an elastic foundation and comparison with analytical and FE approaches, Applied mechanics and Materials*, 2014, pp.407-412.

Krejsa M., Kralik J., *Probabilistic Computational Methods in Structural Failure Analysis Multiscale Modelling,* 2015, 6: 1550006 OI:http://dx.doi.org/10.1142/S1756973715500067.

Kotrasova K., Kormanikova E., *A case study on seismic behavior of rectangular tanks considering fluid - Structure interaction*, International Journal of Mechanics, 2016, Volume 10.

Marek P., Brozzetti J., Gustar M., *Probabilistic Assessment of Structures Using Monte Carlo Simulation Background*, Exercises and Software, ITAM CAS, Prague, 2003.

Sumec J., Kuzma J., Hruštinec L., *Experimental tests of the deformation and consolidation properties of the cohesive soils and their use in the geotechnical calculations*, 48th International Scientific Conference on Experimental Stress Analysis, EAN 2010, 2010,Velke Losiny; pp. 415-420.

Zienkiewicz O. C., Taylor R. L., *The Finite Element Method.* 2000, vol. 2: Solid Mechanics. 5rd ed. Oxford: BUTTERWORTH-HEINEMANN.

WYDAWNICTWO POLITECHNIKI KOSZALIŃSKIEJ
www.wydawnictwo.tu.koszalin.pl

ISSN 0239-7129
ISBN 978-83-7365-474-7